University of Nottingham
UK | CHINA | MALAYSIA

High Pressure and Standard Photoelectron Spectroscopy of Materials for Hydrogen Storage and Production

Thesis submitted to the University of Nottingham for the degree of **Doctor of Philosophy, November 2023.**

Christopher P. C. Ryder

10189323

Supervised by

Dr James N. O'Shea

Abstract

It is widely agreed that hydrogen, a clean, renewable fuel which produces only water as a by-product when reacted with oxygen in air, can and must be used to replace fossil fuels for applications across all sectors if global targets for greenhouse gas emission reductions are to be met, and the harmful effects of the climate crisis are to be mitigated and reversed. However, many of the technologies associated with the lifecycle of truly green hydrogen are still in their infancy. Production still relies heavily on fossil fuels, and electrolysis alone cannot be expected to cover the entire capacity required for their replacement, while the storage of hydrogen commonly uses very high-pressure compression (up to 700 bar) with large associated costs and safety concerns. This thesis therefore looks to investigate materials which may provide alternative methods in each case, namely solar water splitting photocatalysed by titanium dioxide for production, and solid-state storage of hydrogen in intermetallic compounds.

These investigations are performed with core-level, X-ray-based spectroscopies, which can be used to effectively probe the surfaces of materials, providing detailed information about the constituent elements and the chemical state of the system. However, these analytical techniques generally require ultra-high vacuum conditions, while reactions of materials for solid-state hydrogen storage often occur at ambient pressures and above.

A solution to overcome this so called "pressure gap" is therefore required for their effective analysis.

It is for this reason that, in this thesis, a novel differentially pumped multi-stage transfer device was designed to enable the rapid transfer of a sample from reaction to analysis conditions, such that the measured results of analysis techniques including XPS could more accurately represent the actual behaviour of a sample under those reaction conditions. A 'proof of concept' study was performed to display the unique capabilities of the system, in which argon ion sputtering was used to create defective states in the surface and sub-surface layers of a titanium dioxide crystal. The defective crystal was then moved to the reaction chamber of the device, where it was exposed to the atmosphere in an attempt to heal the defects. It could then be transferred back into position for XPS analysis within just 5 minutes for observation of the healed titanium states.

The surface of a high entropy alloy, $(Ti_{0.65}Zr_{0.35})_{1.05}MnCr_{0.8}Fe_{0.2}$, with potential for applications in hydrogen storage, has been investigated with X-ray photoelectron spectroscopy and Near-edge X-ray absorption Fine Structure spectroscopy before and after exposure to conditions associated with hydrogen activation. A surface oxide layer seen on the as-received alloy was reduced when heated to 650^{o}C under vacuum for 30 minutes. After another sample of the alloy was heated to the same temperature in 1 bar of hydrogen, only chromium and iron appeared to reduce to metallic states, while manganese was seen on the surface in significant amounts in the form of Mn_3O_4 and MnO. It is suggested that this sacrificial oxidation of manganese may allow chromium and iron to remain in reduced metallic states to provide a pathway for the dissociation of the hydrogen molecules and diffusion of hydrogen atoms into the bulk for activation.

Finally, a combination of X-ray Photoelectron spectroscopy, Near-edge X-ray Absorption Fine Structure spectroscopy and Resonant Photoemission spectroscopy was used to investigate the interactions between titanium dioxide, in the form of nanoparticles, and a gold crystal surface. The two materials are commonly combined for use in solar water splitting for the production of green hydrogen, so an improved understanding of the interactions and charge transfer dynamics may aid in the further development of the technology. Through analysis of the measured spectra and the core-hole clock method, no evidence of charge transfer between the two materials was observed on the timescale of the core-hole lifetime. Argon ion sputtering of the deposited nanoparticles did however appear to show a reduction in their size, providing a potentially unexplored method of introducing quantum confinement effects into the semiconductor for possible improvements in efficiencies of titanium dioxide photocatalysed devices for solar water splitting.

Acknowledgements

4 years (and two months) is a long time to be working towards one goal, and a lot has happened both in the world and in my life in that time. It's important then to acknowledge those who have helped me along the way.

Jake and Will; sharing all of our individual struggles has made the process a lot easier, and I'm sure that our daily lunchtime walks have been beneficial to the quality of the work we've produced (and not just an excuse to get a coffee and a squaddie bar).

The experiments carried out at MAX-IV, essential to this thesis, could not have been done without the help and insight of Rob, Ellie and Mattia, while the same can be said of Jack for all of the experiments in Nottingham, who helped to show me the ropes and then some.

My supervisor, James O'Shea, was as good a supervisor as I could have asked for. With all of the help and advice, and always being just an email away, I certainly wouldn't have been able to produce this piece of work without him. Also for helping to keep me sane during the night shifts in Sweden, where all we seemed to be doing was sputtering and annealing for 12 hours straight!

Finally, I'd like to acknowledge my family. Mum and Dad, for everything you've done, not just over the past 4 years, but the 23 before that too. Jam, Sarah, Keegs, Caroline and especially the kids, for reminding me that there are things in life more important than work, and more exhausting!

Contents

Chapter 1

Introduction and Background Literature

Contents

1.1 XPS at Elevated Pressures

1.1.1 XPS and the "Pressure Gap"

XPS may be used to characterise atoms and identify elements in a sample, as well as providing information about the chemical state of a system [1–4]. The sample itself is irradiated with X-rays by a direct process; the X-ray is absorbed by an atomic electron which is in turn emitted from the sample. The kinetic energies E_K of the ejected electrons are measured, and the binding energies E_B can be calculated from the equation

$$E_B = h\nu - E_K - \phi \tag{1.1}$$

where $h\nu$ is the energy of the incident X-rays and ϕ is the work function of the spectrometer used. The binding energy of an electron is characteristic of the element, orbital and chemical environment of the atom from which it was emitted, while the recorded intensities enable quantification of elements [3]. The technique is described in great detail in Section 2.1.

Electrons have a strong interaction with atoms at typical electron energies used in XPS (100 eV – 1000 eV), giving them a mean free path on the order of only several monolayers [5]. In fact, the number of electrons emitted decreases exponentially with depth [6]. XPS therefore has exquisite surface sensitivity, with a sampling volume extending from the surface to a depth of around 50-70 Å [7]. The surface of a sample represents a discontinuity between one phase and another, thus it has different physical and chemical properties than the bulk of the material. Many problems associated with modern materials can be solved only by understanding these

surface properties and the interactions that occur there [3]. For example, this understanding has allowed for the investigation of the interfaces of Li-ion batteries [7] and for the emergence of solid-state hydrogen storage; further investigation could help to enable its optimisation and large-scale commercial use.

An issue with XPS as an analytical technique is that it requires UHV conditions (pressures below 10^{-9} mbar) in order for measurements to be taken. The main reason for this is to keep the sample clear of impurities, which will disrupt measurements. Another reason is that the photoelectrons emitted following irradiation of the sample are strongly scattered by gas molecules, and have a very short mean free path. Inelastic scattering is the primary contributor to the attenuation of the recorded signal I which, compared to the signal I_0 at pressure p_0 under vacuum conditions, has the relationship

$$I \propto \exp\left(-\sigma d p\right) \tag{1.2}$$

with d the distance that the electrons travel in a gas at pressure p, and σ the scattering cross section, which depends on the chemical composition of the gas phase. As an example, electrons with 100 eV of kinetic energy in 1 mbar of water vapour have a mean free path of around 1 mm. This is much shorter than the few centimetres of the typical working distance between a sample and the entrance to the electrostatic lens system of an electron analyser [2]. A solution, to what is known in surface science as the "pressure gap" [8], is therefore required for the use of XPS in experiments that require elevated pressures for reactions to proceed.

1.1.2 Ambient Pressure XPS

XPS at ambient pressure (APXPS), often called high pressure XPS to distinguish it from the vacuum-based technique, was initially introduced in the early 1970s [9]; the instrument used, and new ones produced over the next decade, employed a differential pumping scheme. In these schemes, shown in Figure 1.1, several pumped stages are connected only by small apertures, allowing for a downward pressure gradient to form from the sample chamber to the analysis chamber. This has allowed the sample compartment to be at pressures up to around 1.3 mbar [10, 11], while UHV conditions were maintained in the analyser, and enabled the investigation of the interfaces of vapours and liquids [9, 12], of vapours and solids [13], and of liquids and solids [14].

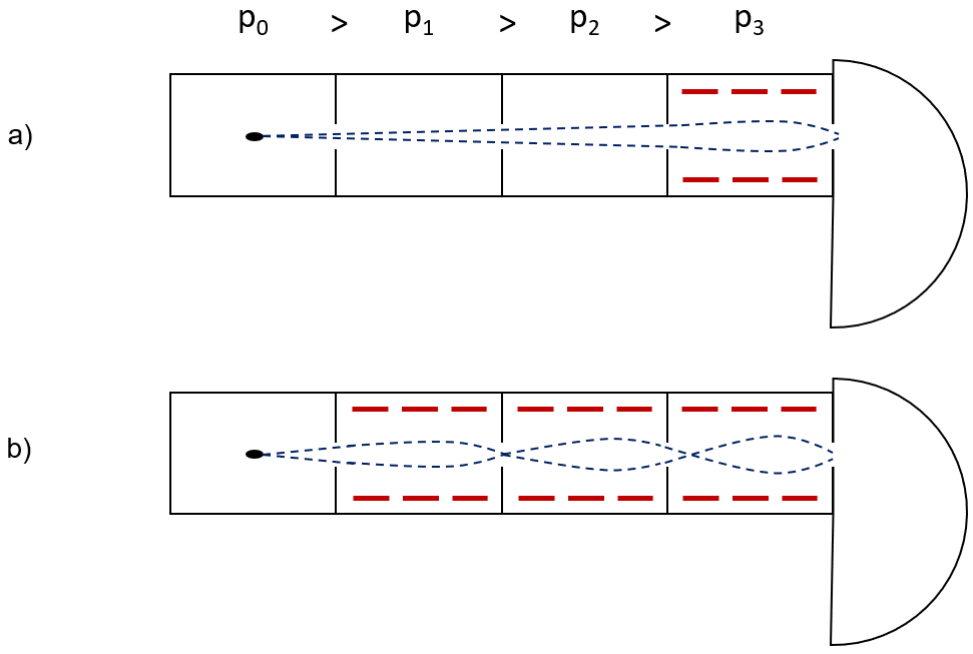

Figure 1.1: Differential pumping schemes (a) without and (b) with an electrostatic lens system for focussing the electrons into the entrance slit of the analyser. In both cases the pressure decreases from p_0 in the sample chamber to p_3 in the analyser.

It can be seen in equation 1.2 that, in the reaction chamber of a differential pumping scheme, the distance d between the sample and the entrance aper-

ture is the only property that can be adjusted, and in this case decreased, in order to reduce the attenuation of the electron signal; the scattering cross-section σ is characteristic of the experiment and the pressure p is sought to be as high as possible. This distance must, however, remain approximately equivalent to two entrance aperture diameters, to prevent the pressure drop across the aperture from affecting the reactions occurring at the sample surface [2]. A smaller sample aperture diameter thus allows for a smaller sample to aperture distance, and so reduced attenuation. Furthermore, the smaller entrance aperture reduces gas flow into the pumping system, allowing for larger secondary apertures between stages. This increases the electron collection efficiency of the analyser without sacrificing the achievable pressure differential across the stages [2]. The key factor in optimising the technique, however, is found to be the size of the photon spot targeting the sample; a smaller photon spot allows for a smaller aperture diameter, and so a smaller sample to aperture distance to reduce attenuation of the detected signal by electron scattering.

It is for this reason that the development of APXPS was greatly accelerated by the advent of third-generation synchrotron facilities in the early 2000s (the use of synchrotron-based X-rays has the key advantage of providing a smaller photon spot size [2, 15]) and by the improvement of laboratory-based APXPS instruments over the past two decades. In 2013, using a tightly focussed, high flux, synchrotron-based X-ray source, the diameter of the entrance aperture to the differential pumping stages of an APXPS system was able to be reduced from 1 mm to 50 μm. In addition to allowing for a smaller sample to aperture distance, so reducing the attenuation of the signal, this lowered the gas flow into the analyser by a factor of 400, thus increasing the pressure limit in terms of differential pumping by the same amount. Despite being relatively simplistic in that the pumping

stages lacked an integrated electrostatic lens system, spectra were obtained at sample pressures as high as 130 mbar [15]. The electrostatic lens system was first introduced in 2002 [16], as a method to optimise differential pumping without a loss of signal. The electrons are focussed onto to the aperture planes, thus preserving the acceptance angle whilst allowing for small apertures and increased differential pumping. The majority of instruments introduced after this have made use of some form of a differentially pumped electrostatic lens system [2]. The technique of differential pumping, as used during this project, is described in more detail in Section 3.2.1.

1.1.3 High Pressure Cells and Sample Transfer

In many cases, it is useful to understand how reactions occur at pressures higher than atmospheric. For example, there have been numerous studies into the behaviour of catalysts at higher pressures [17–21], which are discussed shortly. Meanwhile, as an example application, the target pressure range for on-board vehicular hydrogen storage is stated as 5-12 bar by the United States Department of Energy [22]. In order to use XPS to study the reactions occurring between hydrogen and other substances at these higher pressures, different techniques must be explored which allow a sample to be quickly transferred from a high pressure to a UHV environment, without removing the sample from the controlled atmosphere. A broad selection of devices and their important properties as described in the literature are shown in Table 1.1.

A commonly used method makes use of a high pressure cell, which allows the sample to be exposed to reacting gases before the cell is evacuated and opened, exposing the sample to the UHV environment for analysis. In some cases, the pressure inside the cell is only as high as atmospheric, providing

Table 1.1: Summary of key properties of devices described in literature for the analysis of samples after reactions at elevated pressures. High Pressure Cells and Sample Transfer are represented by HPC and ST respectively.

Name of Lead Author	Year	Device Description	Max Pressure (bar)	Volume of Reactor (ml)	Time to Analysis
Reijnen [23]	1990	HPC + ST	0.01	n/a	20 s
Kahn [21]	1974	HPC	1	571	n/a
Kuhrs [24]	2001	HPC + ST	1	4	n/a
Laegsgaard [25]	2001	HPC + ST	1	500	n/a
Du [26]	2018	HPC + ST	1	1000	n/a
Goodman [8]	1979	HPC + ST	2	n/a	5 mins
Moshfegh [18]	1988	HPC + ST	2.67	320	5-7 mins
Wang [20]	1992	HPC	5	45	1-2 mins
Ludviksson [19]	1995	HPC + ST	15	30	Several mins
Polaschegg [27]	1979	ST	30	20	1 min
Blakely [17]	1976	HPC	100	30	30 mins

an alternative means of carrying out APXPS [24, 28]. These systems may be cheaper and easier to implement into existing laboratories than a differentially pumped electrostatic lens system, but have the disadvantage of not providing in-situ measurements.

The first significant use of a high pressure cell in 1974 enabled the study of catalytic reactions on platinum single crystals at both UHV and atmospheric pressures [21]. The device makes use of a moveable cup which encloses the static sample in an analysis chamber. A seal is formed with a gold O-ring, which may endure only 20 repeated uses, while the volume of the cell is 571 cm^3. Similar devices that have followed have more commonly used cheaper copper gaskets or Teflon O-rings, and had reaction cells with far smaller volumes. It is important that the cells within which the reactions take place are as small as possible. A bigger sample surface-area-to-reaction-cell-volume ratio results in enhanced detectability of products, with less contamination by impurities, while also reducing the time taken for detection and pump-down [17]. Once sealed, the pressure inside the cell can then be increased to 1 atmosphere while UHV is maintained in the analysis chamber. The pressure can then be reduced, and the cup removed

to expose the sample to UHV conditions for analysis. This device was an important step in beginning to bridge the gap between traditional and new analytical tools for heterogeneous catalytic studies, allowing for UHV analysis of a sample following a reaction at an elevated pressure, without exposure to the external atmosphere.

A similar arrangement was presented a couple of years later [17], but allowed for the investigation of catalytic reactions on small surface area samples over a far wider pressure range. In this case, the sample is mounted such that it can be rotated 180^o at any pressure; it can be cleaned with an ion gun before being rotated for measurements to be taken by low-energy electron diffraction (LEED), Auger electron spectroscopy (AES), and thermal desorption. Although the apparatus was not used here for XPS measurements, it had the capability to do so given the correct attachments. This rotation at high pressures of up to 100 bar is enabled by a Teflon-sealed rotary element. Manipulators on conventional UHV systems are bellows-sealed, and only built to sustain 1 bar pressure. Once the sample has been cleaned and pre-reaction surface analyses have been performed, a small high pressure cell with an internal volume of 30 cm^3 encloses the static sample and engages a copper sealing gasket. Gases may then be pumped into the cell at pressures of up to 100 bar. This appears to be the highest pressure used with this type of device, and was done so in order to simulate conditions utilized in equivalent industrial processes such as Fischer-Tropsch synthesis, hydrocarbon reforming, and coal hydrogenation. Once the reaction has proceeded for the desired time, the cell is opened and evacuated. The sample can be in UHV conditions within around 30 minutes, and surface analyses may be performed. An important feature of this apparatus is the ability to remove and replace a sample without disturbing the UHV conditions. This saves a lot of time in experiments

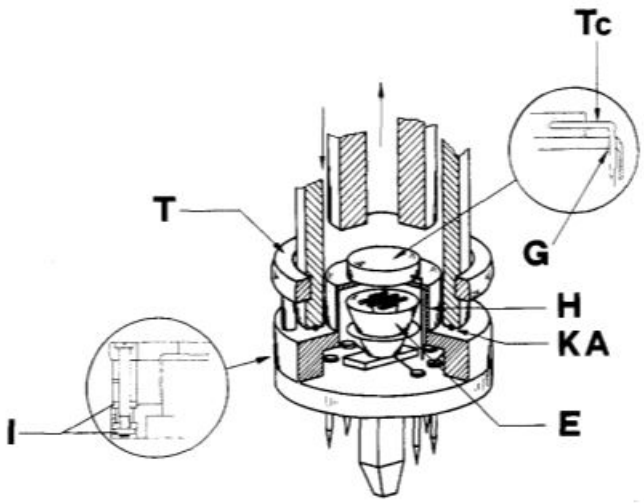

Figure 1.2: 'High-hat' sample mounting which enables sample heating by electron bombardment. The heating filament is kept in UHV conditions to reduce the risk of damage by corrosive gases. (H) high-hat like structure; (KA) Kalrez ring; (E) electron bombardment; (G) gold; (Tc) thermocouple; (T) ring used for sample transfer; (I) isolation [23]

with several samples, a problem which may also be overcome by mounting a selection of samples on a linear feedthrough into the UHV chamber [25]. As is the case with the majority of these types of devices, the desired sample temperature is achieved with resistive heating. Another option is heating by direct radiation, but this can increase the risk of side reactions and pressure changes occurring [17]. A different method of sample mounting has been used which allows heating by electron bombardment [23]; the 'high-hat' shaped structure, depicted in Figure 1.2, is able to withstand high pressure, has a low thermal conductivity to prevent damage to sealing O-rings, and most importantly allows for corrosive gases to be used without risk of damaging the heating filament, which is kept in UHV conditions.

With each of these devices, analysis of the gaseous products is done by either gas chromatography, mass spectrometry, or a combination of the two.

The paper written on the device described in [17] has been cited over a hundred times, with similar devices being used with slight adaptations to

suit their individual experiments. One significant example is a device which makes use of sample transfer, as well as a high pressure cell, to again investigate the effects of a small surface area catalyst on the hydrogenation of carbon monoxide [29]. This was a common theme for many similar papers in the period spanning from the late 1970s to the early 1980s, showing the economic importance of this industrial process at this time. In this case, once the reaction cell has been evacuated of gases, the sample is moved into the UHV chamber for analysis by AES. This transfer allows the sample to go from reaction pressures to UHV conditions within less than 5 minutes. This is a marked improvement on the previously described device, although the maximum reaction pressure in this case is only 2 bar. This set up and its achieved experimental results have been cited hundreds of times, with the same set up being used for further studies of single crystal catalysts [30].

A device described in 1992 uses similar methods to study catalytic reactions at pressures as high as 5 bar in the high pressure cell [20]. In this case, the reaction cell is designed such that it can mount directly onto an existing UHV system, thus eradicating the need for an extra rigid vacuum chamber. The cell itself is a cylindrical cavity in the end of a stainless-steel rod, but again is moved to seal over the static sample, with a cell volume of 45 cm^3. After reaction inside the cell at up to 5 bar of pressure, the cell can be evacuated such that the sample is ready for analysis in just 1-2 minutes. This is the shortest time achieved by a device with this type of arrangement, but did involve introducing a sudden heavy gas load to a turbomolecular pump, which could result in damage.

Another device makes use of a static high pressure cell, and a moveable sample [19]. The sample is mounted on a stainless steel electrical feedthrough tube with an outer-diameter of 0.75 inches. This is attached to the end of

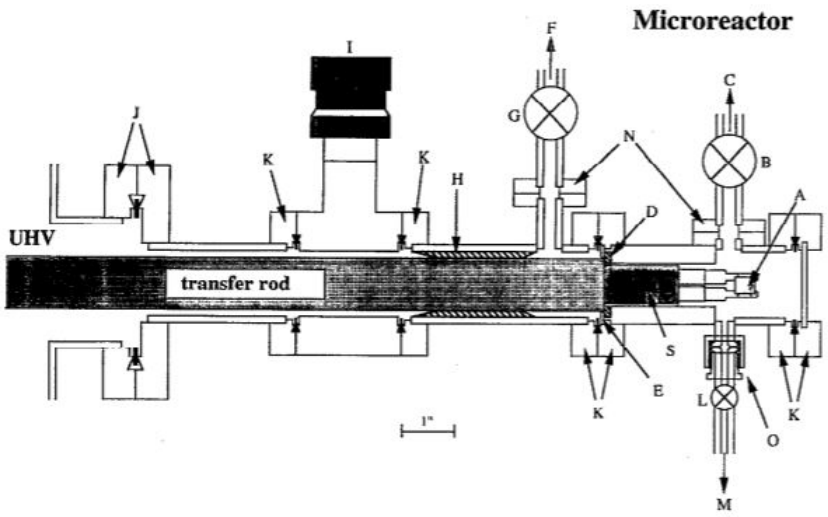

Figure 1.3: Diagram of device which makes use of sample transfer into a high pressure cell. The seal of the cell forms when the sample is fully inserted, with the sample mounted on a protruding electrical feedthrough. The distance between sample and seal helps to reduce the diffusion of impurities onto the sample. (A) sample; (B) valve to turbo pump, (C) turbo pump; (D) Teflon seat; (E) retainer ring for Teflon seat; (F) turbo pump; (G) valve to second turbo pump; (H) aluminized bronze insert which forces self-alignment of rod; (I) gate valve; (J) 4.5 inch conflat flange on UHV chamber; (K) 2.75 inch conflat flange; (L) valve to gas sources and chromatograph; (M) to gas handling system and gas chromatograph; (N) 1.33 inch conflat flange; (O) VCR fitting with a Cu gasket; (S) 0.75 inch-o.d. stainless steel Ceramaseal electrical feedthrough tube [19].

a 1.00 inch outer-diameter transfer rod, such that the sample can be driven from the analysis chamber into the static cell. This setup then allows for a seal between the end of the transfer rod and a Teflon seat to form the wall of the cell, with the electrical feedthrough protruding into the cell itself, and is shown in Figure 1.3.

This protruding feedthrough is a unique feature of this device, providing a large enough distance from the seal to the sample, over which impurities are unable to diffuse during prolonged use. The use of Teflon, as opposed to another metal, gives the advantage of being easier to maintain after repeated uses than it would be for an all-metal seal, as well as being cheaper and requiring smaller forces for sealing. When the cell was filled with 10 bar of hydrogen, UHV was maintained in the analysis chamber, and there

were no measurable amounts of impurities on the sample. This method still requires pumping into the cell after the initial seal is made, and evacuation of the cell before the seal is released, thus taking several minutes for the sample to be exposed to UHV after the reaction.

In 1979, a device was presented that utilises sample transfer, differential pumping, and a static high pressure chamber [27], as opposed to a retractable a high pressure cell, with the paper explicitly claiming to have improved upon the methods described in [17]. A ground sample rod, with a recess for the sample, is passed through a series of differentially pumped Teflon and Viton sealing ring systems. By connecting two sealing ring systems in series with a differential pumping stage in between, a pressure differential of 16 orders of magnitude can be obtained. After a reaction at up to 30 bar in the preparation chamber, the sample can be transferred into the UHV chamber for analysis by AES in less than 1 minute; the key advantage of this device over any of those previously described is that pump-down of the reaction chamber is not required before the sample is moved to the analysis chamber. When the sample is inside the reaction chamber, the apparatus benefits from the relatively small internal volume, equal to 20 cm^3. For high temperatures, the sample is again heated by resistance, and since it can be mounted horizontally, there are no special requirements for granulated samples. The paper claims several advantages over the work in [17], in addition to the obvious reduction in transfer time between pressure regions: the preparation chamber is able to be flushed before the sample is in place, this prevents undesirable reactions between the sample and the now saturated chamber wall; the lifetime of the sealing system is lengthened by the lack of complex mechanical manipulation; the preparation process can be interrupted at any time, and the sample transferred to the UHV chamber for mid-reaction analysis. The latter

advantage is utilised for the repetitive monitoring of catalyst surface composition, again for the hydrogenation of CO, with the same equipment set up [31]. Despite these advantages, the sample transfer device was only used in a handful more experiments [32]. A potential reason for its lack of use may have been due to the level of impurities able to reach the sample through this setup. In fact, Polaschegg, an author on this paper, had previously patented a similar device, but with a different layout [33] with the main purpose of preventing the transfer of impurities into the analysis chamber. In the patented device, the positions of the analysis and reaction chambers were switched. This means that the sample rod does not have to pass through the reaction chamber in order to reach the analysis chamber, where it might otherwise absorb a considerable amount of gas onto its surface. The rod itself then also has a detachable section, such that when the sample is withdrawn from the reaction chamber into the analysis chamber, the part of the rod exposed to reactant gases may be left behind in the sealing system located between the two chambers. These differences are demonstrated in the schematics shown in Figure 1.4.

Despite its apparent advantages, this arrangement may be more difficult to install on an existing apparatus, and this may be the reason that it was not used by Polaschegg in the future device.

It would seem that the majority of devices for UHV analysis of elevated pressure reactions make use of a high pressure cell, where a seal forms around a sample before the cell is filled with reactant gases. After the reaction has occurred, the gases are pumped away and the pressure lowered, such that the seal can be broken and the sample exposed to the UHV conditions of the analysis chamber. The time between the reaction finishing and the analysis taking place is therefore limited by the pumping speed available. These high pressure cells, however, tend to be relatively easy

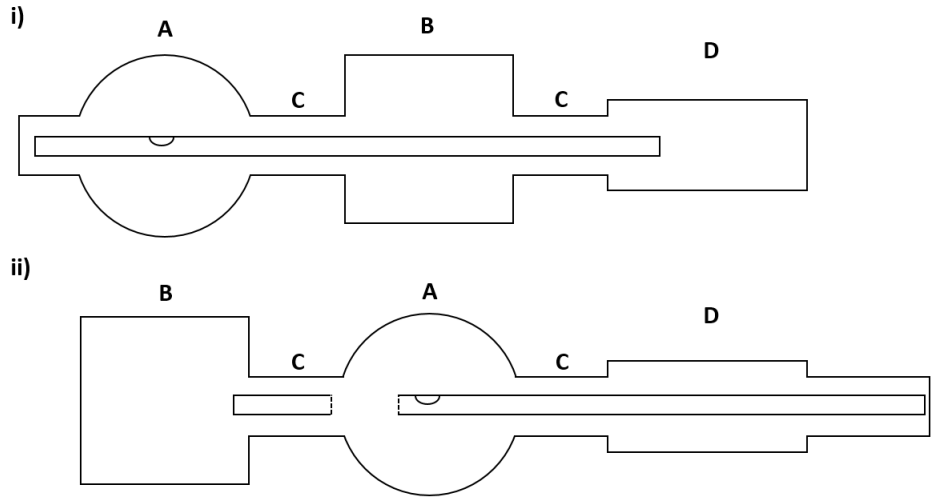

Figure 1.4: Simplified schematics showing the rod and chamber arrangements for the analysis of a previously prepared sample. i) The analysis chamber is furthest from the atmosphere [27], ii) The positions of the analysis and reaction chambers have been switched, and a detachable rod section incorporated, in an attempt to reduce the diffusion of impurities onto the sample [33]: (A) analysis chamber; (B) reaction chamber; (C) differential pumping stage; (D) external drive at atmospheric pressure; (E) sample recess; (F) detached section of sample rod.

to attach to existing laboratory apparatus, potentially saving on cost and time for implementation when compared to larger devices with multiple chambers.

One of these larger devices is the differentially pumped sample transfer mechanism that was previously described [27]. It boasts the significant advantage over the other devices that it overcomes the limit of pumping speed, by not requiring pumping down at all. It could be argued that this device has not been thoroughly proven experimentally, with only a few uses outside of the original presentation. However, with an appropriate method for overcoming the associated high impurity levels on the sample, such as an increased diffusion distance [19] or a rearrangement of the setup [33], this device has the most potential for the rapid analysis of a sample after a reaction at an elevated pressure, in particular at intermediate pressures up to around 30 bar. If even higher pressures are required, a device similar

to that with the moveable cup and static sample [17] might prove more appropriate, although the higher pressures would be achieved by sacrificing the short time for analysis.

One problem not addressed by the differentially pumped sample transfer device [27] is the lack of capability to analyse an air-sensitive sample. For example, a metallic sample will form an oxide layer on the surface when exposed to air, which may affect the reaction of interest in the reaction chamber. This is also the case with many metal and intermetallic hydrides, a problem that is addressed in this thesis. The reason for this is that sample mounting takes place in the open atmosphere. There is therefore no means of transferring the sample from an inert glove box, for example, into the reaction chamber without air exposure. For the other devices described, a 'vacuum suitcase', making use of mechanically operated air-lock systems [34, 35] or even a more complex disposable membrane [36], can be used such that the sample is transferred into the reaction chamber under vacuum.

1.2 Solid-state Hydrogen Storage

Global demand for energy is ever rising and, conversely, fossil fuel reserves are depleting. These non-renewable sources of energy also contribute to vast amounts of greenhouse gas emissions, which have extremely harmful long-term effects on human health and the environment. To mitigate and reverse these effects, fossil fuels must be widely replaced by a greener and more sustainable fuel in the near-future. Hydrogen is a clean, renewable fuel which produces only water as a by-product when reacted with oxygen in air. One of the key issues that must be addressed, however, to enable the mass-adoption of hydrogen in many of the key sectors, is associated

with its storage. Despite having an energy density (J/kg) more than twice as large as common fossil fuel, gasoline, hydrogen also has a significantly lower volumetric density (kg/m^3) at normal temperature and pressure, such that it requires around 4 times more volume than gasoline to store the same amount of energy [37]. For longer-term storage applications, such as stationary hydrogen storage used to balance seasonal supply and demand fluctuations, there is little restriction on space, and so high volumetric capacities are not a necessity. However, for on-board applications, especially in light vehicles, space is limited such that high gravimetric and volumetric capacities are required; the system targets stated by the United States Department of Energy (USDOE) are 0.065 kg H_2/kg system and 0.050 kg H_2/L system respectively [22], as shown in Table 1.2. In existing commercial vehicles, gaseous hydrogen is stored on-board at either 350 or even 700 bar, incurring significant costs associated with the need for tanks to safely withstand these excessively high pressures [38]. Another option is the use of cryogenic compression, through which capacity targets may be met with lower pressures, but the extremely low temperatures required ($\sim$20 K) again make it impractical and expensive. Solid-state storage, dealing with lower pressures and more convenient temperatures in line with the USDOE targets, appears to show the greatest potential as a permanent solution with a reduced safety risk and lower associated costs [39].

There has been much research into how the targets for on-board uses can be met through solid-state storage, with a wide array of materials investigated. However, simultaneously obtaining all of the desired properties, such as high gravimetric capacities, fast reaction kinetics, full reversibility and good cycling stability, all at near-ambient pressures and temperatures, is proving a tremendously difficult task [38, 39].

Storage Parameter	Unit	Ultimate Goal
System Gravimetric Capacity	kg H_2/ kg system	0.065
System Volumetric Capacity	kg H_2/ L system	0.050
Operating Temperature	^{o}C	40/60
Min/Max Delivery Pressure	bar	5/12
Cycle Life	cycles	1500

Table 1.2: Summary of some of the key targets for on-board hydrogen storage systems set by the US Department of Energy [22]

Two main types of storage materials exist, those that store hydrogen via *adsorption* and those via *absorption*. Nanostructured materials like carbon nanotubes and metal organic frameworks can store hydrogen through adsorption of molecular hydrogen [40], offering potential safety benefits related to the lower pressures of the systems, but suffering from very low densities which can result in inefficient hydrogen storage [39]. Metal hydrides are instead chemical storage systems, which absorb atomic hydrogen into the interstitial sites within the material [41, 42]. The focus of this thesis is on metal hydrides and their derivatives, such that the adsorbing materials are not described in further detail.

1.2.1 Metal Hydrides

Conventional metal hydrides consist of a singular metal which reacts with hydrogen, absorbing it into interstitial sites between the metal atoms in the bulk. The reversible reaction of hydrogen with a generic metal M is described by

$$2M + xH_2 \rightleftharpoons 2MH_x \tag{1.3}$$

where the forward reaction (hydrogenation) is exothermic and the reverse (dehydrogenation) endothermic. The process, in both directions, consists

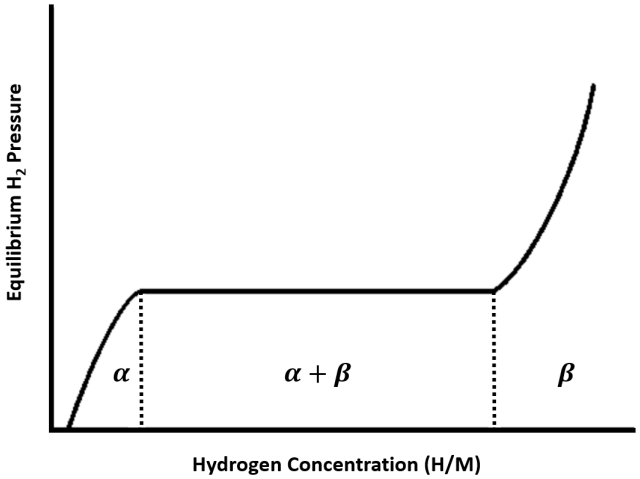

Figure 1.5: Generic pressure-composition isotherm (PCI) for hydrogenation of a metal and dehydrogenation of a metal hydride, showing the 2 phases present as the hydrogen concentration varies. This figure is adapted from [42]

of 2 phases: the α phase is a solid solution of the metal and hydrogen, the β phase is the metal hydride, while an intermediate mixture of the two phases $\alpha + \beta$ is also present during the process [41]. The relationship between the hydrogen concentration, or hydrogen to metal ratio (H/M), and the equilibrium hydrogen pressure is illustrated in the pressure-composition isotherm (PCI) in Figure 1.5, where a clear plateau is seen as the hydrogen concentration of the $\alpha + \beta$ mixture varies. The pressure of this plateau is temperature dependent and equivalent to the equilibrium dissociation pressure of the hydride, providing a measure of its stability [42]. In practice, the dehydrogenation isotherms are at lower equilibrium pressures than the hydrogenation isotherms; this hysteresis effect occurs due to localised defects and surface inhomogeneities [43] which affect the kinetics of the reaction.

The effect of temperature on the individual isotherms is shown in Figure 1.6a; the isotherms lie at higher hydrogen pressures when the temperature is increased. Figure 1.6b shows the associated generic van 't Hoff plot, from which thermodynamic properties can be calculated from the straight line

plot with equation

$$\ln p_{H_2} = -\frac{\Delta H}{RT} + \frac{\Delta S}{R} \tag{1.4}$$

where ΔH is the enthalpy of hydriding (or dehydriding), ΔS is the entropy change and R is the molar gas constant [41]. Values for ΔH and ΔS can therefore be calculated from the slope of the line and the y-intercept respectively.

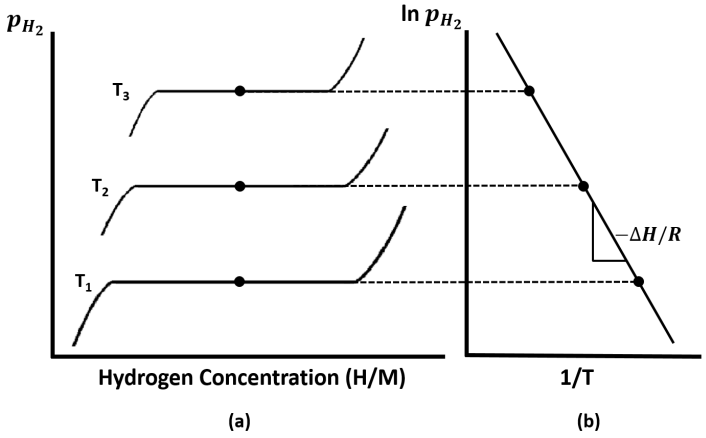

Figure 1.6: (a) PCIs at different temperatures where $T_1 < T_2 < T_3$ (b) van 't Hoff plot showing how hydrogen pressure and temperature are related by the enthalpy and entropy changes of the reaction. Both figures were adapted from [42]

Despite showing promise, singular metal hydrides have failed to provide a means of meeting the USDOE targets, often with some of the targets met, and others not. A prime example is magnesium hydride (MgH_2). Magnesium, a relatively cheap and abundant metal, forms a hydride with a hydrogen storage capacity of 7.6 percent of the total weight of the hydride (wt.%) [44]. This exceeds the USDOE target for on-board storage. However, the dehydrogenation reaction requires an impractically high temperature of ∼560 K at ambient pressure [45]. This is due to the extreme thermodynamics of the reaction, owing to the strength of the bond between magnesium and hydrogen [44]. The slow dissociation rate of hydrogen molecules on the magnesium surface also results in slow kinetics of the hydrogenation reaction [46]. These issues have been addressed for all metal

hydrides using several methods, including varying the hydride particle size, use of different preparation techniques such as ball milling, addition of catalysts, and many cases of mixing with other metals and elements to form new compounds [39].

1.2.2 Complex Hydrides

Complex hydrides combine lightweight metals such as lithium (Li), sodium (Na), potassium (K) and calcium (Ca) with other elements such as aluminium (Al), boron (B) and nitrogen (N) to form alanates, borohydrides and nitrates respectively. Showing promise with their ability to store relatively large amounts of hydrogen, for example lithium borohydride at 19.6 wt.% [47], and release it at mild conditions [48], complex hydrides suffer from issues with safety, decomposition into stable elements, high thermodynamic stability and slow kinetics [49, 50].

1.2.3 Chemical Hydrides

Chemical hydrides contain no metals, typically consisting instead of lighter elements [51], but have similar properties to complex hydrides in that they store large amounts of hydrogen and release it relatively easily. An example worth noting is ammonia borane (NH_3BH_3), which stores hydrogen at 19.6 wt.%. The hydrogen can be released via hydrolysis or thermolysis, but the process produces the undesirable product of ammonia, which must be separated from the hydrogen on-board in order to prevent poisoning of the fuel cell [52]. Chemical hydrides release hydrogen irreversibly, and so they are often used as one-way single use fuels [39], but since some exist in the liquid phase, they may possibly be able to make use of the existing

infrastructures currently used for gasoline [53].

1.2.4 Intermetallic Hydrides

Intermetallic hydrides combine the properties of the constituent metals such that more desirable hydrogen storage characteristics are achievable. One very early example of this was discovered over 60 years ago [54]; it was seen that the intermetallic compound zirconium nickel (ZrNi) reacted reversibly with gaseous hydrogen to form the ternary hydride $ZrNiH_3$. The alloy-based hydride combined the properties of the two constituent metal hydrides, with its enthalpy of formation lying between those of the stable ZrH_2 and the unstable NiH. This is caused by the strong destabilizing effect exerted by the Zr-Ni bond on the Zr-H bond, and leads to a reduction in the temperature at which a plateau pressure of 1 bar is achieved to a third of that for ZrH_2 [42]. Commonly, the hydride will consist of a metal with a high affinity for hydride formation and one with a lower affinity, denoted A and B respectively, where the A metals have negative hydrogen binding energies and the B metals positive [55]. The metals are combined to give several compositions of alloys, including AB_5, AB_2, AB, A_2B and AB_3.

The most thoroughly researched AB_5 alloy for hydrogen storage is lanthanum nickel ($LaNi_5$). While the excessively high temperature of 1300 ^oC is required to reach a desorption pressure of 2 bar for the standard metal hydride LaH_2, the intermetallic hydride $LaNi_5H_6$ reaches the same plateau pressure at just 20 ^oC, therefore showing great promise for practical applications [42]. The kinetics of the reaction are so fast it has even been used to catalyse the reaction of hydrogen with other materials [56]. It has, however, failed to be used practically for hydrogen storage due to the low storage capacity of just 1.4 wt.% and the high cost associated with the

lanthanum itself (a rare earth metal) [57].

AB_2 alloys, such as the widely studied $TiMn_2$, are Laves phase alloys. The three structures of Laves phases include cubic $MgCu_2$ (C15), hexagonal $MgZn_2$ (C14) and hexagonal $MgNi_2$ (C36), where in each case the A atoms take up hexagonal positions and B atoms surround them in a tetrahedral geometry [58]. While the unit block remains the same in each case (A_2B_4), the stacking sequence varies; C15 alloys exhibit an a-b-c-a-b-c sequence, while C14 and C36 alloys have a-b-a-b and a-b-a-c sequences respectively [59]. Hydrogen is then stored within the interstitial sites at capacities greater than that of $LaNi_5$, generally in the range of 1.8-2.0 wt.%, and at a lower cost [60]. The reversible hydrogenation occurs with fast kinetics at mild hydrogen plateau pressures, and after a simple activation process [60, 61]. Activation is the first time a material is hydrogenated, usually requiring a higher temperature and hydrogen pressure than the proceeding hydrogenation events. The methods of activation and further details are discussed later in this Section. The lack of wide commercial use of AB_2 Laves phase alloys such as $TiMn_2$ is a result of difficulties associated with the sloping plateau and large hysteresis of the PCI [61], as well as the significant negative effect of contaminants on the hydrogen storage properties [62].

AB alloys, TiFe the key example, store hydrogen reversibly in amounts comparable to those of AB_2 alloys [39]. TiFe has many desirable properties for hydrogen storage, but suffers from the fact that it requires extreme conditions for hydrogen activation. The reason for this is that the alloys have a low tolerance to oxygen poisoning and readily form a thin surface oxide film on the surface, which acts as a barrier to hydrogen absorption [63, 64]. This difficult activation process is particularly significant for TiFe, since, once activated, it proceeds to react with hydrogen at near-ambient

conditions [65]. For this reason, there has been much research into improving the conditions required for activation. Common attempts to overcome the activation issue use optimisation of preparation techniques, such as the use of ball milling [66, 67], and partial substitution of either Ti, Fe, or both [68–72].

1.2.5 High Entropy Alloys

A high entropy alloy consists of five or more metals at near-equimolar ratio; they are defined such that each element makes up between 5 and 35 at.-% of the total alloy [73]. Favoured by the high entropy of mixing, HEAs form solid solutions consisting of the metal lattice with electrons flowing within. The structures formed are simple structures such as body-centred cubic (bcc) or cubic close-packed (ccp), where the constituent metals are distributed randomly. This random distribution means that HEAs are heavily disordered [74] such that they, by the 'entropy-based' definition, have configurational entropy of at least $1.5R$, where R is the gas constant [75]. Since the lattice comprises several different metals, each with a different atomic radius, there is significant lattice strain. It is known that increased lattice strain allows for hydrogen to be stored within HEAs in relatively large amounts [76], improving upon capacities of the binary hydrides of any of the constituent elements [77]. Tunability is another exceptional feature of HEAs; desirable properties may be achieved by selecting the metals present in the alloy and their relative amounts [78]. For example, the electronic structure, hydrogen binding energy and resulting hydrogen storage temperature and pressure required for hydrogenation and dehydrogenation may be targeted with careful selection of the constituent metals and their concentrations [75, 79]. Transition metals are often those selected in attempts

to keep the hydrides lightweight and cheap when compared to rare-earth metals [77, 79].

HEAs therefore show much promise for use in practical applications of hydrogen storage [77], and as such there is significant research being done in the search for the ideal combination of metals. One study suggested three empirical criteria that should be adhered to when designing an HEA in order to achieve desirable hydrogen storage properties [80]:

1. AB_2-type atomic configuration – These are thought to have the most potential for low temperature storage when compared to other candidates such as AB and A_3B_2 systems

2. C14 Laves phase structure of the alloy and hydride – Explained previously as having the ability to store hydrogen reversibly with fast kinetics at mild hydrogen plateau pressures, and after a simple activation process [60, 61].

3. A valence electron concentration (VEC) of 6.4 - The VEC is defined as the number of valence electrons per formula unit [81] and can be calculated for an alloy with several metals by taking an average of the VECs of the constituent metals based on their atomic fractions present [74]. The VEC can have an influence on the properties of the alloy; for example, the onset temperature for hydrogen desorption from a metal or alloy decreases linearly with increasing VEC [74]. It is for this reason that metals such as titanium and zirconium, with low VECs of 4 [82], usually form stable hydrides which can only release hydrogen at high temperatures, while metals with high VECs of 9 and 10, such as cobalt and nickel respectively [82], have low affinities for hydrogen. VEC is also a property which is far easier to tune in HEAs than it is in binary or ternary alloys [55].

It is important that these criteria are properly validated before future studies can follow the findings unquestionably, to prevent future potential 'blind spots' where new materials are not investigated because they do not fit the criteria perfectly. For instance, achieving an exact VEC of 6.4 significantly reduces the number of metal combinations which may be used to form the alloy. There are examples of materials designed to fit the criteria which do show promise. One such material is described in the same study which suggests these criteria; the HEA TiZrCrMnFeNi stored 1.7 wt.% of hydrogen reversibly at room temperature with fast kinetics and without the need for activation, thus showing very promising signs for future practical applications, although the relatively low gravimetric capacity remains an issue. Similarly, another study investigated $Ti_xZr_{2-x}CrMnFeNi$ with $x = 0.4$, 0.8, 1.2 and 1.6 [55]. The VEC remains as 6.4 for each composition since Ti and Zr have the same VEC value. The plateau pressure was found to increase with decreasing amounts of Ti, with the alloys with $x = 0.4$ and 0.8 the only ones to hydrogenate and dehydrogenate near ambient pressure at room temperature. They also expectedly stored similar amounts of hydrogen to TiZrCrMnFeNi, which essentially just had $x = 1$. In an example of an HEA that does not fit the criteria, TiVZrHfNb, with a VEC of 4.4, was investigated for its hydrogen storage properties [77]. The alloy absorbed hydrogen at room temperature with a plateau pressure of 0.1 bar at a capacity similar to $Ti_xZr_{2-x}CrMnFeNi$ with $x = 0.4$, 0.8 and 1. Therefore, although the criteria can result in the design of materials with promising storage properties, it appears not to be essential for all three criteria to be met, and so may be problematic to suggest otherwise.

1.2.6 Activation

As previously mentioned, activation can be a practical barrier for alloys as hydrogen storage materials. The need for activation predominantly stems from the fact that most alloys will react in air and form an oxide layer on the surface, which must be removed before hydrogen is able to be absorbed into the material [83–86]. For hydrogen to be absorbed into a metal or alloy, it must first dissociate from molecular to atomic hydrogen. This occurs via a reaction catalysed by metal atoms on the surface, after which the atomic hydrogen is able to diffuse into the bulk where the hydride is formed [87, 88]. For AB_5 alloys such as $LaNi_5$, activation is easy, since the oxide layer does not prohibit the reaction with hydrogen; the nickel atoms are available to catalyse the dissociation reaction at the surface [89]. However, in most cases the oxide layer acts as a barrier between the hydrogen molecules and the metal atoms [83, 90]. The oxide layer itself forms when the material is exposed to air and may also be introduced during preparation. The time of exposure also increases the difficulty of activation, as the oxide layer becomes thicker [87]. It must therefore be removed or altered, usually by a high temperature; the layer becomes thinner and disintegrates when enough energy is provided to break the metal-oxygen bonds, and the oxygen diffuses away. Where the oxygen goes is subject to discussion, with some believing that instead of leaving the metal as a gas, oxygen atoms diffuse into the bulk of the metal [88]. This is particularly interesting in the context of hydrogen storage, since bulk sites for occupation by hydrogen may instead be occupied by this oxygen, such that the hydrogen storage capacity of the material is reduced.

Temperatures and pressures required for the initial hydrogenation are far higher than the operating conditions that follow [84], meaning that the

activation step alone places extreme constraints on practicalities such as vessel construction and safety management. For this reason, there have been significant efforts to reduce the need for the extreme conditions to activate intermetallic hydrides. One method involves the substitution of one or more of the constituent elements. For example, for TiFe, a promising hydrogen storage alloy with a difficult activation process, both Ti and Fe have been partially substituted with other metals, successfully removing the need for extreme conditions to enable the first hydrogenation [64, 91, 92]. Other attempts concern the methods used to prepare the alloys themselves. Many mechanical preparation methods have been used successfully [93–95], but perhaps the most promising preparation technique to enable activation at ambient conditions is ball milling [96]. Ball milling is where a sample is transferred to a container containing heavy balls that assist in size reduction by continuous grinding [97]. This decrease in size of the alloy particles can improve hydrogenation kinetics by providing more metallic surface sites for hydrogen dissociation [98–100]. Dry ball milling of alloys can however cause agglomeration and the formation of clusters, counteracting the reduction in particle size. The addition of ethanol during the process has been seen to reduce this effect; the ethanol helps to spread the sample and increase the active surface due to its large polarity, as well as removing the oxide layer due to its reduction ability, making the dissociation of hydrogen on the surface easier [96].

The mechanism of activation of intermetallic hydrides is not yet fully understood, but can be investigated with analysis techniques such as XPS in attempts to propose potential routes [96, 101]; quantifying the amounts of each element in the surface layer as well as the oxidation states of the metals before and after the activation process can help to suggest what happens on the surface during activation that enables the first uptake of

hydrogen. One such study is described in Chapter 5 of this Thesis.

1.3 Titanium Dioxide for Solar Hydrogen Production

For hydrogen to be used as a truly green technology, all aspects of its lifecycle, from production to use, must result in net-zero greenhouse gas emissions. Currently, only a tiny proportion of global hydrogen production is green; according to a report from the International Renewable Energy Agency [102], at the end of 2021 just 4 % was produced with electrolysis, with the rest produced using fossil fuels such as natural gas (46%), coal (27%) and oil (22%). Further, since only around 33% of global electricity was produced using renewable energy, it can be said that only $\sim$ 1% of global hydrogen production at this time could be considered green, a figure which remained true for 2022 [103]. The scale up of electrolysis using electricity from renewable sources is therefore a key priority if targets for global hydrogen use are to be met; it is estimated that in order to be on track for the Net Zero Emissions by 2050 (NZE) Scenario, by 2030 an installed capacity of more than 550 GW of electrolysers is required [104]. This is a significant increase on the total installed capacity recorded in 2022 of around 690 MW. This rapid increase in capacity would also require extremely large amounts of renewably generated electricity and enhancement of the power grid. Additional options for net zero production include 'blue' hydrogen, where carbon capture and storage (CCUS) is used to remove emissions after hydrogen production with fossil fuels, and other green technologies including solar water splitting, where hydrogen is generated from the splitting of water using only solar energy. Like electrolysis, water

is the only feedstock, making solar water splitting a sustainable and environmentally friendly technology [105]. Devices used for this process have commonly consisted primarily of silicon, but the high cost associated with their complex production process has placed limits on commercial applications [106]. It is for this reason that lower cost alternatives are being widely researched. One such material is titanium dioxide (TiO_2).

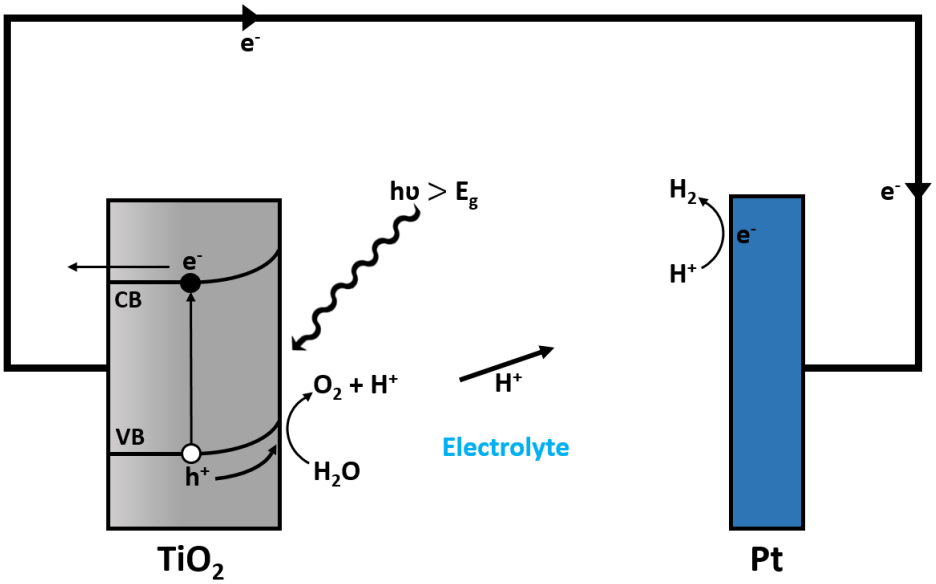

Figure 1.7: First system, developed by Fujishima and Honda [107], to achieve solar water splitting on a TiO_2 photoanode.

With abundant reserves and reactivity with light and water without corrosion [105, 108], the use of TiO_2 as a photocatalyst for solar water splitting has been widely reported. The first evidence was shown by Fujishima and Honda in 1972 [107]. The experimental setup is represented in a simple diagram in Figure 1.7; a TiO_2 photoanode was connected to a platinum cathode via an external circuit, with an aqueous electrolyte completing the cell. When UV radiation is incident upon the semiconductor photoanode, electrons from the valence band are excited across the band gap of energy E_g to the conduction band [109], leaving positive holes in the valence band; the electron-hole pairs generated form the basis of photocatalysis. The holes act to drive the oxygen evolution reaction (OER) by oxidising H_2O

molecules at the photoanode:

$$H_2O + h\nu \longrightarrow \frac{1}{2}O_2 + 2H^+ + 2e^-$$

where the incident photon energy $h\nu$ must be greater than the band gap energy of TiO_2 (3.2 eV [110]). Electrons flow from the conduction band into the external circuit, while H^+ ions produced by the OER reach the cathode via the aqueous electrolyte, and the two combine at the cathode to produce hydrogen through the hydrogen evolution reaction (HER):

$$2H^+ + 2e^- \longrightarrow H_2$$

Adaptations to the system have been made in attempts to improve the energy conversion efficiency (ECE), with TiO_2 used in many forms such as nanoparticles or thin films to maximise its surface area available for light absorption [111]. However, the most important factors for improving the ECE for photocatalysed solar water splitting involve the wavelength of light that can be absorbed, and the separation and transport speed of photoinduced charges [112].

Due to the relatively large band gap of TiO_2, visible light is not able to excite electrons from the valence to the conduction band of the semiconductor. This greatly reduces the efficiency upon absorption of solar radiation since visible light makes up $\sim 46\%$ of it, while UV accounts for just $\sim 4\%$ [109]. A solution to this problem is to 'sensitise' the TiO_2 with a material that is able to absorb visible light. The most common example of this is seen in dye-sensitised solar cells (DSSCs) [113–115]. With a system based on the first example of this device, known as a Grätzel cell [116], a dye on

the surface of TiO_2 absorbs visible light and injects the photoexcited electrons into the TiO_2 conduction band. Further examples use gold, instead of a dye, in a similar capacity [110, 117, 118]. Initially this might seem counterintuitive, since an interfacial Schottky barrier forms when gold and TiO_2 are in contact; the different work functions of the two materials induce a space-charge region with internal electric field, bending the bands of the semiconductor and introducing a potential energy barrier which must be overcome for electrons to pass from the lowest occupied molecular orbitals (LUMOs) of gold into the TiO_2 conduction band [119]. However, the barrier may be overcome if localized surface plasmon resonance (LSPR) bands form within the gold [120]. These occur when the frequency of incident photons matches the natural frequency of the surface free electrons, exciting energetically 'hot' electrons over the energy barrier [121]. These hot electrons have also been seen to display longer excited-state lifetimes than those photogenerated directly within TiO_2 via UV absorption [122], again improving the ECE of the system. Although more expensive, gold potentially provides a more robust alternative to the commonly used ruthenium-based dyes, which have often been known to evaporate or leak over the desirable lifetime a solar cell [123].

Photoinduced charge separation in TiO_2 enhances ECEs by preventing recombination of the electron-hole pairs, which otherwise produces unwanted heat and photons [110, 124]. Reduced recombination also leaves more charge carriers available to perform their respective roles in the oxygen and hydrogen evolution reactions. Gold has also been used to address this issue [125–127], acting as a 'cocatalyst' by trapping photoexcited electrons from the TiO_2 conduction band and passing them into the external circuit. The formation of an interfacial Schottky barrier is now beneficial, preventing the flow of electrons back into the TiO_2 photoanode for recombination

with holes [109, 112, 128]. Other noble metal cocatalysts have been used, such as platinum [129, 130], and although a higher rate of hydrogen evolution was achieved than with gold, gold is much less active in hydrogen oxidation, a back reaction that must be avoided to maintain higher ECEs for solar water splitting [131].

1.4 Aims and Structure of Thesis

The overall aim of the thesis is to use X-ray spectroscopies to investigate materials for their potential applications in hydrogen storage and production technologies. In the next Chapter, the underlying theory and utilisation of the experimental methods conducted throughout the thesis are described and explained in detail. Chapter 3, the first experimental chapter, describes the design and build of a novel device which aims to improve the capability of UHV-based techniques for use in rapid analysis of materials after reactions at ambient pressures and above, built with solid-state hydrogen storage materials in mind. The following chapter, Chapter 4, then describes a surface study of a titanium dioxide crystal; performed directly as a 'proof of concept' for the device, the study aims to display its unique capabilities. In Chapter 5, a high entropy alloy is hydrogenated for the first time in an 'activation' process. The process is highly dependent on surface interactions, such that XPS and NEXAFS may be used effectively to observe changes to the alloy which occur as a result. The final study in this thesis, described in Chapter 6, investigates the interactions between titanium dioxide and gold, two materials commonly combined for applications in green hydrogen production through solar water splitting. It aims to further develop the understanding of these interactions, with the two materials combined in a unique configuration.

Chapter 2

Methodology

Contents

2.1 X-Ray Photoelectron Spectroscopy

2.1.1 Introduction

XPS is a surface sensitive analytical technique which has been used for decades for the characterisation of elements and their environments within a sample [1–4]. First developed by Kai Siegbahn and colleagues in the 1940s and 50s [132], the technique, also known as Electron Spectroscopy for Chemical Analysis (ESCA), makes use of the photoelectric effect; a one-to-one interaction between a core electron and an incident photon results in said electron absorbing the energy of the photon, such that it can be fully ejected from the sample it resides in. The photons used for these ejections are in the form of X-rays, which are emitted from a source and aimed directly at the surface of the sample. The ejected photoelectrons are then detected, and their kinetic energies E_K measured. The binding energies E_B may then be calculated from the equation

$$E_B = h\nu - E_K \tag{2.1}$$

where $h\nu$ is the photon energy of the incident X-rays. The binding energy of an electron refers to the change in energy of the atom from its ground state E_0 to the state after the electron is emitted E_+, such that

$$E_B = E_+ - E_0. \tag{2.2}$$

Since energy is conserved, the energy of the atom before and after the emission is equal,

$$E_0 + h\nu = E_+ + E_K. \tag{2.3}$$

Combining equations 2.2 and 2.3 gives equation 2.1 as a result. This is however only applicable to measurements in the gas-phase, since otherwise the work function of the sample ϕ_{sa} must also be included. This is the potential barrier at the surface of the sample which the electron must overcome for it to be emitted, and corresponds to the difference in energy between the vacuum and the Fermi levels, E_V and E_F respectively. In the gas-phase, the vacuum level is set as the reference of the electron energy at which the binding energy is equal to "0 eV", and often instead referred to as the ionisation potential. Here, the electron is assumed to be at rest and infinitely far away from the considered system [133]. However, with solid samples, the Fermi level is used as a more convenient reference.

Therefore, from Figure 2.1, it can be seen that

$$h\nu = E_B^F + E_K^{sa} + \phi_{sa} \tag{2.4}$$

with E_B^F representing the binding energy of the core electron and E_K^{sa} the kinetic energy of the photoelectron after leaving the sample. This value is, however, different from that of the kinetic energy of the electron measured by the detector E_K^{sp}. Equally, the work functions of the sample ϕ_{sa} and the spectrometer ϕ_{sp} are also different. A common Fermi level can be established for both the sample and the spectrometer, but only with the assumption that the sample and spectrometer are in good electrical contact. This therefore cannot apply to measurements of the gas phase or other samples which are electrically insulating and thus do not allow for charge transfer between the spectrometer and the sample. Figure 2.1 therefore

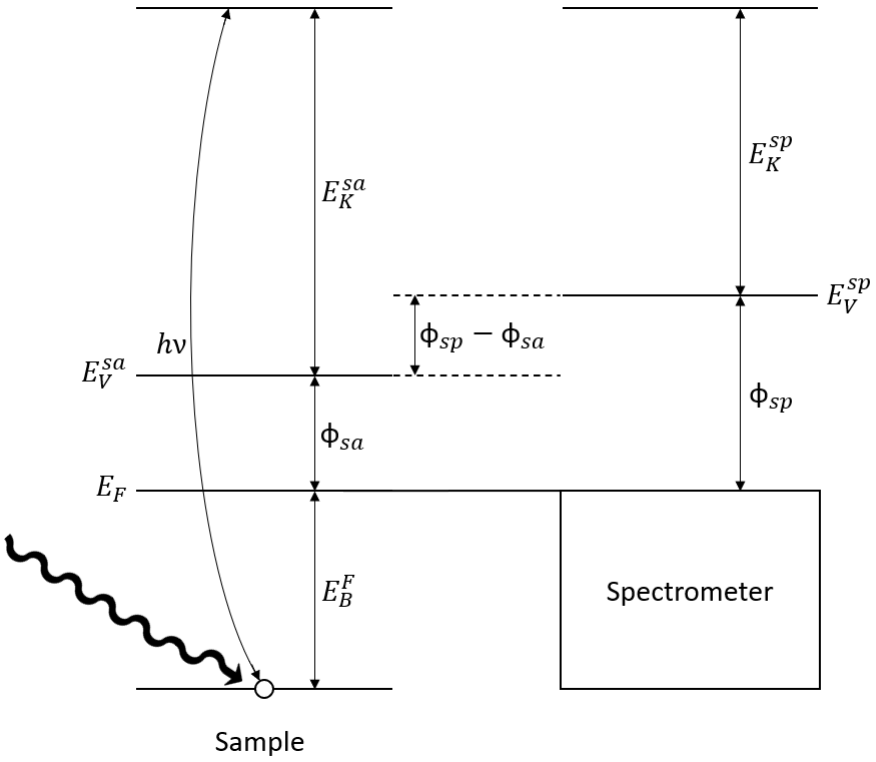

Figure 2.1: Energy level diagram for a sample in good electrical contact with the spectrometer, such that the Fermi levels E_F are aligned. The binding energy of the core electron E_B^F can be determined from the measured kinetic energy E_K^{sp} and the constant spectrometer work function ϕ_{sa}.

shows that

$$E_K^{sa} + \phi_{sa} = E_K^{sp} + \phi_{sp} \tag{2.5}$$

and so equation 2.4 then becomes

$$E_B^F = h\nu - E_K^{sp} - \phi_{sp}. \tag{2.6}$$

The binding energy of the photoelectron E_B^F (more commonly written simply as E_B) is therefore independent of the sample work function ϕ_{sa}, which is desirable since it is not constant. The work function of the spectrome-

ter ϕ_{sp}, on the other hand, is constant. This value can be set during the calibration of the equipment, and with the energy of the X-ray photons also known and constant, the binding energy of the photoelectron may be calculated from the measured kinetic energy alone.

2.1.2 Detection of the Photoelectrons

Emitted electrons pass through an electrostatic lens system, where they are decelerated by a retarding voltage V_i and focused through a slit and into the analyser. The most common analysers, and all of those used in this thesis, consist of two concentric hemispheres (Figure 2.2), each with a set voltage, V_{in} and V_{out}. The difference between these voltages results in an electrostatic force exerted on the electrons that are passing between the hemispheres. For the electrons to pass all the way through the analyser and reach the detector, they must have a centripetal force F_C roughly equal to that of the electrostatic force. This is related to their kinetic energy by the equation

$$F_C = \frac{E_K}{r} \tag{2.7}$$

where r is the radius of the arc along which the electrons travel. If the centripetal force of the electron is too great or too small, it will instead collide with one of the hemispheres. In an ideal scenario, the radius of the detected electrons is given by $R_0 = (R_{in} + R_{out})/2$, where R_{in} and R_{out} are the inner and outer hemisphere radii, respectively. The energy of these electrons is known as the pass energy E_{pass}, which is linked to the hemisphere voltages and radii through the relationship

$$e(V_{out} - V_{in}) = E_{pass}\left(\frac{R_{out}}{R_{in}} - \frac{R_{in}}{R_{out}}\right) \tag{2.8}$$

with e the charge on an electron. In practice, the detected electrons will travel along arcs with radii varying slightly from R_0 and thus have energies which vary from E_{pass}, in the range of $E_{pass} \pm \Delta E$. The detector, commonly made up of a microchannel plate (MCP), a phosphorescent screen and a charge-coupled device (CCD), is able to simultaneously detect all electrons within this energy range. E_{pass} is chosen by the user of the apparatus and is acquired by deceleration of the photoelectrons in the lens system. The value is selected based on the type of measurement required. Higher pass energies allow for higher count rates, a wider range of electron energies to be detected, and so decreased measurement times. This stems from the fact that the range $2\Delta E$ is proportional to E_{pass} and means that higher pass energies result in a lower energy resolution. This is also related to the geometry of the analyser used through the relationship

$$\frac{\Delta E}{E_{pass}} = \frac{W}{2R_0} \tag{2.9}$$

where W is the sum of the entrance and exit slit widths. Selected pass energies will almost always lie within a range of 5 eV to 200 eV, with the trade-off between measurement time and resolution the main consideration. Desired kinetic energy ranges of the photoelectrons can then be probed by scanning the retarding voltage in the lens system V_i and the voltages of the two hemispheres V_{in} and V_{out}, such that equation 2.8 is always satisfied for a chosen pass energy.

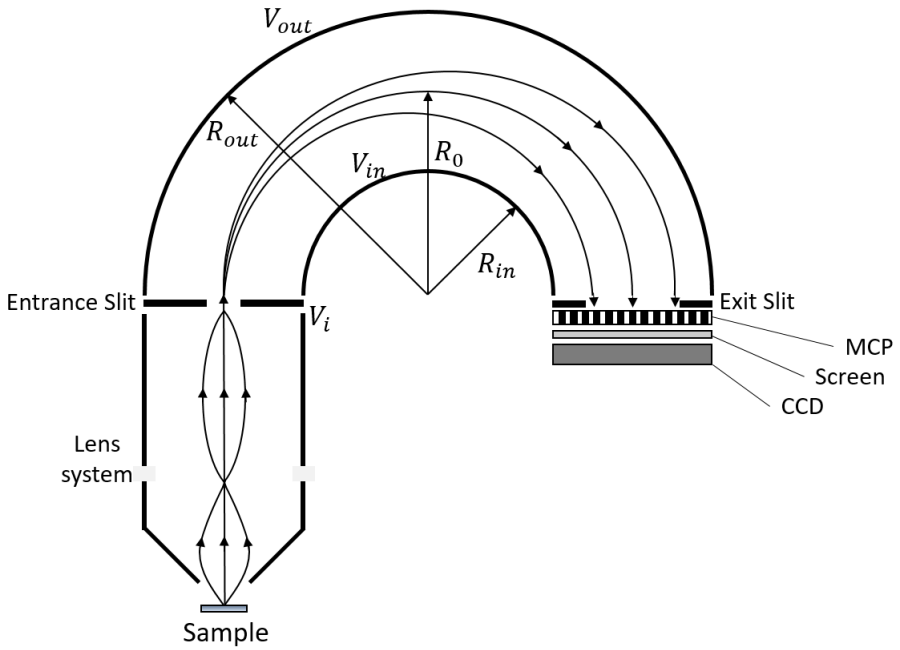

Figure 2.2: Analyser and detector setup for the standard concentric hemisphere analysers used in this study. Electrons emitted from the sample are focussed into the analyser entrance slit, and those with kinetic energies within the desired range will reach the exit slit for detection.

2.1.3 Surface Sensitivity

The surface of a sample represents a discontinuity between one phase and another, thus it has different physical and chemical properties than the bulk of the material. It is therefore useful to be able to analyse the surface and its various interactions with other matter. Surface sensitivity is a key component of XPS, and stems from the strong interaction of the photoelectrons - at energies of those involved in XPS - with atoms. Although the X-rays are able to probe into the sample in the micrometre range, only electrons within roughly the first 50 to 70 Å are able to escape the sample and be detected [7]. The photoelectrons interact with matter mainly through inelastic collisions; their inelastic mean free path $\lambda(E)$ is a function of the energy of the electron. For elemental solids, this relationship has been derived experimentally [5] such that $\lambda = \frac{143}{E^2} + 0.054E^{1/2}$. This is often referred to as the "universal curve" since it is similar for most solids

[134]. Similar relationships have also been derived for inorganic and organic compounds in reference [5]. The inelastic mean free path (IMFP) is then defined as the average distance traversed by an electron between two successive inelastic collisions [135]. It is also defined as the distance travelled through a material which attenuates the electron intensity by $\frac{1}{e}$, such that the exponential relationship for the measured intensity I of electrons that pass through a material of thickness d is given by

$$I = I_0 \exp\left(-\frac{d}{\lambda(E)}\right) \tag{2.10}$$

where I_0 is the initial intensity of the electrons. Electrons which escape with no further energy losses give rise to peaks characteristic of the core orbital from which they came, while those which do suffer losses, but are still detected, contribute to the background of the spectrum. Characteristics of XPS spectra are explained in more detail in Section 2.1.4.

A general relationship for the ratio of electrons emitted from a certain thickness d is therefore given by

$$\frac{I_d}{I_{total}} = 1 - \exp\left(-\frac{d}{\lambda(E)}\right). \tag{2.11}$$

The term 'probing depth' is often used to denote the thickness of the sample surface responsible for 95% of the total detected electrons. The remaining 5% come from deeper within the sample [136]. By substituting this value into equation 2.11 and rearranging, the simple relationship $d_p \approx 3\lambda(E)$ is obtained. As an example, for an electron energy of 1000 eV, the IMFP can be calculated from the "universal curve" [5] to be around 2 nm, thus giving a probing depth of approximately 60 Å. This relationship is, however, only

true for the case where the sample surface normal is parallel to the direction of the analyser entrance slit (Figure 2.3). The general relationship is instead given by $d_p \approx 3\lambda(E)\cos\theta$, where θ is the angle between the surface normal and the entrance slit, such that the extra distance the electrons must travel is taken into account. This angle can therefore be varied to a "grazing" angle to alter the desired probing depth, with larger angles leading to measurements of electrons which are on average emitted from layers closer to the surface [137].

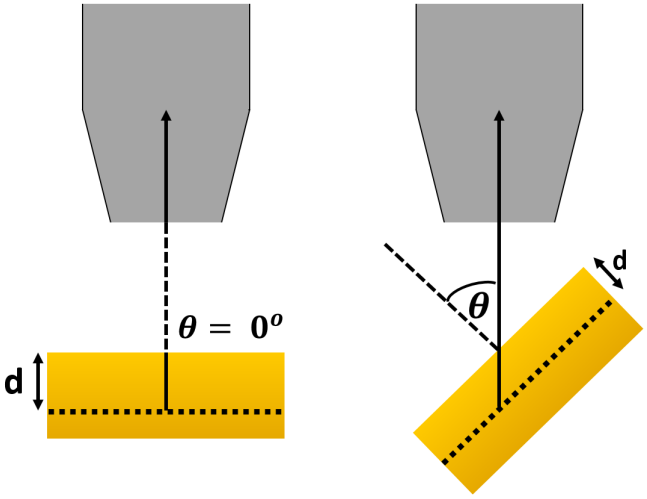

Figure 2.3: The thickness of the sample responsible for 95% of the total detected electrons d decreases as the angle θ between the surface normal and the analyser entrance slit increases, thus increasing the surface sensitivity of the technique. The sample is represented by the gold rectangle.

2.1.4 Interpretation and Analysis of Spectra

Electrons ejected from core levels have characteristic binding energy values which show as peaks in spectra. In a generalised application of Koopmans' Theorem, these represent the difference in energies of initial and final states of the atom from which they are emitted [138]. As stated in Section 2.1.1, the values can be calculated from the detected kinetic energies of the electrons. For the most basic analysis, the calculated energies are compared

to known values for the identification of elements present within the measured sample. However, initial and final state effects must be considered for a more detailed analysis. Initial state effects include things that happen before the photoionisation event, while final state effects include the way in which the atom responds to it.

2.1.4.1 Initial State Effects

Chemical Shifts

Small shifts from the characteristic core level binding energies can show the chemical environments of the atoms and their oxidation states. These shifts in the positions of the spectral peaks are known as chemical shifts and occur as a result of variations in charge densities and electronegativities of the atoms involved. For example, for an atom bonded to one with a high electronegativity e.g. fluorine, electrons will be drawn away from the atom of interest. This leads to poorer screening of the core hole left after photoionisation, such that Coulombic attraction will decrease the kinetic energy of the electron leaving the atom. The spectral peak produced will therefore lie at a slightly higher binding energy when compared to that if the atom was not bonded to the highly electronegative neighbour, fluorine.

Photoionisation Cross-section

Each orbital in an element has a specific photoionisation cross-section, based on its inherent properties, which determines how 'visible' it is to the incident X-ray and thus the probability that the electrons within it will interact. This affects the intensity of the measured spectral peak after detection. In fact, by using the known value for a given orbital of an

element and incident photon energy, and dividing the relative area of the peaks by that value, the relative amounts of each element at the surface of the sample can be determined.

Example Calculation

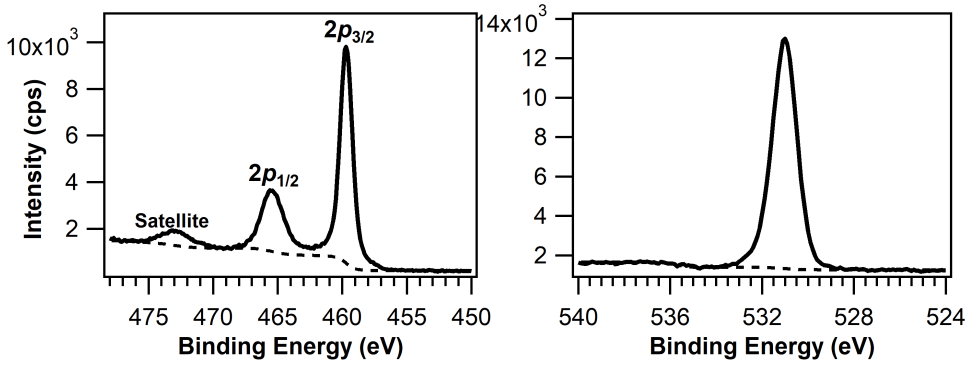

Figure 2.4: XPS spectra showing the intensity in counts per second versus the Binding Energy in eV for a clean TiO_2 crystal. Ti $2p$ (left) and O $1s$ (right) regions were measured with an X-ray photon energy of 1486.6 eV. Shirley backgrounds (dashed line) were subtracted from the raw data to allow the areas under the plots to be calculated in each case.

As an example, XPS measurements were performed using a lab-based monochromatic Al Kα source (photon energy = 1486.6 eV) and a Phoibos 150 NAP hemispherical analyser on a clean titanium dioxide (TiO_2) crystal, for the Ti $2p$ and O $1s$ regions (Figure 2.4). After a Shirley background subtraction, a process described in Section 2.1.4.3, the areas under the peaks of the Ti $2p$ and O $1s$ regions were calculated to be 22298 and 16950 arbitrary units respectively. At a photon energy of 1486.6 eV, the photoionisation cross-sections of Ti $2p$ and O $1s$ are 0.1069 and 0.04004 Mbarn respectively [139, 140]. By dividing the area by the cross-section in each case and comparing these values, a 1:2 ratio of Ti to O is found. The calculation is shown below:

$$\text{Ti}: \ 22298/0.1069 = 208587.5...$$

$$\text{O} : 16949.7/0.04004 = 423319.2...$$

$$\therefore \text{O/Ti} : 423319.2.../208587.5... = 2.03... \approx 2$$

2.1.4.2 Final State Effects

Spin-orbit Coupling

A key example of a final-state effect is spin-orbit coupling, which leads to the splitting of peaks. Photoelectrons emitted from atomic orbitals with an orbital angular momentum quantum number l greater than 1 - i.e. p, d, f but not s – will have different kinetic energies dependent on their spin vector s. For electrons, $s = \frac{1}{2}$, and so the total angular momentum quantum number $j = l \pm \frac{1}{2}$ and depends on the spin of the photoemitted electron. If the photoemitted electron spin is parallel to the orbital angular momentum vector, the total angular momentum quantum number $j = l + \frac{1}{2}$. If the electron is anti-parallel, $j = l - \frac{1}{2}$. For this reason, the corresponding XPS signals occur as spin-split doublets. As a result of Hund's rules, the electrons with parallel spin are more easily removed, and thus have higher kinetic energies and lower binding energies than those with anti-parallel spin [141]. The degeneracy associated with the interaction is equal to $2j + 1$ and determines the ratio of the areas of the XPS peaks. All of the values for each orbital angular momentum quantum number l are shown in Table 2.1. As an example, for photoelectrons emitted from a Ti $2p$ orbital, two peaks representing Ti $2p_{3/2}$ and Ti $2p_{1/2}$ will be seen (Figure 2.4). The Ti $2p_{3/2}$ peak will be at a lower binding energy and have twice the area of the Ti $2p_{1/2}$ peak.

Table 2.1: Corresponding total angular momentum quantum numbers, degeneracy values and XPS peak ratios for given atomic orbitals

Atomic orbital	j	Degeneracy	Ratio of Peaks
s ($l = 0$)	$\frac{1}{2}$	0	-
p ($l = 1$)	$\frac{1}{2}, \frac{3}{2}$	2,3	1:2
d ($l = 2$)	$\frac{3}{2}, \frac{5}{2}$	4,6	2:3
f ($l = 3$)	$\frac{5}{2}, \frac{7}{2}$	6,8	3:4

Peak Shape

The shape of the peaks themselves is also important for the analysis of spectra. Peak broadening due to experimental processes, including the spectrometer and sample environment, leads to a Gaussian contribution to the shape, while the inherent core hole lifetime, estimated from Heisenberg's uncertainty principle, produces a Lorentzian contribution [142]. The use of a convolution of these contributions, known as a Voigt function, is the most accurate method when fitting the peaks. Although, to reduce computational expense, these are usually approximated to give pseudo-Voigts [143]. In some cases, the peaks may be asymmetric in shape. This 'Doniach-Sunjic' contribution occurs as a result of interactions between conduction band electrons and the accompanying core holes [144], adding an exponential tail to the higher binding energy side of the peak. A finite version of this tail with an arbitrary cut-off can be used reasonably to include this contribution into the fit. This asymmetry is typically only observed for metallic samples.

Auger Decay

Another final state effect is Auger decay. This is where, after the initial electron emission, another electron in the atom decays to fill the hole left

and stabilise the ion. In doing so, a photon is released which can give energy to another electron within the ion to be emitted and detected in a process known as "autoionisation" [145]. This secondary electron is known as an Auger electron. A photon can also be emitted without transferring its energy to an electron in a process known as fluorescence. Auger electrons can be identified by their characteristic kinetic energies, and where their peaks appear on a binding energy spectrum will depend on the photon energy of the incident X-rays according to Equation 2.1.

Another form of Auger decay is known as Coster-Kronig decay. This occurs when the core hole left after an Auger emission event is within the same shell as the initial vacancy. In first row transition metal spectra, this leads to a broadening of the $2p_{1/2}$ peak, but not the $2p_{3/2}$ peak. This difference in widths of the doublet peaks is known as the Coster-Kronig effect. It occurs due to the process being very rapid specifically for decay between $2p$ orbitals, and thus a decreased lifetime in the $2p_{1/2}$ core hole causes the peak to broaden [146]. It should be noted, however, that this has more recently been disputed [147], with the apparent broadening of the $2p_{1/2}$ peak in Ti instead attributed to the presence of XPS intensity distributed over many unresolved final states for a Ti $2p_{1/2}$ peak core hole, dominated by shake satellites which involve symmetry flip valence excitations. Super Coster-Kronig decay, where instead two final state holes are within the same shell as the initial vacancy, is also possible but is very uncommon and so rarely a cause for concern. Photoemission, fluorescence, Auger emission and Coster-Kronig emission are illustrated in Figure 2.5.

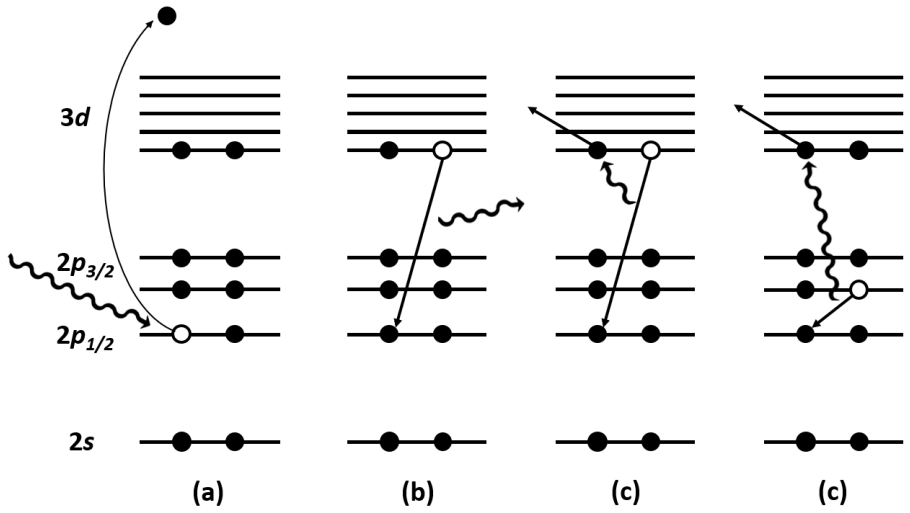

Figure 2.5: Energy level diagrams for Ti $2p$ to show the movement of electrons during (a) Photoemission (b) Fluorescence (c) Auger emission (d) Coster-Kronig emission. Ti $1s$, $3s$, $3p$ and $4s$ orbitals have been left out for ease of understanding. Filled and open circles represent electrons and holes respectively.

Satellites

The appearance of satellites is another type of final-state phenomena observed in the spectra. When photoelectrons leave the sample, they can transfer energy to other electrons and excite them to vacant states of higher energy. For instance, this can involve exciting electrons from the valence band to the conduction band, or from the highest occupied molecular orbitals (HOMOs) to the lowest unoccupied molecular orbitals (LUMOs). The loss in kinetic energy of the original photoelectrons causes peaks to emerge at a higher binding energy than that of the main structure. These are called "shake-up" satellites. If the excited electron is instead ejected from the ion completely, it appears as a broadening of the core-level peak or simply contributes to the inelastic background. This is known as a "shake-off" satellite. For clean surfaces, and usually those of metals, the emitted electron can excite collective oscillations in the conduction band. These "plasmon excitations" appear as a series of satellite peaks on the

higher binding energy side of the main photoemission peak that reduce in intensity as the binding energy increases. In some cases where the chemical environments cannot be easily identified from core-level peak fitting alone, the satellite configuration may instead be used.

Sample Charging

For samples that are insulating, including metals with thick surface oxide layers, emitted photoelectrons may not be sufficiently replaced by electrons from the bulk, leading to a build-up of positive charge on the sample surface. A Coulombic interaction with the emitted electrons then causes them to have lower kinetic energies by the time they reach the detector. As a result, spectral peaks shift to higher binding energies [136]. To correct for this during analysis, the binding energy of each peak can be calibrated to one with a known value from literature. The most common example, due to its presence on almost all samples that have been exposed to air, is to correct the adventitious carbon peak such that it lies at a binding energy of 284.4 eV [148]. Each other peak can then be corrected by the same binding energy value that was required to move the observed adventitious carbon peak to the reference value, such that the spectrum is calibrated.

2.1.4.3 Background

Peaks in an XPS spectrum sit on a background. This is formed of electrons excited by the X-ray Bremsstrahlung radiation (produced as electrons are decelerated in the anode of the X-ray source) [136] at lower binding energies, and those inelastically scattered at higher binding energies. As explained in Section 2.1.3, photoelectrons nearest to the surface of the sample are likely to be detected without losses due to collisions, and so will form

the characteristic peaks of the spectrum. Those deeper within the sample will suffer kinetic energy losses and instead add to the background on the higher binding energy side of the peaks. Since this is the case for each peak on the spectrum, these inelastically scattered photoelectrons will cause an accumulation of the background in a step-like structure as the binding energy increases. For spectra to be quantitatively analysed, the background must be accounted for via a subtraction. There are several subtractions which may be appropriate, including linear and polynomial subtractions. However, perhaps the most accurate and thus the most commonly used are Shirley and Tougaard subtractions. The Shirley subtraction is an iterative calculation between two points on the spectrum which assumes that the background at a certain kinetic energy is proportional to the area of the peak above that energy [149, 150]. Shirley subtractions were used in Figure 2.4 in Section 2.1.4.1. The Tougaard subtraction was not used in this thesis, but differs from the Shirley method in that the background is taken over the whole spectrum, as opposed to two selected points [150, 151].

2.1.5 X-ray Generation

For the laboratory-based XPS performed in this thesis, X-rays were generated using an Omicron DAR 400 X-ray source consisting of an X-ray tube with a filament, that acts as a cathode, and an aluminium target anode. In an X-ray tube, current is passed through the filament until it is glowing, emitting electrons which are accelerated towards the anode by up to 20 kilovolts (kV). The electrons decelerate as they interact with electrons in the target and emit X-ray photons as a result. The X-rays produced contribute to a continuous spectrum of Bremsstrahlung radiation, as well as far more intense emission lines characteristic of electron transitions within the

aluminium via fluorescence (Figure 2.5b). For an aluminium anode, these characteristic X-rays have a fixed energy of 1486.6 eV and are directed at the sample using mirrors, lenses and sometimes a monochromator, while the Bremsstrahlung radiation is minimised in the analysis chamber with filters and windows [152].

Synchrotron radiation was also used as a source of X-rays in the studies in this thesis. In simple terms, at synchrotron facilities, electrons are accelerated with a linear accelerator to relativistic speeds, before entering large storage rings where they are controlled by many bending magnets. As these electrons change direction, they emit electromagnetic radiation with high a photon density [153], which are directed to beamlines located around the ring. Here, photons of the desired energy are selected and used for measurements in experimental endstations. With bending magnets alone, radiation emitted is spread out into a flat horizontal fan, meaning that only a small fraction of it will enter the beamlines. Instead, linear arrays of short dipole magnets with alternating polarity provide a means of maximising the photon flux [153]. These are known as insertion devices, consisting of wigglers and undulators. Working in much the same way, wigglers and undulators force the path of the X-rays to oscillate such that a continuous energy distribution of very intense radiation is produced.

Synchrotron radiation has several advantages over that produced using a lab-based source. The most significant stem from the fact that the energy distribution is continuous instead of discrete. For example, the tunable X-ray photon energy associated with synchrotron radiation enables the use of analytical techniques that would otherwise be impossible with discrete sources. These include X-ray Absorption Spectroscopy (XAS) and Resonant Photoelectron Spectroscopy (RPES), techniques that are described in more detail later in this Chapter (Sections 2.2 and 2.3). The surface sensi-

tivity of XPS can also be adjusted by using photons of different energies; higher energy X-rays will enable electrons deeper within a material to gain enough energy to escape a sample and undergo detection, effectively moving along the "universal curve" previously mentioned. Due to the relationship between the energy of the incident X-rays and the photoionisation cross-sections of elements, the latter can be maximised by adjusting the photon energy [139, 140]. Another advantage of synchrotron radiation is simply the intensity of the radiation itself, the quality of which is only comparable for lab-based sources if a very small photon spot size is combined with low pass energy measurements. Unlike X-rays from laboratory based sources, synchrotron radiation is also polarised. This means that XAS may also be used to probe molecular orientation, due to the spatial distributions of unoccupied molecular orbitals, and to probe along specific crystallographic directions in the case of single crystals.

The facility used for the studies in this thesis was the MAX IV synchrotron in Lund, Sweden. There are two storage rings at MAX IV, a 3 GeV ring and a 1.5 GeV ring with respective circumferences of 528 and 96 metres. In each case, the path of the electrons is precisely controlled with a complex system of bending magnets and undulators. This precise path, as well as the low pressures, and periodic accelerations applied to replace any energy losses, enable the electrons to exist for long periods of time in these rings. Two beamlines were used in this thesis, known as HIPPIE and FlexPES. Located on the larger ring, HIPPIE uses an elliptically polarizing undulator (EPU) as its X-ray source, while FlexPES, situated on the smaller ring, uses a linearly polarizing undulator (LPU). The two beamlines are described in full detail elsewhere [154, 155].

2.2 X-Ray Absorption Spectroscopy

X-ray Absorption Spectroscopy (XAS) is another technique used for sample analysis. Like XPS, X-rays are incident upon a sample, but as mentioned in Section 2.1.5, the photon energy is varied instead of fixed, hence the need for a synchrotron source. An XAS spectrum can be split into three distinct regions, each specified by their relation to the absorption edge of the element being probed. This is the energy at which there is a sharp rise in the absorption coefficient of X-rays by the element [156], corresponding to the incident photon energy which is equal to the binding energy of a core-level electron [157]. The three regions are the pre-edge region, which provides information on covalency and electronic structure, the near-edge X-ray absorption fine structure (NEXAFS), which enables identification of oxidation states and coordination symmetry, and the extended X-ray absorption fine structure, which is associated with the ligands involved [156, 158]. Only the NEXAFS were explored in this thesis. In NEXAFS, the photon energy is swept across the absorption edge for an orbital of interest, and when a photon energy matches that between an occupied and an unoccupied energy level, it is absorbed by a core-level electron, which is excited (Figure 2.6). This leads to another key difference from XPS, which probes the occupied energy states of an element, as NEXAFS probes unoccupied states. Since the photoelectron wavefunction is strongly dependent on the potential around the absorbing sample, the position of the absorption edge therefore changes as the charge of the absorber changes. The oxidation state of the sample can therefore be determined from this chemical shift in the edge position [158].

The decay events that follow absorption will lead to Auger or fluorescence emission, previously seen in Figure 2.5, which can be measured in several

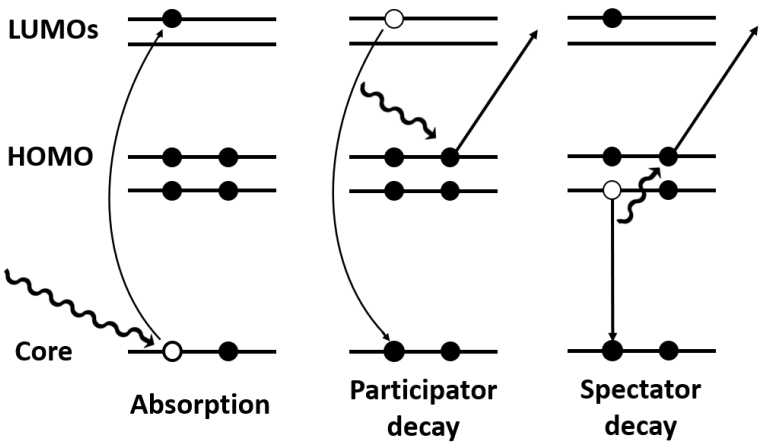

Figure 2.6: Energy level diagrams to show the movement of electrons during X-ray Absorption, Participator decay and Spectator decay. Filled and open circles represent electrons and holes respectively.

ways:

1. Total Electron Yield – Upon Auger or fluorescence emission, a current will therefore leave the sample, known as the drain current. This can be measured to give the total electron yield. When this is mapped as a function of the known photon energy, the spectrum produced provides information on the unoccupied energy levels. A disadvantage of this method is that all electrons other than the desired Auger electrons will also be measured, leading to significant background contributions from inelastic collisions and secondary electrons.

2. Auger Yield – The energy of the Auger electrons is measured using the analyser and plotted as a function of the changing photon energy. The data can then be integrated to produce an absorption spectrum. This is a complex and slow method, requiring longer measurements for noise reduction. However, it can be used to observe other peaks, such as those associated with direct photoemission, as they track through the kinetic energy window. This then enables the choice of an integration window that may avoid these peaks if required.

3. Partial Yield – The microchannel plate (MCP) detector allows electrons in, but by applying an opposing negative bias, electrons below a certain energy are unable to pass through to the analyser. This removes counts from background and inelastically scattered electrons, hence improving upon the Total Electron Yield method as well as the surface-sensitivity.

2.3 Resonant Photoelectron Spectroscopy (RPES)

Resonant photoelectron spectroscopy (RPES) is another technique which uses a varying photon energy. It essentially combines XPS and XAS, such that it can provide an XPS spectrum with enhanced intensities by using incident photon energies close to the absorption threshold of a core-level, as previously determined by XAS.

After absorption by a sample, the excited state can undergo two types of Auger decay: spectator and participator decay [145], each shown in Figure 2.6. In spectator decay, the core electron which is excited into the unoccupied state remains there while another electron relaxes to fill the core-hole, and an Auger electron is emitted. The 'spectating' electron in the LUMO provides shielding, which leads to an enhanced kinetic energy of the ejected Auger electron. This is the foundation for resonant Auger electron spectroscopy, which was not used in this thesis, so is not described in detail. In participator Auger decay, the previously excited electron does itself then relax from the LUMO to fill the core-hole, again leading to Auger emission of an electron from the HOMO. This time the emitted electron has a kinetic energy indistinguishable from that of a normal Auger electron and, since the incident photon energy is equal to that transferred to the electron in the

HOMO through relaxation, an electron detected after direct photoemission. The existence of participator decay can therefore only be inferred from the enhanced intensities of the HOMOs when measured at the excitation energies of the LUMOs [159]; at the photon energies where this decay and subsequent 'auto-ionisation' occurs, the intensity recorded is added to that from standard direct photoemission, such that higher intensities are recorded.

RPES measurements are often shown as a 2D map, where XPS measurements are taken as a function of photon energy over a constant binding energy window. An example is shown in Figure 2.7, where a Ti RPES map was measured for a clean rutile $TiO_2(110)$ single crystal. Details of the measurements are described in Chapter 6. The intensities can then be represented on a colour scale. For analysis, different features can be identified on the map. For example, diagonal bands of enhanced intensity represent constant kinetic energy features such as Auger peaks, horizontal bands correspond to resonant enhancement of the LUMO states, and vertical bands of high intensity on LUMO resonances represent enhancements of the HOMO states. The NEXAFS may also be recovered from such a map by integrating the intensity over the area corresponding to the enhancement of the Auger.

RPES is a particularly useful technique when molecules are deposited onto a sample surface, and thus charge transfer becomes a possibility. Using a molecule deposited on a metal substrate as an example: if the LUMO of the deposited molecule lies below the Fermi level of the metal, then charge transfer between the metal's occupied valence structure and the LUMO of the excited molecule can potentially occur before the core-hole is filled. There are three types of charge transfer which can occur, each shown in Figure 2.8, after which a specific decay process follows. For example, charge

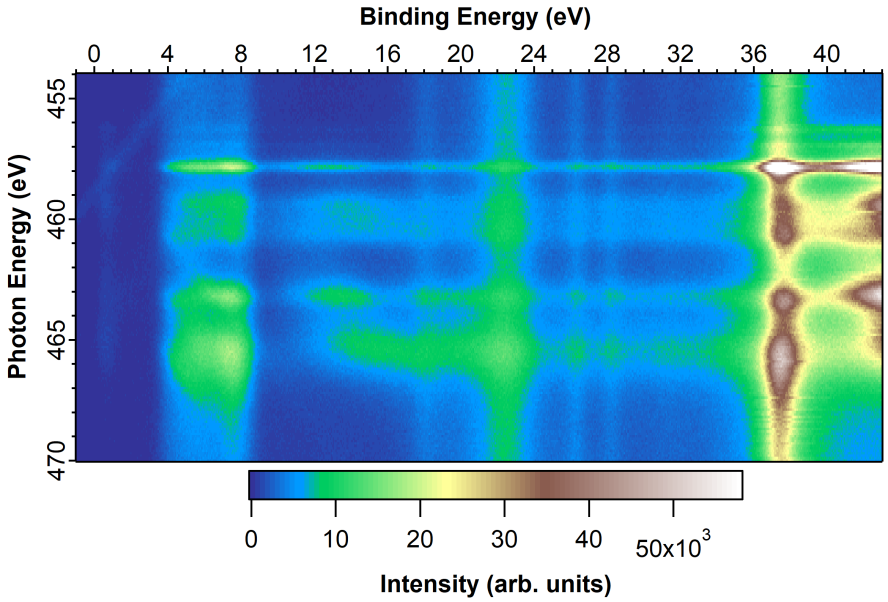

Figure 2.7: 2D Ti RPES map measured for a clean rutile TiO_2(110) single crystal, taken from the experiment described in Chapter 6.

transfer from the molecule to the metal (Figure2.8a) is followed by normal Auger decay. Following transfer of one or more electrons from the metal into the unoccupied levels of the molecule (Figure2.8b), these same electrons may relax while the excited electron in the molecule spectates, during what is known as "super-spectator" decay [160]. Bi-directional charge transfer (Figure2.8c), of the previously excited electron from the molecule into the metal and electrons from the metal into the unoccupied orbitals of the molecule precedes "super-Auger" decay [161], where the electrons originating from the metal undergo normal Auger decay.

The products of each decay mechanism may be distinguished using RPES, providing information on the charge transfer itself. For example, on the 2D maps of photon versus binding energy, constant kinetic energy bands that track back to the participator resonant enhancements represent super-spectator and super-Auger decay [159].

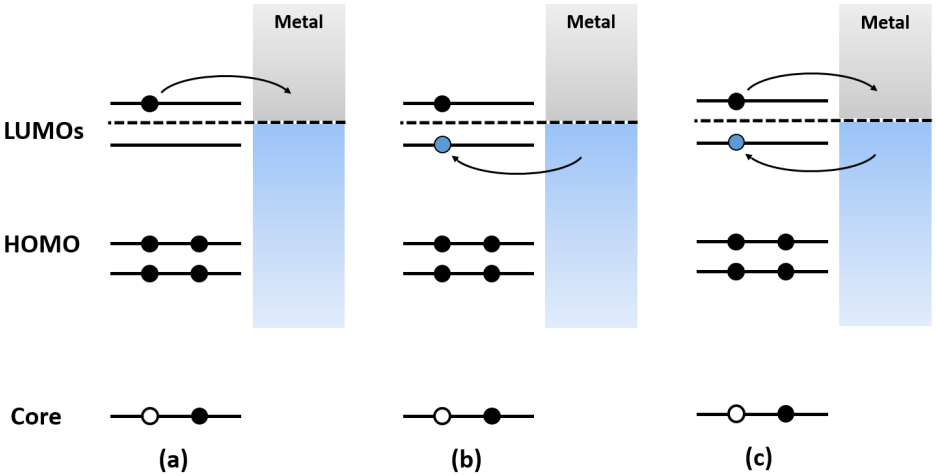

Figure 2.8: Energy level diagrams to show the movement of electrons during (a) molecule to surface charge transfer (b) surface to molecule charge transfer (c) bi-directional charge transfer. Filled and open circles represent electrons and holes respectively.The dashed line represents the Fermi level of the metal.

Chapter 3

Device for Sample Transfer Between Reaction and Analysis Conditions - Design and Build

Contents

3.1 Introduction

The "pressure gap" and , more generally, the difference in conditions required for reaction and analysis propose problems which have been addressed in Section 1.1.1. A method is required to enable the rapid transfer of a sample from reaction to analysis conditions, such that the measured results of analysis techniques including XPS could more accurately represent the actual behaviour of a sample under those reaction conditions. Additionally, it is important that the sample is not exposed to other unwanted elements such as air during the transfer, something that would again affect results. Many methods used to achieve these goals for various applications are described in the literature and have been summarised and assessed in Section 1.1 in this thesis. With the aim of improving upon these previous attempts, a design is presented in this Chapter; employing sample transfer through a differential pumping scheme, the system is made with the future analysis of solid-state hydrogen storage materials in mind. Targeted pressures of hydrogen required for on-board vehicular storage in the solid-state are around atmospheric and slightly above [22], therefore the aim of the system is to achieve these pressures in the reaction chamber while suitably low pressures are maintained in the analysis chamber such that XPS analysis can take place within just a few minutes of reaction.

In this Chapter, the process of this design and build from first principles through to the finished system is described and explained, with results from tests performed at each stage provided and discussed.

3.2 Methodology and Design

3.2.1 Overview and Differential Pumping

The final design of the device employs a stainless-steel transfer rod upon which a sample is mounted, such that it can undergo reactions with gases at pressures at and above atmospheric in the reaction chamber, before being moved through a series of connected differentially pumped chambers into the analysis chamber at UHV. Differential pumping is therefore the key phenomenon used to enable the rapid transfer.

For two connected chambers of differing pressures, gas molecules will flow down a pressure gradient from the higher pressure to the lower pressure chamber as a result of the kinetic theory of gases [162]. This will continue until the pressure of both chambers are at equilibrium. In order to maintain different pressures between the connected chambers, differential pumping is required. For the lower pressure chamber, the relationship between the speed at which gas is pumped out and the gas flow rate into that chamber will determine the pressure inside. As the pumping speed increases relative to the gas flow, intuitively, the pressure will decrease. Therefore, with sufficient pumping and a small enough flow rate, the pressure can be kept lower in one chamber than in the other it is connected to.

In examples described previously in Section 1.1.2, differential pumping enabled a pressure differential to be maintained between a reaction chamber and an analysis chamber, where connection via apertures was required for an electron beam to pass from sample to analyser [15, 16]. In another example, the connection between chambers of differing pressures was necessary instead for sample transfer [27], as is also the case for the design

presented here.

The gas flow between chambers may vary due to a number of factors; for example, the size of the aperture through which the gas passes, the amount of leakage allowed through a seal, and the size of the pressure gradient. In order to increase the latter past the limit allowed by the pumping speed and gas flow rate between just two chambers, intermediate chambers may be introduced. These extra differentially pumped stages in effect decrease the gas flow between the highest and lowest pressure chambers, by having neighbouring chambers with smaller pressure differentials and building the gradient more gradually.

The design and build of the final device was achieved through that of a series of prototypes, each tested until successful such that it could be built upon to create the next.

3.2.2 First Prototype

3.2.2.1 Design

The initial prototype design is shown in Figure 3.1. It consists of two 304L stainless-steel 4-way crosses with ConFlat (CF) flanges with outer diameters of 69.8 mm connected by a custom O-ring flange of the same size. The crosses each had an internal volume of 242 cm^3. 304L stainless-steel was used for all parts in the design unless otherwise specified, since it is able to withstand extreme temperatures, pressures and corrosive environments without deformation or damage, as well as having a low outgassing rate and being easy to clean, all while being a cost effective choice [163]. It is also highly resistant to hydrogen embrittlement, which will be important

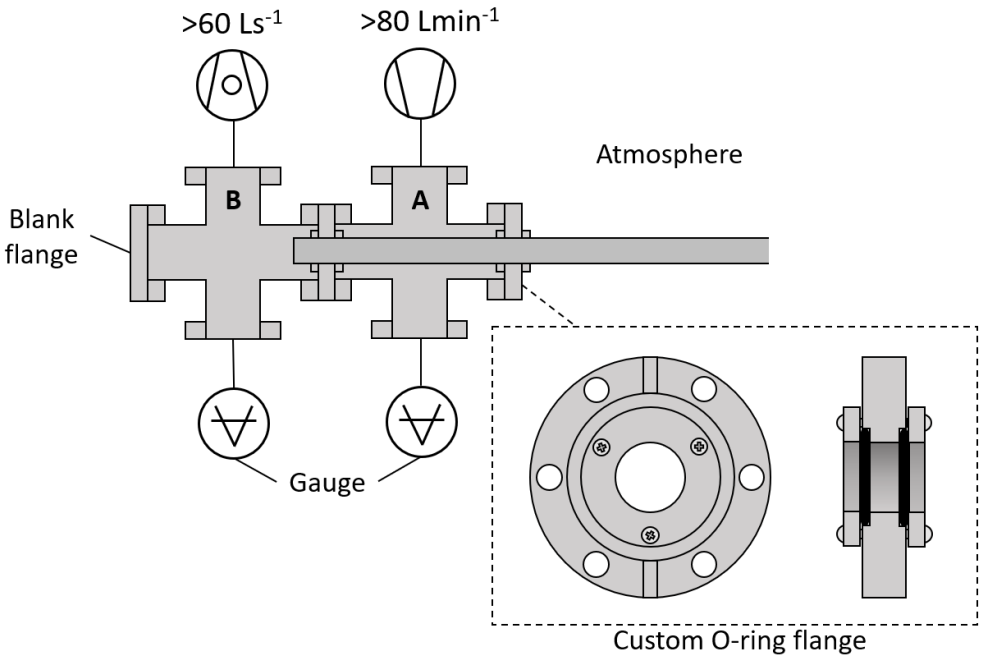

Figure 3.1: Design of the first prototype. Two cross-chambers are connected with custom O-ring flanges which are shown magnified in the dashed box. The right chamber (A) closest to the open atmosphere is pumped with a dry scroll pump, while the left (B) is pumped with a higher speed turbopump. The stainless-steel rod is present in both chambers such that the seals are maintained. Pressures in the chambers are measured with cold cathode Pirani gauges.

for maintaining safety during future studies of hydrogen storage reactions. One cross (B) has a blank CF flange on the end, while the other (A) is separated from the atmosphere by another custom O-ring flange. The custom O-ring flanges are vital to enable the differential pumping between the neighbouring chambers; a double-sided CF flange with a 20.5 mm diameter hole in the middle has Viton O-rings clamped to each side by aluminium rings which are screwed into the flange itself, allowing a 20 mm diameter rod to pass through the hole with the O-rings sealed tightly to its edge. The aluminium clamps have indents to keep the O-rings positioned around the hole in the flange. The O-rings themselves have inner and outer diameters of 20 and 23 mm respectively and ensure gas flow between neighbouring chambers is minimised while the rod is still able to slide horizontally in both directions. The O-ring material is Viton rubber, which is resistant

to a wide range of chemicals and can withstand temperatures in the range of –20 ^{o}C up to 210 ^{o}C [164]. This will become important if heating and cooling capabilities are eventually introduced in the reaction chamber. The O-rings are durable to reduce the need for replacement, but also relatively cheap should they need replacing after becoming damaged by the moving rod after repeated use. The rod is 1 metre long, as is required by the design of the final device, and is inserted into both cross chambers through the two custom O-ring flanges while the other end protrudes into the atmosphere. The corner on the end of the rod was lightly smoothed with sandpaper to prevent the sharp edge from damaging the O-rings as it passes through. Chamber A as shown in the Figure is pumped with an Agilent Technologies SH-110 dry scroll pump, while chamber B is pumped with a higher speed Pfeiffer HiPace 80 turbomolecular pump. The pressures in the chambers are measured with Pfeiffer PKR 361 cold cathode Pirani gauges, which measure in the range of 1×10^{-9} to 1×10^{3} mbar.

The aim of the prototype is to test the pressure gradient that is achievable between atmosphere and the differentially pumped neighbouring chambers, and thus the ability of the custom O-ring flanges to maintain a seal while allowing for rod movement.

3.2.2.2 Test Results

The pressures measured in chambers A and B while the rod is both stationary and moving are shown in Table 3.1. As expected, the pressures in both chambers were slightly higher for the moving rod, since the seals are disturbed by the movement. At all times the rod must protrude into both chambers such that the seal between is maintained. In both cases the pressure in the lowest pressure chamber, B, was approximately 7 orders of

magnitude lower than that of the open atmosphere. With just two differentially pumped chambers, this was a big enough differential to deem the custom O-ring flanges a success, such that an extended prototype could be developed with the same custom flanges, with the aim of reaching even lower pressures through the introduction of more chambers.

Table 3.1: Pressures recorded in Chambers A and B for the first prototype design, with both a stationary and moving rod

	Pressure in Chamber (mbar)	
	A	B
Stationary Rod	1.2×10^{-2}	3.4×10^{-5}
Moving Rod	3.4×10^{-2}	5.6×10^{-5}

It was found to be very difficult to move the rod in the direction of the open atmosphere. This was a result of the strong pressure gradient in the opposite direction and must be addressed in the next prototype; the rod must be easily moveable in both directions to allow the sample to be moved back from the analysis chamber to the reaction chamber or the open atmosphere.

3.2.3 Second Prototype

3.2.3.1 Design

The design of the next prototype is shown in Figure 3.2. One cross chamber remains to act as a 'dummy' analysis chamber (denoted AC in the figure). This is for the protection of a real analysis chamber from potential spikes in pressure during tests which may damage analyser electronics and introduce impurities. The other cross chamber from the first prototype has been replaced with a smaller flange chamber, with an outer diameter of 69.8 mm,

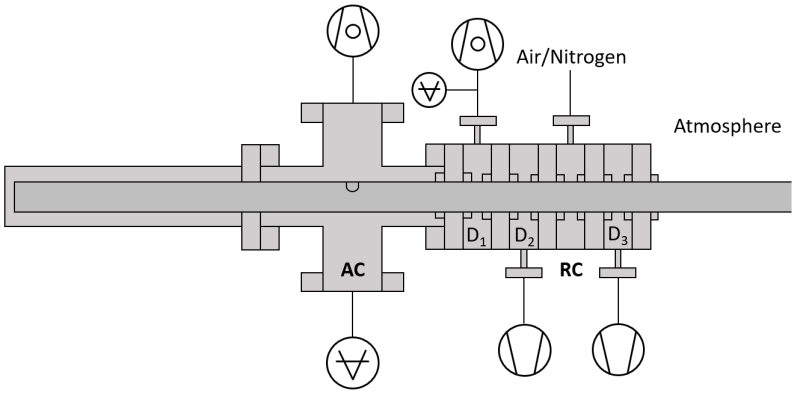

Figure 3.2: Design of the second prototype. A cross-chamber acting as a 'dummy' analysis chamber (AC) and a differentially pumped scheme of flange chambers are connected with the custom O-ring flanges. The reaction chamber (RC) lies between two pumped chambers, the right one (D_3) aiding rod movement in the direction of the open atmosphere.The inclusion of another turbopumped chamber (D_1) helps to increase the pressure gradient between the RC and the AC. The crescent shape on the rod represents a recess in which the sample is mounted.

a bore diameter of 37 mm and a thickness of 19 mm. The new chambers introduced for the reaction chamber (denoted RC in the figure) and the further differential pumping stages are also identical flange chambers. They are shown in more detail in Figure 3.3. These smaller chambers were chosen for the differential pumping stages as they decrease the distance required to move the sample from atmosphere to reaction to analysis and take less time to evacuate than larger chambers. The same chamber was chosen for the reaction chamber since smaller chambers require lower volumes of reactant gases to reach the same pressure, which can help to improve safety when dealing with gases such as hydrogen, and the smaller internal volume of the chamber leads to enhanced detectability of products and a reduced effect of impurities, as was seen in Section 1.1. The volume inside the chamber is 18.3 cm^3 and decreases further to 12.9 cm^3 when the rod is inserted. The minimum size of the chamber was limited by the size of the aluminium clamps on the custom O-ring flanges, which would prevent proper attachment either side of the chamber if they were to be touching. Nevertheless, this small volume compares favourably to those seen in the

literature (Table 1.1).

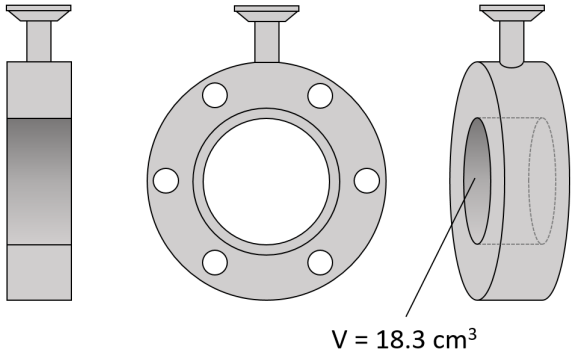

Figure 3.3: More detailed side (left), front (middle) and diagonal (right) views of the flange chamber introduced in the second prototype design. The internal chamber volume V = 18.3 cm^3 is favourably small when compared to those in the literature when used as a reaction chamber. The small width also allows for a shorter distance between reaction and analysis positions. The KF fitting on the top enables evacuation with a pump or the introduction of reactant gases.

As seen in Figure 3.2, there are now two differential pumping stages between the reaction chamber and the 'dummy' analysis chamber. The first is pumped again with an Agilent Technologies SH-110 dry scroll pump, and the second with a Pfeiffer HiPace 80 turbopump. The pumps are each connected to the chambers via Kleinflansch (KF) fittings. This increased pumping should enable a lower pressure to be reached in the 'dummy' analysis chamber, which is also pumped with a turbomolecular pump. The real analysis chamber will be pumped further with both a turbo and an ion pump, but it is also significantly larger than the cross chamber in the prototype. Another chamber on the other side of the reaction chamber is also pumped with a dry scroll pump. This is to address the issue of difficult rod movement in the direction of the atmosphere, balancing the forces to allow easier movement in both directions. It will also act as a buffer between the reaction chamber and atmosphere, such that any leakage of a reactant gas will be pumped away in this chamber before reaching the atmosphere, and thus improve safety. In the case of hydrogen, this is an important risk mitigation; if the hydrogen were to leak into the pumped chamber, it will

represent almost 100% of the total gas mixture in the chamber. This is far greater than the 75% higher flammability limit of hydrogen [165], such that there is no risk of ignition. The pump can be connected to a suitable means of ventilation, where it can be released into a massive volume; making up a negligible percentage of the total gas mixture present, any risk of hydrogen ignition is again mitigated. The chamber will also help to prevent leakage of air from the atmosphere into the reaction chamber, thus reducing the level of impurities introduced.

A sample recess was cut into the transfer rod at a position 33 cm from one end. This allows for it to be present in the open atmosphere, while the remainder of the rod protrudes into the 'dummy' analysis chamber, and as such all seals are always maintained. This is an important feature of the design; the sample may be mounted in atmosphere and moved directly into the analysis chamber, providing a rapid form of sample transfer when compared to a traditional load-lock approach - even when no reaction is taking place in the reaction chamber. A length of tubing was required on the left-hand side of the cross chamber such that the rod can be fully inserted with the sample recess in the centre of the chamber, or the 'analysis position'. The recess itself is $9 \times 14 \times 2$ mm such that it fits between O-rings when passing through the custom flanges. Importantly, this width is small enough that it will not straddle neighbouring chambers, which would bridge the seal and cause the pressures to equilibrate. A very small volume of gas is expected to be taken in the recess from the higher to lower pressure chambers, but this should prove negligible in the analysis chamber once it has passed through the other pumping stages. The recess allows for flat samples, with a maximum thickness of 2 mm, to be mounted simply onto carbon sticky tape, but no part can extend outside of the recess, as the sample would be damaged while passing through the flanges. The recess

edges were also smoothed to again prevent damage to the O-rings during rod movement.

3.2.3.2 Test Results

Without a sample present in the prototype, pressures in the 'dummy' analysis chamber and final differential pumping stage (D_1) were measured as the rod moved between key sample positions. These include the rod being stationary in the open atmosphere, then moving into the reaction chamber, moving into the 'dummy' analysis chamber, and again back into the reaction chamber. This was repeated with varying pressures of nitrogen in the reaction chamber, up to a maximum of 4.5 bar. The maximum pressure was limited by that of the nitrogen supply available. Nitrogen was used for the increased pressure tests since it is an inert gas with low safety risks should there be a leakage. The nitrogen was connected to the reaction chamber via the KF fitting, which was sealed with a KF trapped centering ring with outer ring and O-ring and a clamp. It was important to measure the pressures in the chambers when the sample was moved from the reaction chamber back to the analysis chamber, as this is a useful technique for investigating a sample undergoing repeated reactions. In the case of solid-state hydrogen storage materials, their stability under multiple cycles of hydrogenation and dehydrogenation is a significant property, and one which could be readily examined with this system.

The aim of the test was to determine the ability of the system to maintain a low enough pressure in the analysis chamber during the various processes involved with the sample transfer and analysis. A maximum acceptable pressure in an analysis chamber is deemed in this study, with this apparatus, as 1.0×10^{-5} mbar. This pressure will still allow the detection of

emitted electrons, while sample contamination by impurities is also limited. Lower pressures are of course more desirable, but are compromised in this case for the speed of analysis after reaction. The results are shown in Figure 3.4.

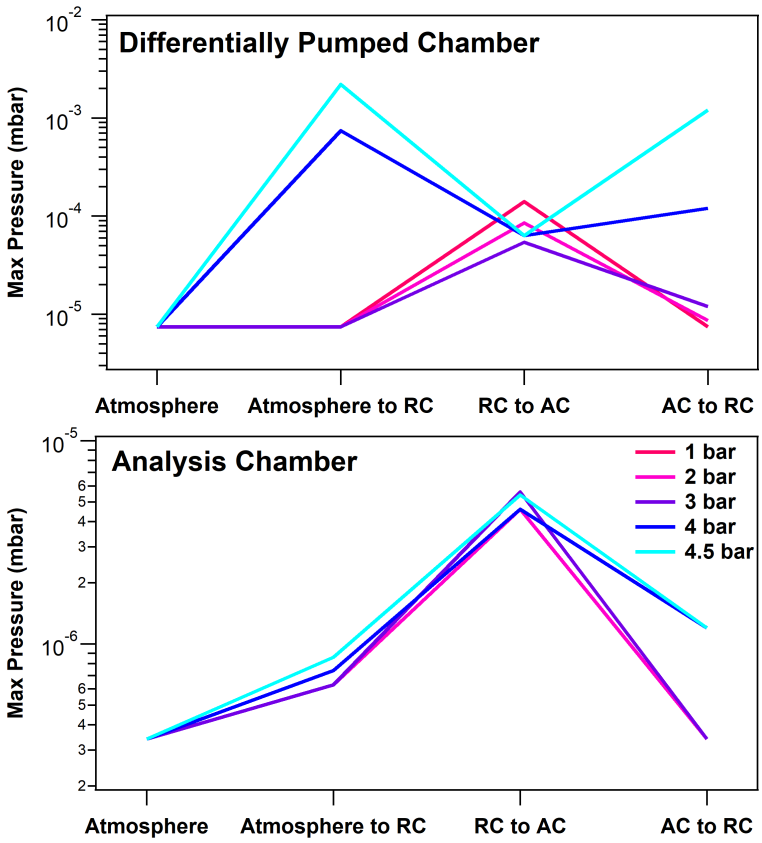

Figure 3.4: Logarithmic plots showing the maximum pressure reached in the differentially pumped chamber D_1 (top) and the 'dummy' analysis chamber (bottom) as the sample recess is moved from the open atmosphere to the reaction chamber (RC), to the cross-chamber (AC), and back to the reaction chamber. These processes were repeated with nitrogen in the reaction chamber at a range of pressures from 1 to 4.5 bar, each shown by a different coloured line.

The differentially pumped chamber reached a maximum pressure of 2.2×10^{-3} mbar while the reaction chamber contained 4.5 bar of nitrogen and the sample was moved from atmosphere into the reaction chamber. The seal between this pumped chamber and the 'dummy' analysis chamber was sufficient in all cases for a significant pressure differential to be maintained. The highest pressure was measured in the 'dummy' analysis chamber during

transfer of the sample recess from the reaction chamber to the analysis chamber itself; 5×10^{-6} mbar was recorded with pressures of 3 and 4.5 bar in the reaction chamber. This pressure was similar for all reaction chamber pressures and confirmed that the differentially pumped system was successful in preserving an acceptably low pressure in the analysis chamber at all times. The system could now be transferred to a real analysis chamber and used for experiments.

3.2.4 Final System

3.2.4.1 Design

The final system design is shown in Figure 3.5, where the cross-chamber has been replaced with a real analysis chamber. Spacers on each end of the analysis chamber enable the sample to be in positions for mounting in atmosphere (C), reaction (B) and analysis (A) while all seals are maintained at all times, and the rod does not approach the mounted turbopump too closely. Any contact would cause severe damage to the pump, which makes use of a series of rotary blades spinning at 1500 Hz.

The analysis chamber, as previously mentioned, is pumped again by a turbomolecular pump but also by a Varian 54 noble diode ion pump. This should enable even lower pressures to be achieved in the chamber, which is now a significantly large volume. A valve present between the analysis chamber and the differential pumping scheme allows for maintenance of the system, including full rod removal and O-ring replacement, while the analysis chamber can remain at UHV.

Once mounted in the recess and positioned in the analysis chamber, the

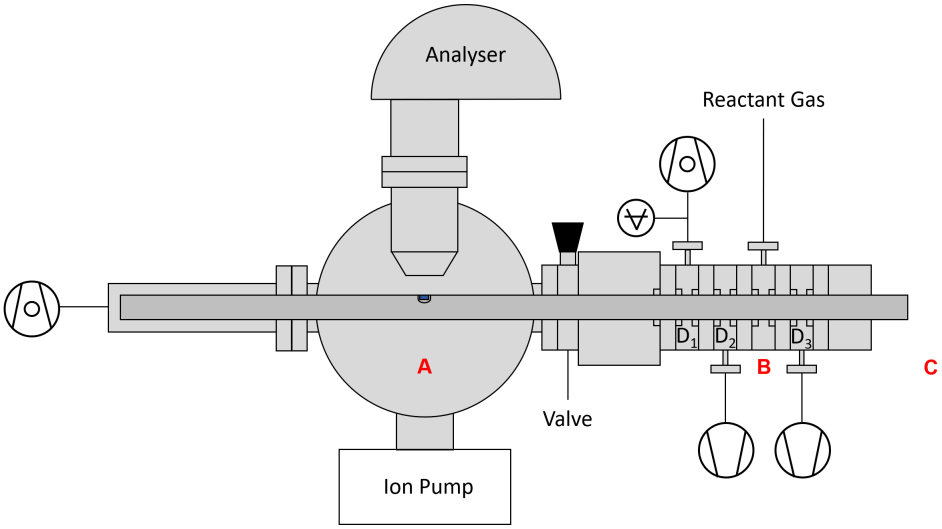

Figure 3.5: Final system design; the differentially pumped transfer system is installed on a real analysis chamber. A Varian 54 noble diode ion pump maintains UHV in the large analysis chamber, while the valve allows for rod removal and system maintenance. The rod is shown in the analysis position A, while B and C represent positions for reaction and sample mounting respectively. The system is designed such that all seals are maintained when the sample is in each of these key positions. The Scienta Omicron R3000 hemispherical analyser combined with an Omicron DAR 400 X-ray source enables XPS analysis.

sample can be manipulated horizontally and rotated through a full 360-degree range. This allows the grazing angle, as explained in Section 2.1.3, to be easily adjusted for variation of surface-sensitivity in the XPS analysis. It can also be repositioned in the analysis chamber should other instruments be used on the sample, such as an ion gun used for sputtering, which is described in more detail in the next chapter. The vertical position of the analyser entrance slit lies 45 mm above the sample position, the working distance of the Scienta Omicron R3000 analyser used on the system, and was positioned with the use of a spacer. In principle, small changes to this distance are sometimes needed to optimise the measured counts when using samples of different thicknesses. This would then appear to be a limit of the design, but since it is already limited to the use of only flat, thin samples, the lack of adjustment in this axis is not a major concern. The analyser itself consists of an MCP detector and a CCD camera detection system.

The Omicron DAR 400 X-ray source is mounted onto the analysis chamber at a 45-degree angle relative to the position of the analyser entrance slit such that the X-rays are emitted approximately 150 mm from the sample. This distance can however be varied to maximise the detected electron count using an adjustable bellows.

The stainless-steel transfer rod is grounded by contact with the stainless-steel parts of the custom flanges, but this is checked before experiments are performed; a lack of grounding would cause sample charging and thus affect the measured binding energies of peaks during XPS analysis.

A more detailed depiction of the chambers and flanges in the differential pumping section of the system is shown in Figure 3.6. The chambers and custom O-ring flanges are connected via 6 mm threaded rods which extend all the way through into a wider flange at the end, where the rods are screwed tightly. The connections are tightened as much as possible by nuts at the other end. The end flange also has threads protruding into the other side to allow for the connection of an add-on designed for use with air-sensitive samples. This is described in the next section.

An experiment carried out using the unique capabilities of this system is described in the following chapter, providing a 'proof of concept' for the device.

3.2.5 Add-on for air-free transfer

3.2.5.1 Design

As explained in Section 1.1.3, sometimes it is necessary to investigate samples without having them exposed to air. A method of air-free transfer

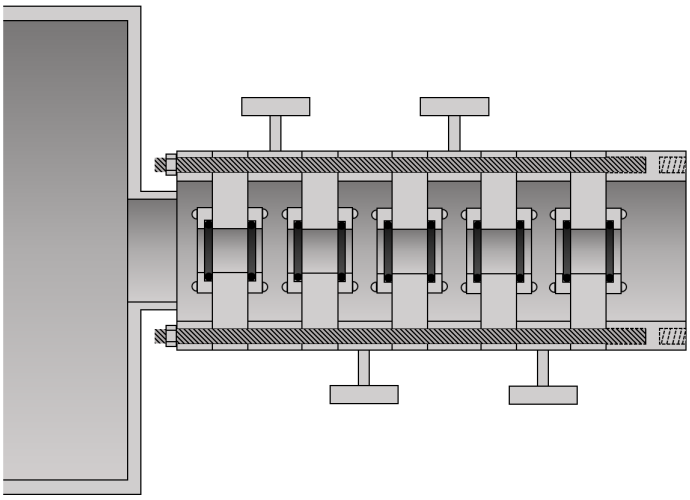

Figure 3.6: A more detailed depiction of the differentially pumped system design. All flange chambers and custom O-ring flanges are connected with 6 mm diameter threaded rods which are screwed into an end flange and tightened with nuts. Threaded holes on the other side of the end flange will allow the attachment of an add-on described in Section 3.2.5.

from an inert atmosphere in a glove box to the reaction chamber is therefore required.

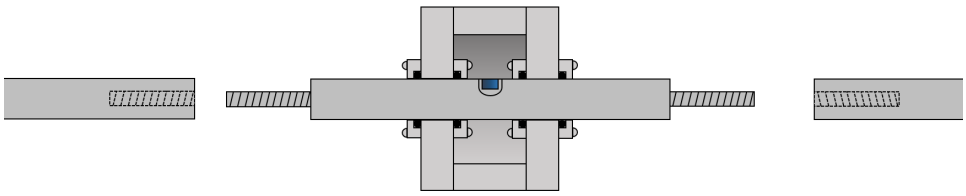

Figure 3.7: An add-on to enable air-free transfer of a sample from an inert atmosphere to the reaction chamber. The stainless-steel rod has been cut into three sections and that containing the sample recess can be placed into a flange chamber, forming seals with the custom O-ring flanges attached to either side.

A design which aims to provide this means, compatible with the system described, is shown in Figure 3.7. A 40 mm wide flange has two custom O-ring flanges connected to either side. The stainless-steel transfer rod has now been cut into three sections which can be reattached simply by screwing the parts together. 8 mm diameter threads of 35 mm in length ensure that the rod is sturdy upon reattachment. The middle section is

150 mm long with the sample recess in the centre, and this part is placed through the two O-ring flanges and into the flange chamber once the sample is mounted upon it inside the glove box. The left section of the rod, 240 mm in length, can remain inside the differential pumping scheme such that all seals are maintained. An inert atmosphere of gas, which in the case of this study is nitrogen, is sealed inside the add-on chamber. The add-on can then be removed from the glove box and the rod reattached to the other section in the main system. The add-on can be connected to the end flange of the system via 6 mm screws into the threaded holes: both the screw heads which attach the add-on together being flat to the edge of the left O-ring flange and the extra holes cut all the way through enable this connection. The final section of the rod is reattached before the rod is moved such that the sample is inside reaction chamber having had no contact with air. The reattachment of the 'air-free add-on' to the main system is depicted in Figure 3.8.

3.2.5.2 Test Results

The ability of the design to keep air out was tested using an oxygen indicator known as Ageless Eye. Samples of Ageless Eye were generously provided by Mitsubishi Gas Chemical Company [166]. The solid indicator is pink in the absence of oxygen (0.1% or less). It then begins to turn blue in increasing oxygen concentrations, taking 5 minutes to turn completely blue in a 0.5% oxygen concentration. Once blue, the indicator then takes 2 to 3 hours in the absence of oxygen to return to pink.

In a glove box containing an inert nitrogen atmosphere, one Ageless Eye pellet was placed inside the chamber and the detached rod section was pushed through to form seals at both O-ring flanges. The add-on was

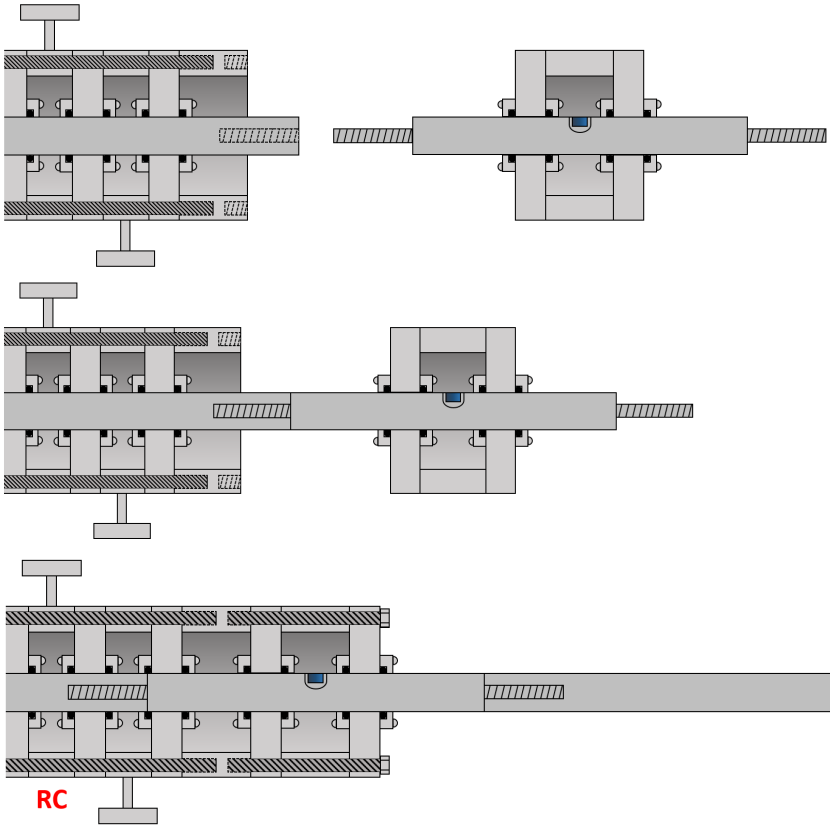

Figure 3.8: The process (from top to bottom) of attachment of the add-on to the main system. Once the sample is in the position seen in the bottom diagram, it can be moved horizontally into the reaction chamber (RC) such that it has not been in contact with air throughout the process.

then removed from the glove box and left in the open atmosphere for half an hour. It was turned several times to simulate attachment to the main system, before being returned to the glove box where the colour of the indicator was checked. The indicator had remained pink, showing that the part was successful in keeping air from leaking in. The process was repeated with the add-on left out in the open for greater lengths of time, the colour of the indicator recorded in each case.

As is seen in Table 3.2, the oxygen concentration inside the add-on rose above 0.1% after around 90 minutes of open atmosphere exposure. The test at 60 minutes was repeated several times, and in each case the indicator remained pink. It can therefore be said with some certainty that the add-

Table 3.2: Colours of the Ageless Eye indicator after the add-on was left in the open atmosphere for varying lengths of time. The indicator is pink in the absence of oxygen, and blue in its presence.

Time left in open (mins)	Colour
30	Pink
60	Pink
90	Pink/Blue
120	Blue
180	Blue

on is able to keep oxygen levels below a maximum of 0.5% concentration for up to 60 minutes; this is far longer than the expected time required to transfer the sample from the glove box to the system. The design was therefore proven successful and should enable the analysis of air-sensitive samples with this setup in the future.

3.3 Conclusions

The process for the design of a novel sample transfer has been described. The first prototype introduced a stainless-steel transfer rod pushed through custom O-ring flanges, which enabled a pressure differential of 3 orders of magnitude to be achieved between neighbouring chambers. The second prototype introduced more pumping stages into the system and a reaction chamber in the form of small flange chambers. With the pressure kept below the acceptable level for XPS analysis in the 'dummy' analysis chamber during rod movement between key sample positions, the system could be transferred to a real analysis chamber for the final design. Conclusions are made about the suitability of the final design in the next chapter, since they are based on results of the tests performed with a titanium dioxide crystal in a 'proof of concept' experiment.

Chapter 4

Device for Sample Transfer Between Reaction and Analysis Conditions - Proof of Concept

Contents

4.1 Introduction

The preceding Chapter described a device which was designed to enable rapid XPS analysis of a sample following a reaction of interest. The design of the system was illustrated and explained in detail, and the study described in this Chapter looks to test its ability to meet these goals, providing a 'proof of concept' for the device.

Titanium dioxide (TiO_2) is a widely studied material; a versatile semiconductor with unique properties, it has garnered considerable attention for its potential applications in nanoelectronics [167], photocatalysis [168, 169], and optoelectronics [170]. Moreover, its ability to serve as a photovoltaic material holds immense promise for future solar energy conversion technologies, including, as described in this thesis, solar water splitting for hydrogen production [107]. In this study, however, it is used purely for its behaviour under argon ion (Ar^+) sputtering and air exposure.

When a defect-free TiO_2 crystal is sputtered, its surface and sub-surface layers are depleted of oxygen until a steady-state level of reduction has been established [171, 172]. Titanium defects, consisting primarily of oxygen vacancies, are formed in these layers, and the localised defect electrons which remain lead to reduced states of titanium which can be seen with XPS. Upon exposure to air, the defects will begin to heal as the surface layers become oxidised once more [172].

Using the capacity of the previously described device (Chapter 3) for rapid transfer between reaction and analysis, the evolution of the titanium oxidation states is measured with XPS for the sample crystal as-received, after Ar^+ sputtering, and after subsequent exposure to air.

4.2 Methods

The single crystal rutile $TiO_2(110)$ sample was provided by Pi-Kem, and cut to 7×10 mm to fit within the rod recess. With the experimental set up described in Chapter 3 and shown in Figure 3.5 for an experiment that does not require the air-sensitive add-on, the TiO_2 crystal was mounted to the rod recess using carbon sticky tape in the open atmosphere. With the initial pressure in the analysis chamber at 7.4×10^{-9} mbar and that in the turbo-pumped chamber (denoted as D_1 on Figure 3.5) at 1.0×10^{-6} mbar, the sample was moved into the analysis position.

Wide scans and core level XPS for the Ti $2p$ regions were measured for the as-received sample using a laboratory-based Al Kα X-ray source (Omicron DAR 400) with a photon energy of 1486.6 eV, and a Scienta Omicron R3000 hemispherical analyser. Argon was leaked into the analysis chamber until a pressure of 5×10^{-7} mbar was achieved, and the sample was then sputtered with Ar^+ ions at a voltage of 5 kV for 30 minutes in an effort to deplete the surface and sub-surface layers of oxygen, leaving it defective. XPS measurements were repeated for the sputtered sample before it was removed from the analysis chamber and positioned in the reaction chamber, where it was exposed to the open atmosphere for 15 minutes. The transfer process took just 3 minutes and 30 seconds. The sample was returned to the analysis position after the 15 minutes had passed, with measurements taking place just 5 minutes later.

Shirley background subtractions were used to enable peaks to be fitted to the XPS data with pseudo-Voigt line shapes; the Gaussian-Lorentzian ratio of the peak shapes for all fitting was fixed for features arising from the same core-level, with the widths allowed to vary within realistic constraints.

Peak identification from binding energy values was based on data from the NIST XPS database [148]. In each case, the binding energies of the XPS spectra were calibrated to the Ti^{4+} peak at 458.7 eV, which has been previously determined [148]. For calculations of the surface compositions, XPS peak intensities were normalised through division by the appropriate photoionisation cross-sections, which have also been previously determined [139, 140].

4.3 Results and Discussion

Figure 4.1 shows the XPS spectra of the Ti $2p$ regions for the as-received sample, the sample after sputtering, and after the sputtered sample has been exposed to air. For the as-received sample, the spectrum shows a doublet attributed to the Ti^{4+} oxidation state; the Ti $2p_{3/2}$ peak lying at 458.7 eV and the Ti $2p_{1/2}$ peak at 464.4 eV. As dictated by the degeneracy of the electronic levels (Section 2.1.4.2), the area of the $2p_{1/2}$ peak is half that of the $2p_{3/2}$ peak. It is also slightly wider, likely due to the presence of a satellite peak involving symmetry flip valence excitations [147] (Section 2.1.4.2). The "shake-up" satellite peak at 471.9 eV is also associated with Ti^{4+}, arising as a result of emitted electrons transferring energy to, and thus exciting, other electrons (Section 2.1.4.2). The apparent sole presence of Ti^{4+} on the surface of the TiO_2 sample is to be expected, since the prolonged air exposure has provided sufficient oxygen to heal any surface defects.

After the sample was sputtered with argon ions for 30 minutes, the surface of the crystal appears to be more defective, as oxygen atoms are depleted from the surface and sub-surface layers. This is demonstrated by the fact

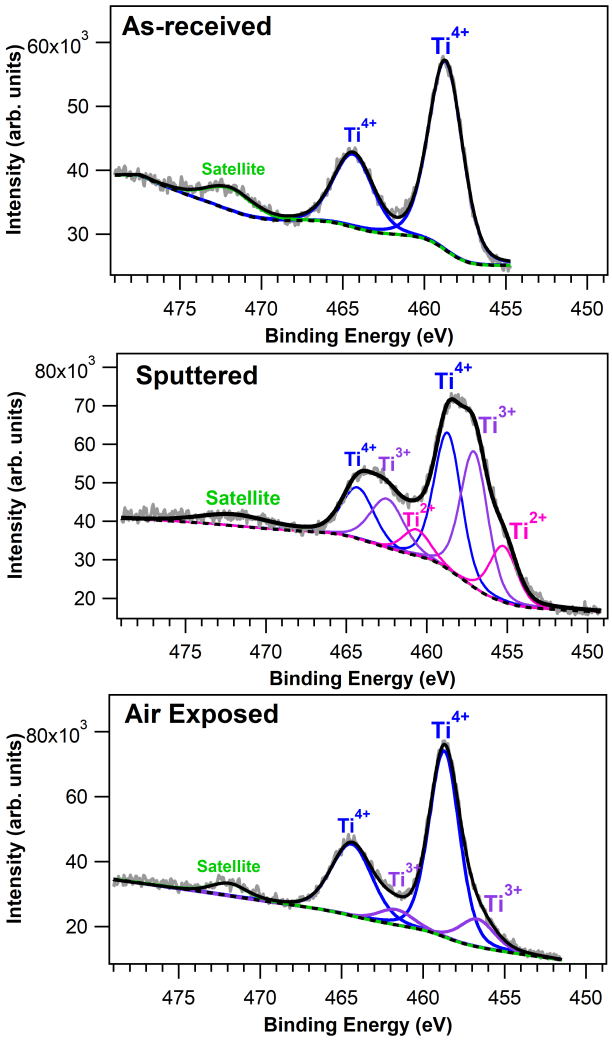

Figure 4.1: Core-level XPS spectra of the Ti 2*p* regions measured using a photon energy of 1486.6 eV for the as-received sample, after 30 minutes of argon sputtering, and after subsequent exposure to air for 15 minutes. Peaks have been fitted and the oxidation states labelled where appropriate.

that, not only has the spectrum again been fitted with spin doublets for the Ti^{4+} oxidation state, it has also been fitted with doublets for both the Ti^{2+} and Ti^{3+} states, with peaks at binding energy values of 455.2 and 460.7 eV, and 457.1 and 462.5 eV respectively for the Ti $2p_{3/2}$ and $2p_{1/2}$ components in each case. These are consistent with those in the literature [148, 172]. The peaks in the spin-orbit doublet attributed to Ti^{3+} in Ti_2O_3 are actually formed of complex multiplets, owing to final-state effects associated with its open-shell electron configuration, derived from the Ti 3*d* orbital, and the angular momentum coupling of the 2*p* hole with the open shell, intra-

atomic many-body effects, and core-hole screening [173]. These are left as unresolved doublets when fitted in this case, and throughout this thesis, since qualitative analysis is not required, but it should be noted that any fits where they are involved would have significant error associated with the relative amounts of the individual Ti fit components.

After withdrawal to the reaction chamber for air exposure, the sample was transferred back into the analysis position, and the measured spectrum is also shown in Figure 4.1. The surface defects appear to heal significantly, with the spectrum fitted predominantly with the Ti^{4+} doublet. A small amount of Ti^{3+} remains fitted to the lower binding energy side in this case, the peaks at 456.8 and 461.9 eV appearing to represent the Ti $2p_{3/2}$ and $2p_{1/2}$ components respectively. The oxygen in the air has enabled oxidation of the surface titanium defects.

Figure 4.2 shows a graph of the maximum pressures reached in the analysis chamber and in the turbo-pumped chamber (D_1) during each process. At all times the pressure in the analysis chamber remained low enough for acceptable XPS measurements to take place (below 1.0×10^{-5} mbar); the highest pressure was measured during sputtering, but importantly the highest during rod movement was recorded when the sample was transferred from the reaction chamber into the analysis chamber and was only 4.6×10^{-8} mbar. Measurements could therefore take place immediately once the sample was in position.

The time taken for this transfer was 5 minutes, while the reverse took 3 minutes and 30 seconds. These were conservative transfer times, where the rod movement was slow and controlled to keep the pressures as low as possible. If the rod is moved faster, more gas leaks between the seals of the pumping system, thus increasing the pressure in the analysis chamber;

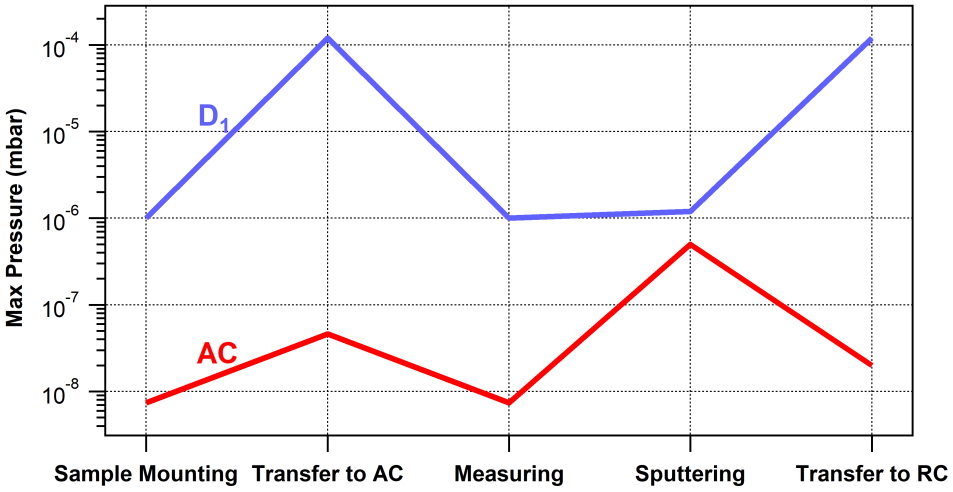

Figure 4.2: Maximum pressures reached in the analysis chamber (AC) and the turbo-pumped chamber (D_1) during processes carried out in the study. At all times the pressure in the analysis chamber remained lower than the maximum at which measurements are possible (1×10^{-5} mbar). The reaction chamber is denoted by the acronym RC.

a balance must be found between chamber pressure and transfer time. The transfer times compare well with those seen with other devices at atmospheric pressures in the reaction chamber in the literature (Table 1.1), while the transfer itself is a very simple mechanism. It was seen from the tests performed with the second prototype in the previous Chapter that a higher pressure than the 1 atmosphere of air in the reaction chamber could be used, but that was not necessary for this study.

4.4 Conclusions and Future Work

Defects formed on the surface of a TiO_2 crystal during Ar^+ sputtering were almost completely healed due to the reaction with oxygen in air, after exposure for just 15 minutes. Prolonged exposure may have allowed the defects to further heal, or instead annealing the sample at temperatures of 700 K and above [172]. Annealing causes oxygen anions in the crystal bulk,

and Ti^{3+} species in the surface and sub-surface layers to diffuse in opposite directions, allowing the defect-free structure to be restored [171]. Although not necessary for the purposes of this study, heating of the sample is not currently possible in the existing system setup. This capability may be introduced in the future. If a form of conductive heating was used, the rod would have to become more complex, allowing wires to pass through it to reach the sample recess. Instead, it may be more intuitive to have the heating take place in the reaction chamber, where a form of radiative heater could be mounted permanently.

This study has served as a proof of concept for the transfer device described in Chapter 3. The device employs a simple transfer mechanism which enables easy transfer from a reaction chamber to an analysis chamber, down a pressure gradient of 11 orders of magnitude. Taking just 5 minutes, and requiring no evacuation of the reaction chamber, the time for the transfer is comparable to similar systems in the literature, while also allowing for easy transfer in the opposite direction. The pressures in the analysis chamber were not as low as is ideally used for XPS analysis ($\leq 10^{-9}$ mbar), but this could potentially be achieved in the future by introducing another differentially pumped stage to the system. The increased distance for the sample to travel would however slightly increase the time for transfer.

For future studies, higher pressures of gas may be used in the reaction chamber. The current design has been used successfully with up to 4.5 bar of nitrogen, but even higher pressures would require adjustments to the system. The KF fitting on the reaction chamber itself would no longer be safe to use, so could be adjusted such that a National Pipe Thread (NPT) is welded in place. This would then allow connection to a gas line which could withstand hundreds of bar of gas pressure. The limits though would likely then arise due to the seals between the O-rings and the transfer rod, which

would need to be suitably tested at higher pressures to ensure safe use. Studies with different reactant gases may also be performed in the future; the system described was designed to be compatible with hydrogen, and so reactions of solid-state storage materials could be an obvious next step.

Chapter 5

Investigation of the Effects of Hydrogen Activation Conditions on the Surface of the High Entropy Alloy $(Ti_{0.65}Zr_{0.35})_{1.05}MnCr_{0.8}Fe_{0.2}$ using XPS Coupled with a Catalytic Reactor

Contents

5.1 Introduction

Many materials have been widely researched for their potential uses in hydrogen storage, with metal hydrides and their derivatives perhaps the most common. Intermetallic hydrides particularly have shown great promise in the field; properties of the chosen constituent metals are combined in attempts to meet capacity, kinetic and thermodynamic targets set for practical applications, such as vehicle propulsion.

A widely studied group of these hydrides are titanium (Ti) and iron (Fe)-based alloys. Cheap and with relatively high storage capacities [39], they suffer from a difficult activation process [174]. Temperatures and pressures required for the initial hydrogenation are far higher than the operating conditions that follow [84], meaning that the activation step alone places extreme constraints on practicalities such as vessel construction and safety management. To tackle this problem, other metals have been partially substituted in for both Ti and Fe. For example, zirconium (Zr) [91], manganese (Mn) [92] and chromium (Cr) [64] have each been used separately in an attempt to improve activation conditions.

In this study, all three of these transition metals are substituted in to produce an AB_2 type high entropy alloy (HEA) in the form of $(Ti_{0.65}Zr_{0.35})_{1.05}MnCr_{0.8}Fe_{0.2}$; also known as LCM-ERA 5, the A sites are occupied by Ti and Zr, while the B sites are occupied by Mn, Cr and Fe. HEAs are a relatively new family of materials with promising hydrogen storage characteristics and a high level of tunability [77]. They are defined to consist of five or more metals in near-equimolar ratios (none making up greater than 35 at.-% of the total alloy), forming a multicomponent solid solution as favoured by the high entropy of mixing. It is proposed that

the variation in the atomic radii of the constituent atoms leads to lattice strain which can be beneficial for hydride formation [76, 77].

Like most hydrogen storage alloys, when exposed to air, oxides will form on the surface of an HEA. The surface oxide layer and its chemical composition plays an important role in the activation of an intermetallic hydride, seen previously to act as a barrier which must be removed or reduced, be it only partially, for hydrogen to penetrate into the bulk of the material [84, 85, 90, 96, 101]. This is done with an activation process, usually consisting of high temperatures and a hydrogen atmosphere, leaving the metals present on the surface as sub-oxides, hydroxides, or in the metallic state [101, 175, 176]. A key feature of alloys, and in particular HEAs, is the propensity of their constituents for surface segregation [177]. This property plays a role in determining the composition of the surface, and thus that of the oxide layer as well as its interactions with hydrogen.

This study looks to investigate the activation step of LCM-ERA 5 by means of surface layer studies using XPS and NEXAFS. By providing a 'snapshot' of the surface elements before and after various treatments, any changes in the oxidation states of the elements and their chemical environments can be monitored. A catalytic reactor in the experimental setup [154] allows for the alloy to be exposed to extreme conditions before being rapidly transferred to an analysis chamber without exposure to atmosphere. The treatments of the sample include being heated under vacuum and in hydrogen, with the latter being repeated to investigate the behaviour of what should be an already activated sample. The aim of the study is to understand the effects of realistic activation conditions on the surface of this HEA, such that the knowledge may aid in the design of future HEAs with milder activation conditions, therefore accelerating adoption of the technology.

5.2 Methods

The alloy was synthesised by levitation induction melting of the constituent metals in a water-cooled copper crucible under an argon atmosphere of 1 bar, such that the stoichiometry of the alloy was $(Ti_{0.65}Zr_{0.35})_{1.05}MnCr_{0.8}Fe_{0.2}$. This process is described in more detail in a previous study of the alloy [178], with the authors confirming the stoichiometry and C14 Laves phase hexagonal structure using a combination of X-ray diffraction and scanning electron microscopy. The X-ray diffraction pattern is shown in Figure A.1 in Appendix A. Samples of the alloy used for surface analysis were lumps of approximately 1 cm x 1 cm x 0.5 cm in size, with at least one flat edge to enable easy mounting for laser heating. The samples were mounted onto stainless-steel foil on the sample plates and held in place by spot-welded stainless-steel strips. For heating, the laser passed through a hole in the back of sample plate and onto the foil, where the heat could spread evenly across the sample, helping to prevent sample damage from localised overheating. XPS and NEXAFS measurements of the samples were carried out on the HIPPIE soft X-ray beamline on the 3 GeV electron storage ring of the MAX-IV Synchrotron in Lund, Sweden. The beamline and endstation are described elsewhere [154], but the setup now also includes a chamber which hosts a catalytic reactor, where solid samples can be exposed to gases at pressures up to 1 bar and heated up to 900 ^{o}C with a laser heater. This new setup allows for a relatively short time between reaction and analysis, and the transfer between chambers to be done under ultra-high vacuum (UHV), preventing the reacted sample from coming into contact with anything during the process that may affect results. The alloy was split into two samples, A and B, such that the results of heating the as-received

state in vacuum and in hydrogen separately could be compared. XPS and NEXAFS measurements were first performed on sample A of the as-received alloy, and again after the same sample had been laser-heated under vacuum (ca. 10^{-9} mbar). The measurements were then repeated for sample B after it had been laser-heated in 1 bar hydrogen in the new reactor, and after this sample was laser-heated in hydrogen for a second time. For each treatment the sample was heated to 650 ^{o}C for 30 minutes. Wide scans and core level XPS for each constituent element were measured with an X-ray photon energy of 1000 eV, and in some cases 1600 eV to enable measurements of photoemission from deeper within the surface for those elements. Shirley, linear and polynomial background subtractions were used appropriately to enable peaks to be fitted to the data, while peak identification from binding energy values was based on data from the NIST XPS database [148]. For the as-received alloy and the alloy after heating in vacuum, the binding energies of the XPS spectra were calibrated to the Ti^{4+} peak at 458.70 eV, which has been previously determined [148]. After the hydrogen treatments, the binding energies of XPS the spectra were instead calibrated to the previously determined value for the adventitious carbon peak in the C 1s spectra at 284.4 eV [148]. This is due to the nature of the Ti 2p spectra after hydrogen treatments, where broad peaks meant that precise fitting of the individual components was not possible. The carbon peak in the C 1s spectrum for the alloy after heating in vacuum was also confirmed to lie at 284.4 eV, verifying the consistency of these calibrations in the case where both peaks were present. For calculations of the surface compositions, XPS peak intensities were normalised through division by the appropriate photoionisation cross-sections, which have been also previously determined [139, 140]. The error in the composition percentages was mainly due to the choice of background subtraction over each measured region;

systematic errors were introduced in normalised peak area calculations due to the variety of backgrounds that could potentially be subtracted in each case. To determine the size of the errors in the surface composition percentages, minimum and maximum values of the normalised areas under the peaks were calculated after different background subtractions, before these values were then compared to the opposite values of the remaining elements. For example, to calculate the maximum percentage of titanium in the as-received alloy, the maximum calculated area under the peaks of the Ti $2p$ spectrum was compared to the minimum values of the areas under the peaks of all of the remaining elements' core level spectra. Then for calculation of the minimum percentage of titanium, the minimum calculated area under the peaks of the Ti $2p$ spectrum was compared to the maximum values of the areas under the peaks of all of the remaining elements' core level spectra. This was repeated for each of the elements present.

For confirmation that the presence of sulphur seen in the XPS results after sample heating did originate from the alloy itself, and not the reactor, XPS measurements were repeated after another sample of the alloy was heated under vacuum in different apparatus. This was done using an electron beam heater behind the sample plate. The temperature was measured using a thermocouple located at the edge of the sample plate, with the sample heated to 650 ^{o}C for 30 minutes. These XPS measurements were performed using a lab-based monochromatic Al Kα source (photon energy = 1486.6 eV) and a Phoibos 150 NAP hemispherical analyser.

5.3 Results

Figure 5.1 shows the XPS wide scan measured to give overviews of the as-received alloy, and the alloy after each treatment. These help to show the obvious changes in amounts and oxidation states of each constituent element in the alloy surface layer. For example, they provide a visual representation of the decreasing amount of surface oxygen on the alloy, and thus the reduction of the surface during each treatment.

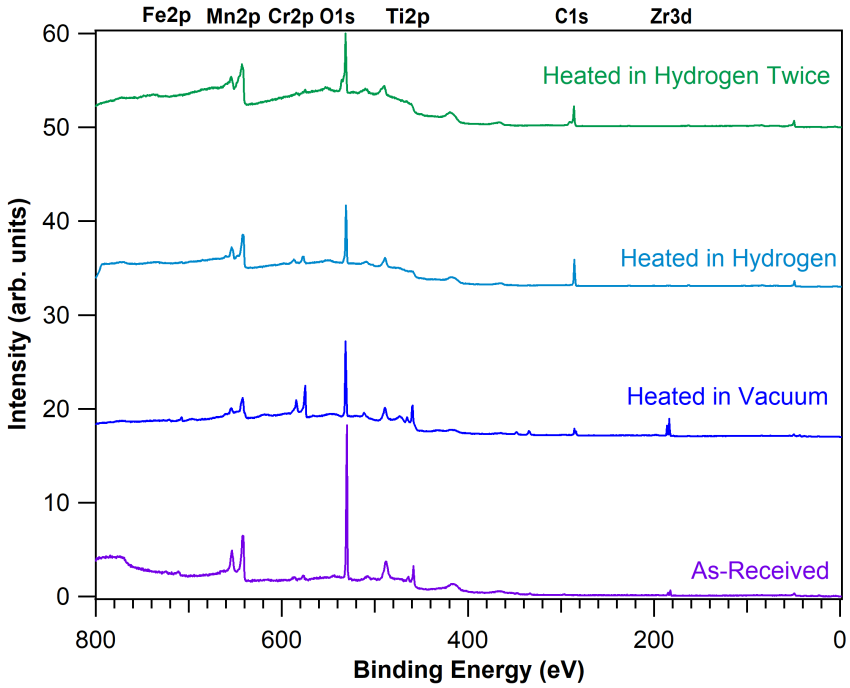

Figure 5.1: XPS wide scan including peaks for each of the highlighted binding energy regions of interest for the as-received alloy, and the alloy after it was heated at 650 ^{o}C for 30 minutes in vacuum, in 1 bar hydrogen and in 1 bar hydrogen for a second time.

This observation is confirmed by the surface composition values seen in Table 5.1; that of oxygen decreases from 72.1 at.-% to similar amounts, ranging from around 35 to 38 at.-%, after the three treatments. It can also be seen that carbon, although present in an almost negligible amount on the as-received alloy surface, formed around a quarter of the total surface composition after the heat treatments. This was similarly the case

with sulphur, with peaks appearing in the XPS spectra of the S $2p$ regions of the treated samples, although in much smaller quantities. It is thought that these impurities were present in the bulk of the as-received alloy, and were driven to the surface by the heat treatments. XPS measurements repeated after heating under vacuum in the different apparatus showed similar amounts of sulphur to be present in the surface layer, thus reaffirming these assumptions.

Table 5.1: Surface composition of the as-received alloy and after each treatment, calculated from relative peak intensities of XPS spectra

Element	**Surface Composition (at.-%)**			
	As-received	After Heating in Vacuum	After Heating in Hydrogen	After Heating in Hydrogen Twice
Ti	7.5 ± 0.4	10.3 ± 0.9	4.2 ± 0.7	5.3 ± 1.8
Zr	1.4 ± 0.1	3.1 ± 0.1	0.6 ± 0.1	0.1 ± 0.1
Mn	10.3 ± 0.9	16.3 ± 1.1	21.8 ± 0.9	25.2 ± 2.2
Cr	6.3 ± 0.2	9.4 ± 0.3	10.6 ± 0.7	2.6 ± 0.3
Fe	1.9 ± 0.5	1.4 ± 0.1	0.8 ± 0.5	0.4 ± 0.3
O	72.1 ± 1.3	36.9 ± 1.2	35.2 ± 1.4	37.7 ± 1.9
C	0.5 ± 0.1	22.0 ± 0.9	24.5 ± 1.2	26.8 ± 1.4
S	0.0	0.7 ± 0.1	2.3 ± 0.2	1.9 ± 0.2

5.3.1 As-received alloy

Figure 5.2 shows the XPS spectra of Ti $2p$, Zr $3d$, Mn $2p$, Cr $2p$ and Fe $2p$ signals for the as-received alloy. It can be seen that each constituent metal is mainly present in its fully oxidised state. For example, the majority of Ti is in the form of Ti^{4+} in TiO_2, as suggested by the Ti $2p_{3/2}$ peak at a binding energy of 458.7 eV, with its spin-orbit doublet Ti $2p_{1/2}$ at 464.2 eV. Unusually, another spin doublet pair at binding energies of 459.5 and 465.0 eV appears to suggest that a second phase of TiO_2 is also present in the oxide layer. The satellite at 471.9 eV is also indicative of TiO_2. Smaller contributions at 456.7 and 462.0 eV are then consistent with known values

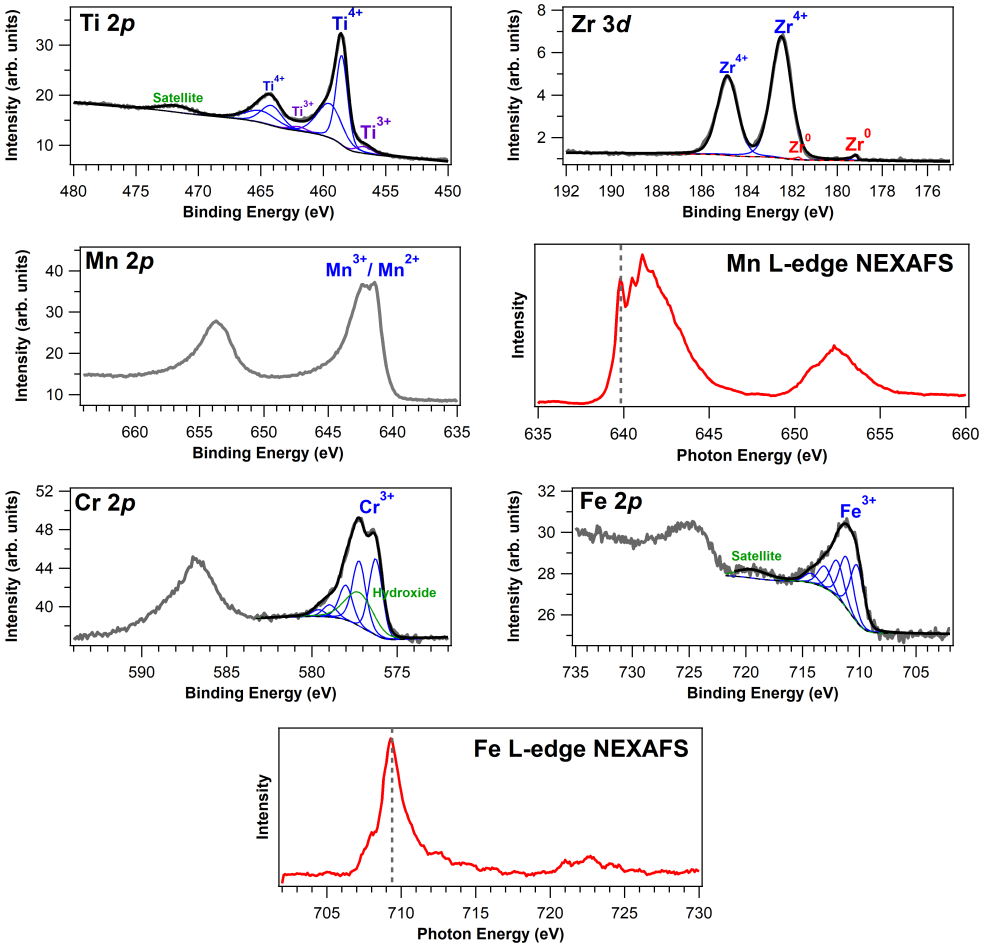

Figure 5.2: Core-level XPS spectra of the Ti 2*p*, Zr 3*d*, Mn 2*p*, Cr 2*p*, and Fe 2*p* regions measured using a photon energy of 1000 eV for the as-received alloy. Peaks have been fitted and the oxidation states labelled where appropriate. The Mn L-edge and Fe L-edge NEXAFS are also shown.

of the spin-orbit pair for a small amount of Ti^{3+} in Ti_2O_3 [148]. Peaks at binding energies of 182.5 and 184.9 eV in the Zr 3*d* spectrum likely represent the spin doublet of Zr^{4+} in ZrO_2 [148]. The smaller, slightly asymmetric peaks at 179.3 and 181.8 eV indicate the presence of some metallic Zr on the alloy surface.

In the Mn 2*p* region, the lack of a satellite peak at around 646.8 eV binding energy suggests that Mn is not in the 2+ oxidation state in the form of MnO. It is however difficult to then distinguish between Mn^{4+} in the form of MnO_2, or a mix of Mn^{2+} and Mn^{3+} in Mn_3O_4 from the XPS alone.

The NEXAFS, also shown, can instead be used; both the shape of the spectrum and in particular the peak at 639.8 eV photon energy suggest that Mn_3O_4 is present on the as-received alloy surface, when compared with similar spectra seen in the literature [179, 180]. In the Cr $2p$ spectrum, the broad peak at a binding energy of 577.2 eV suggests the presence of Cr^{3+} in $Cr(OH)_3$ and Cr_2O_3, the latter having multiplet splitting components consistent with values seen in a previous study in the literature [181]. All multiplet fitting performed in this study is consistent with the binding energy values used in this previous study. This forms the majority of Cr present on the alloy surface. The multiplet splitting components in the Fe $2p_{3/2}$ peak and the satellite at binding energy 719.4 eV imply that Fe on the as-received alloy surface is all in the form of Fe^{3+} in Fe_2O_3. This is further supported by the Fe L-edge NEXAFS spectrum (Figure 5.2), where the peak at a photon energy of 709.3 eV is consistent with values for Fe^{3+} in the literature [182].

5.3.2 After Heating Under Vacuum

Figure 5.3 depicts the XPS spectra of the alloy components after the sample was heated at 650 ^{o}C for 30 minutes under vacuum. As seen in Table 5.1, the amount of Ti on the alloy surface slightly increased from 7.5 at.-% to 10.3 at.-% after the treatment. Although with the associated error in the calculation of these values, the minimum measured increase is just 1.5 at.-%. The peaks seen at binding energies of 458.7 and 464.3 eV in the Ti $2p$ region are attributed to the spin-orbit pair of Ti^{4+} and suggest that Ti is still present predominantly in the form of TiO_2, reaffirmed by the satellite at 471.6 eV. There are now, however, significant contributions from both Ti^{2+} in TiO and Ti^{3+} in Ti_2O_3, as suggested by the pairs of peaks at 455.2

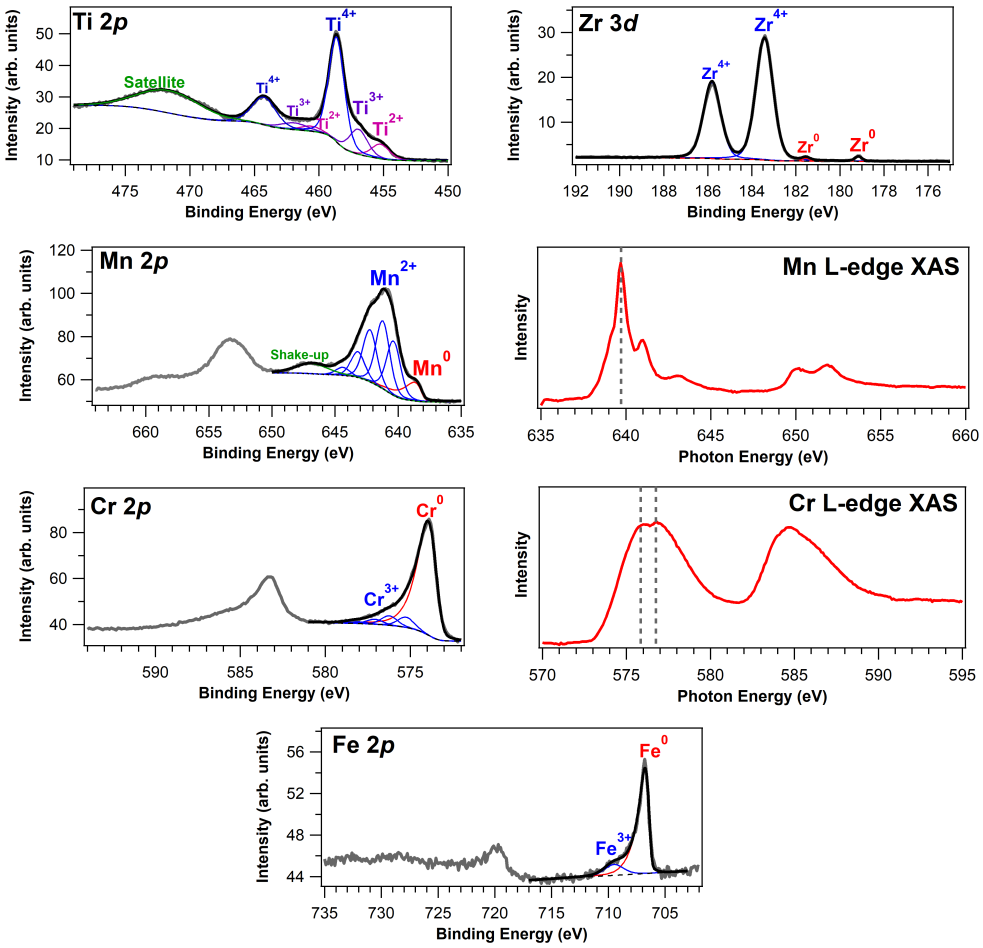

Figure 5.3: Core-level XPS spectra of the Ti 2*p*, Zr 3*d*, Mn 2*p*, Cr 2*p*, and Fe 2*p* regions measured using a photon energy of 1000 eV for the alloy after heating in vacuum for 30 minutes. Peaks have been fitted and the oxidation states labelled where appropriate. The Mn L-edge and Cr L-edge NEXAFS are also shown.

and 460.6 eV, and 456.9 and 461.9 eV respectively. The Ti present in the alloy surface has therefore been slightly reduced by the treatment. The amount of Zr on the alloy surface doubles after vacuum heating, while the XPS spectrum of the Zr 3*d* region remains very similar. Although the large Zr^{4+} peaks have shifted to slightly higher binding energies, the Zr is again present mainly in the form of ZrO_2, along with a small amount of metallic Zr. The amount of Mn has increased from 10.3 at.-% before to 16.3 at.-% after the treatment and has clearly been reduced from Mn^{3+} and Mn^{2+} in Mn_3O_4 to a majority of Mn^{2+} in MnO and a small amount of metallic Mn.

This is seen in the Mn 2p XPS spectrum by the multiplet splitting of the Mn $2p_{3/2}$ peak and the distinctive MnO shake-up satellite now present at a binding energy of 646.8 eV, as well as the Mn^0 peak at 638.9 eV. The Mn L-edge NEXAFS (Figure 5.3) also reaffirms the assignment of Mn^{2+} to the oxidised Mn, with its shape and main peak position comparable to those from studies in the literature [179, 180]. After heating in vacuum, the Cr in the alloy surface layer is mostly reduced from Cr^{3+} to metallic Cr, as indicated by the large peak at binding energy 574.0 eV in the Cr 2p XPS spectrum. The Cr L-edge NEXAFS (Figure 5.3) appears to confirm this, with the peaks at photon energies of 575.9 and 576.8 eV comparable to those of Cr^0 and Cr^{3+} respectively in other studies [183, 184]. There is a similar case for Fe, where the Fe^0 peak at 706.9 eV in the Fe 2p spectrum suggests that a majority of metallic Fe is now present. However, the total amount of Cr in the surface composition increases, while that of Fe decreases, after the treatment of the alloy.

5.3.3 After Heating in Hydrogen

Figure 5.4 shows the XPS spectra of the constituent metals after the as-received alloy was heated in 1 bar hydrogen for 30 minutes. It is clear that there are some peaks present in the Ti 2p region, but they are unresolvable. It therefore is not possible to infer which oxidation states of titanium are present. The signal appears instead to consist mainly of the inelastic background. The calculated amount of Ti in the surface composition has this time decreased from that in the as-received alloy to 4.2 at.-%. There are just two peaks present in the Zr 3d XPS spectrum, attributed to the spin-orbit split pair of Zr^{4+} at 182.5 and 184.9 eV binding energies. The surface amount of Zr has also decreased significantly after this treatment,

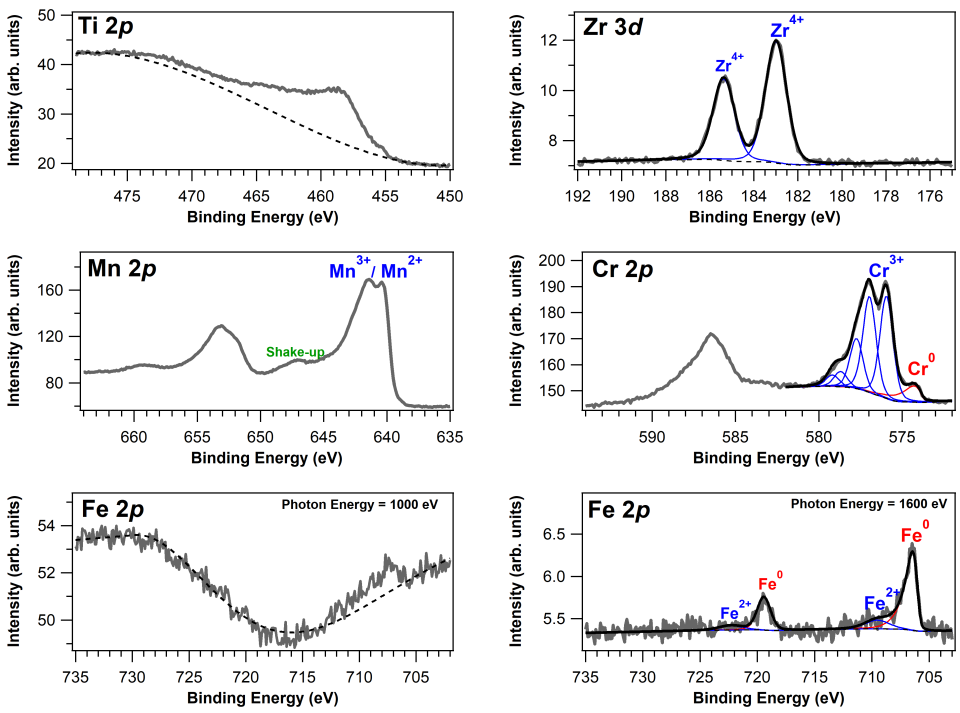

Figure 5.4: Core-level XPS spectra of the Ti 2*p*, Zr 3*d*, Mn 2*p*, Cr 2*p*, and Fe 2*p* regions measured using a photon energy of 1000 eV for the alloy after heating in 1 bar hydrogen for 30 minutes. The measurements of the Fe 2*p* region were also measured using a photon energy of 1600 eV, such that Fe deeper within the surface of the alloy could be probed. Peaks have been fitted and the oxidation states labelled where appropriate.

to just 0.6 at.-% of the of the total composition. The XPS spectrum of Mn 2*p* after heating in hydrogen shows a combination of the two previously seen spectra, indicating the presence of both Mn^{3+} and Mn^{2+} in Mn_3O_4, and Mn^{2+} in MnO. Due to the complex multiplet splitting of both Mn oxidation states, it was not possible to obtain a reasonable peak fit in this case. The contribution of Mn to the total surface composition after this treatment is now approximately double that of the as-received alloy. After heating in hydrogen, Cr appears present mainly in the form of Cr^{3+}, as is suggested by the multiplet splitting. The peak at a binding energy of 574.5 eV also indicates that a small amount of metallic Cr is present. The Fe 2*p* XPS spectrum is made complex by the strange background contribution. It is thought that this arises since the peaks sit upon the background of

those in the Mn 2p region, which are very intense in comparison, causing the steep slope at the lower binding energy side of the Fe 2p region. This is further complicated by the presence of what is likely a broad carbon Auger peak; with a known kinetic energy value of around 270 eV [148], carbon KVV Auger electrons in this case will present as a peak at around 730.0 eV on a binding energy spectrum with the use of 1000 eV X-ray photons. Nonetheless, a small peak can be identified at a binding energy of around 708.0 eV which appears to show the presence of FeO on the alloy surface. In this case, XPS of the Fe 2p region was also measured using a higher photon energy of 1600 eV to probe Fe present deeper within the surface of the treated alloy. In this spectrum, the peaks of the Fe 2p doublet at 706.6 and 719.4 eV indicate the presence of a significant amount of metallic Fe, while those at 709.5 and 722.3 eV suggest a smaller contribution of Fe^{2+} in the form of FeO.

5.3.4 After Heating in Hydrogen Twice

The sample was heated in 1 bar hydrogen to 650 ^{o}C for 30 minutes for a second time, and the XPS spectra of the metals in the surface layer of the alloy are shown in Figure 5.5. The XPS spectrum of the Ti 2p region can be easily compared to that for the sample after one treatment in hydrogen, again showing one broad and unresolvable peak. No peaks can be seen at all in the Zr 3d region, suggesting that a negligible amount of Zr is now present in the surface layer. The Mn 2p region has a very similar spectrum to that of the alloy after one hydrogen treatment, with the only contributions coming from Mn^{3+} and Mn^{2+} in Mn_3O_4, and Mn^{2+} in MnO. The NEXAFS, with its shape and primary peak position of 639.7 eV photon energy, suggests that it is a majority of MnO, based on comparisons to other studies [179, 180].

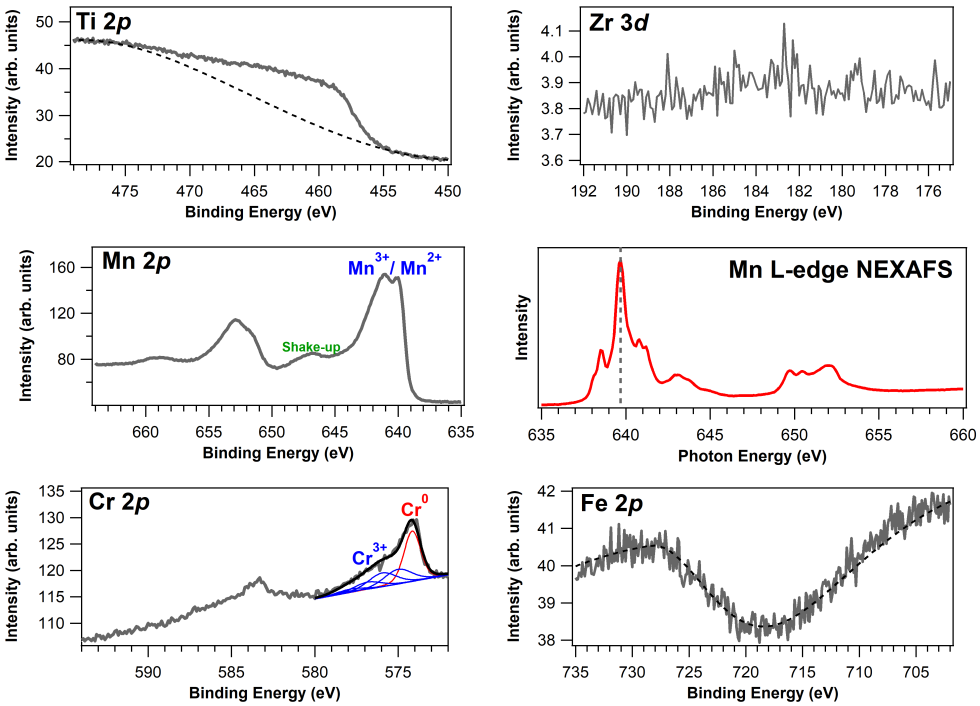

Figure 5.5: Core-level XPS spectra of the Ti 2*p*, Zr 3*d*, Mn 2*p*, Cr 2*p*, and Fe 2*p* regions measured using a photon energy of 1000 eV for the alloy after heating in 1 bar hydrogen for 30 minutes for a second time. Peaks have been fitted and the oxidation states labelled where appropriate. The Mn L-edge NEXAFS is also shown.

The amount of Mn on the alloy surface has again increased after the alloy was heated in hydrogen, and now makes up around a quarter of the total surface composition. There is just 2.6 at.-% of Cr now present on the alloy surface, a decrease when compared to the as-received alloy and after each of the other treatments. It consists of equal contributions from metallic Cr and Cr^{3+} in the Cr 2*p* XPS spectrum, as seen by the peak at 574.2 eV and the higher binding energy multiplet split peaks respectively. The Fe 2*p* spectrum is again similar to that in Figure 5.4, but in this case it is difficult to identify any peaks. There were also no peaks seen in the region after XPS was repeated with the higher photon energy. It can therefore be said that there are negligible amounts of Fe in the surface and sub-surface layers of the alloy after it has been heated twice in hydrogen. Until now, the physical appearance of the sample itself had been completely unchanged,

but after the second hydrogen treatment it appeared to have a smoother surface.

5.4 Discussion

The oxide layer seen on the surface of the as-received sample is the main reason that an activation process is required for the first hydrogenation event. Energy, usually in the form of a high temperature, must be provided to break the bonds between oxygen and the constituent metals, exposing now-reduced metallic sites to the hydrogen atmosphere for interaction. The metals in an alloy will react to activation conditions in different ways depending partly on their enthalpies of formation of oxides, which explains why Fe is reduced the most after the sample is heated in vacuum; FeO has the least negative enthalpy of formation of all the oxides that can be formed by the metals present in the alloy [65]. The oxide layer will also vary depending on the composition of the alloy surface. As seen in Table 5.2, the stoichiometry of the bulk of the as-received alloy, $(Ti_{0.65}Zr_{0.35})_{1.05}MnCr_{0.8}Fe_{0.2}$, is different to that of the surface layer, $Ti_{0.73}Zr_{0.14}MnCr_{0.61}Fe_{0.18}$, due to surface segregation; there is a larger fraction of both Ti and Mn in the surface, and smaller fractions of the remaining metals. The error range within which the relative stoichiometry of each element can be accurately stated is shown in Table A.1 in Appendix A.

This phenomenon is seen in alloys and in particular HEAs [177, 185], where the surface can become more enriched in some constituents than others. Segregation of Mn specifically has previously been seen both computationally [177] and experimentally [186, 187] during oxidation of an HEA. In our study, after heating in hydrogen, the amounts of Mn in the surface layer

Table 5.2: Alloy formula of the as-received alloy and after each treatment, calculated from relative peak intensities of XPS spectra for all except the as-received bulk alloy

Treatment	Alloy Formula
As-received (Bulk)	$(Ti_{0.65}Zr_{0.35})_{1.05}MnCr_{0.8}Fe_{0.2}$
As-received (Surface)	$Ti_{0.73}Zr_{0.14}MnCr_{0.61}Fe_{0.18}$
After Heating in Vacuum	$Ti_{0.63}Zr_{0.19}MnCr_{0.58}Fe_{0.09}$
After Heating in Hydrogen	$Ti_{0.19}Zr_{0.03}MnCr_{0.49}Fe_{0.04}$
After Heating in Hydrogen Twice	$Ti_{0.21}Zr_{0.004}MnCr_{0.10}Fe_{0.02}$

increased and remained oxidised in the Mn^{2+} and Mn^{3+} states. It can be suggested then that the Mn is playing an enabling role in the hydrogenation of the HEA. It appears to be sacrificially oxidising on the surface, such that Cr and Fe can remain in reduced metallic states to provide a pathway for the dissociation of the hydrogen molecules and diffusion of hydrogen atoms into the bulk. Mn has been seen to do this previously in a TiFe-based alloy [65], where it was also noted that Mn_3O_4 in particular has a large negative enthlalpy of formation, so is more likely to form than other oxides of the metals present. Ti may be playing a similar role to Mn, as it also appears oxidised after the alloy is heated in hydrogen. There is however a much smaller amount of Ti than Mn, so one would assume it is having less of an effect. The large decrease in measured amounts of both Ti and Zr after the hydrogen treatments may suggest that they are buried beneath an overlayer rich in Mn. This would also explain the nature of the Ti 2*p* signals, which became heavily influenced by the inelastic background after the alloy was heated in hydrogen. Metallic Fe seen deeper within the surface after the sample was heated in hydrogen may also be acting as a catalyst, as suggested in other cases involving the activation of TiFe-based alloys [188–190].

The greater reduction of the surface states after heating under vacuum

alone versus heating in hydrogen suggests that separating the heating and hydrogen exposure steps could provide a more successful means of activation, with more sites available for hydrogen dissociation. It is also likely, however, that the spectra after heating in hydrogen essentially show the combination of a two-step process, with the first step being that seen in the spectra for the sample heated under vacuum. Another potential reason for oxides remaining on the alloy surface after the hydrogen treatments is that residual oxygen or water is introduced into the catalytic reactor with the hydrogen. Although unlikely, this should be further investigated so as to prevent incorrect conclusions being drawn from the results.

The sample was heated in hydrogen for a second time to investigate the changes occurring on the surface of what is now an activated sample. Again the composition was further dominated by Mn and Ti, while Cr on the alloy surface also became more reduced after the second hydrogenation. Both results suggest that the second cycle acted to further enhance the effects of the first hydrogenation process.

Throughout the experiment, the physical appearance of the sample remained mostly unchanged. However, the broadening of the peaks, particularly in the Ti $2p$, Fe $2p$ and Zr $3d$ regions, and the marked change in stoichiometry away from the original AB_2 type alloy after the hydrogen treatments may suggest that the structural integrity of the sample itself has been slightly altered. This partial decrepitation is expected, as the hydrogen drives its way into the bulk of the alloy, cracking the metal particles as it does so [191].

5.5 Conclusions and Future Studies

By probing the surface of the HEA before and after it has been exposed to hydrogen activation conditions, the activation mechanism has been explored. Observed changes were so dramatic that it is not possible to determine the mechanism and order in which they occurred, but the key results can be seen clearly. For example, it is seen that Mn plays a key role in the activation, with its oxides occupying most of the surface layer after hydrogen treatment, leaving reduced states of Cr and Fe available as sites for hydrogen dissociation, the first stage of hydrogenation. Its inclusion in future HEAs designed for hydrogen storage should therefore be strongly considered.

Further studies could involve similar investigations at different conditions in the reactor, with surface measurements performed as a function of increasing temperature and hydrogen pressures. This may include in-situ ambient pressure (AP)-XPS and AP-XAS at mbar pressures to determine the points at which key chemical and compositional changes occur, as well as the time required for activation. It may also be interesting to explore the activation as a two-step process, first heating under UHV and then exposing the highly reduced sample to hydrogen. Comparisons of the amounts of hydrogen absorbed could then help to suggest the preferred activation method. With the effects of hydrogenation appearing to be enhanced by the second hydrogen treatment, it would be of great interest to repeat the measurements after an increased the number of hydrogen cycles. Results could be compared to those found for the same material after repeated cycles [178], where the storage properties appeared to be unchanged after a total of 70 cycles.

Similar studies could also be performed on different HEAs including those consisting of the same constituent metals, but with differing stoichiometries, as this is also expected to have an effect on activation properties. The relationships of other hydrogen storage properties and alloy stoichiometries were also investigated in the previously mentioned study including LCM-ERA 5 [178]. For further understanding of the activation mechanism, it may be of interest to determine where the oxygen goes when it is removed from the alloy surface. By performing mass spectrometry alongside the activation treatments, it should be possible to see in each case if the oxygen is leaving the alloy surface as a gas, or in fact being driven into the alloy bulk, something which may then be affecting the hydrogen storage capacity of the alloy.

Chapter 6

Surface Studies of Titanium Dioxide Nanoparticles on a Gold crystal surface

Contents

6.1 Introduction

Due to its abundant reserves, reactivity with light and water without corrosion, and relatively low cost [105, 108], titanium dioxide (TiO_2) has been widely investigated for its use as a photocatalyst in solar water splitting for clean hydrogen production ever since the first reported evidence in 1972 [107]. The chemical process is described in Section 1.3. The efficiency of the photocatalyst depends heavily on the competition between the rate of recombination of photoexcited charge carriers and that of their separation and migration. To increase this efficiency, noble metal cocatalysts are used to entrap electrons excited in the TiO_2, and subsequently separate them from their corresponding holes, such that they are able to carry out their respective roles as oxidisers and reducers [108, 109]. Gold has been used effectively in this manner in many cases [125–127], exploiting the Schottky barrier which forms at the junction of the metal and the semiconductor [109, 128, 192].

Owing to its large band gap (~ 3.2 eV [110]), ultra-violet (UV) radiation is required to excite electrons from the valence to the conduction band in TiO_2. UV, however, makes up just $\sim 4\%$ of solar radiation, while visible light makes up $\sim 46\%$ [109]; the efficiency of TiO_2 for solar water splitting would be vastly increased if it could also absorb in the visible spectrum. A common solution for this is to use dyes to sensitize the semiconductor, such that absorption of visible light is possible [115, 116], however, gold has also been used in the same way [110]; gold is irradiated by visible light, and electrons excited as a result transfer into the TiO_2.

It is therefore important to fully understand the interaction of gold with TiO_2, and in particular the charge transfer dynamics in both directions,

such that solar water splitting by TiO_2 can continue to improve. This interaction has been studied thoroughly, with gold and TiO_2 combined in a myriad of ways [126, 127, 193, 194].

In this study, TiO_2, in the form of nanoparticles with an average diameter of 21 nanometres (nm), is deposited in suspension with ethanol onto a gold crystal substrate. To the author's knowledge, this is the first time that this TiO_2/Au combination has been investigated. Two methods of deposition are used, drop casting and electrospray deposition, with the results compared. The interactions between the nanoparticles and the metal substrate are investigated with a combination of surface-sensitive analytical techniques including XPS, NEXAFS and RPES. With X-ray radiation incident upon the TiO_2/Au samples, electrons are excited to the LUMOs in the conduction band in a similar way as they would by solar radiation in a solar cell, although in this experiment they are excited from the core levels, instead of the HOMOs in the valence states. As described in Section 2.3, after this excitation, electrons will decay via one of several mechanisms shown in Figures 2.6 and 2.8. Each of these decays may appear as a distinct feature on the measured RPES maps, such that their occurrence can be identified. Since the "super-spectator" and "super-Auger" decay features will only present as a result of charge transfer from the Au to the TiO_2, they can therefore provide direct evidence of this. Charge transfer in the other direction may be instead identified by observing changes in the relative intensities of the "participator" decay features in a core-hole clock type analysis [161, 195–198].

The deposited nanoparticles are also sputtered with Ar^+ ions in an attempt to decrease their size. If successful, this would enable investigation into the potential effects of quantum confinement. The successful use of Ar^+ sputtering to decrease the size of nanoparticles has been seen previously

[199], where in that case it was gold nanoparticles deposited on a silicon substrate.

6.2 Methods

Experiments were performed on the FlexPES soft X-ray beamline on the 1.5 GeV electron storage ring of the MAX-IV synchrotron Laboratory in Lund, Sweden. The experimental set up of the system is described in detail elsewhere [155]. A rutile $TiO_2(110)$ single crystal was cleaned with 3 rounds of 1 kV Ar^+ ion sputtering for 20 minutes and annealing in UHV to 600 ^{o}C for 15 minutes, followed by 3 further rounds where the annealing was this time done in 1×10^{-7} mbar of oxygen. XPS was performed between rounds to ensure C 1s peaks were no longer visible and as few defects were present as possible in the Ti 2p spectrum. Once clean, XPS of the Ti 2p region, as well as NEXAFS over the Ti L-edge, and Ti RPES were all measured for later comparison to TiO_2 nanoparticles deposited on a gold surface. All core level XPS measurements were recorded with a fixed photon energy of 650 eV, with the Ti RPES measurements over a photon energy range of 454 to 470 eV and a binding energy range of –1 to 43 eV.

The TiO_2 nanoparticles were purchased from Sigma-Aldrich, who also determined the average diameter of the particles to be 21 nm using transmission electron microscopy (TEM).

An Au(111) crystal was also cleaned by Ar^+ ion sputtering and annealing in UHV with the same parameters as used for the TiO_2 crystal. A total of 5 rounds were required before O 1s and C 1s peaks were no longer observable by XPS. After measurements of the valence band XPS for the clean crystal, it was then removed from UHV, where an average diameter

of 21 nm nanoparticles of TiO_2 in suspension with ethanol was drop cast onto the clean Au crystal. 5 drops of the suspension were deposited in total, which had previously been sonicated to ensure an even distribution of the nanoparticles which otherwise collect at the bottom of the container. Back in the analysis chamber, with a base pressure in the low 10^{-10} mbar, XPS measurements of the sample were taken over the Ti $2p$, Au $4f$ and valence band binding energy regions, along with Ti L-edge NEXAFS and Ti RPES measurements. A density of states plot could be produced from the NEXAFS and the valence band XPS, such that both lay on the same binding energy scale. To achieve this for the Ti L-edge NEXAFS, the binding energy position of the Ti $2p_{3/2}$ core level is subtracted from the spectrum.

The sample was then sputtered with Ar^+ ions at 0.5 kV for a total of 1 hour and 25 minutes in an attempt to make TiO_2 particles smaller. XPS measurements were taken over the Ti $2p$ and Au $4f$ regions, along with Ti L-edge NEXAFS and Ti RPES. To then heal any defects in the nanoparticles, the sample was annealed in 1×10^{-6} mbar of oxygen in 30 minute blocks of increasing temperature. Beginning at room temperature, the final temperature of annealing was 360 ^{o}C. This was done such that the defects were healed at as low a temperature as possible, with Ti $2p$ XPS regions measured after each round until the spectra showed no further reduction in defects. The sample was annealed for a total of 4 hours before the same XPS, NEXAFS and RPES were again measured.

A different sample of Au(111) on a mica substrate was cleaned with Ar^+ ion sputtering and annealing in UHV. With the sample remaining under UHV, the sonicated suspension of TiO_2 21 nm nanoparticles in ethanol was then deposited onto the clean Au surface with electrospray deposition. The electrospray set up is shown in Figure 6.1. The UHV-4 system from Molec-

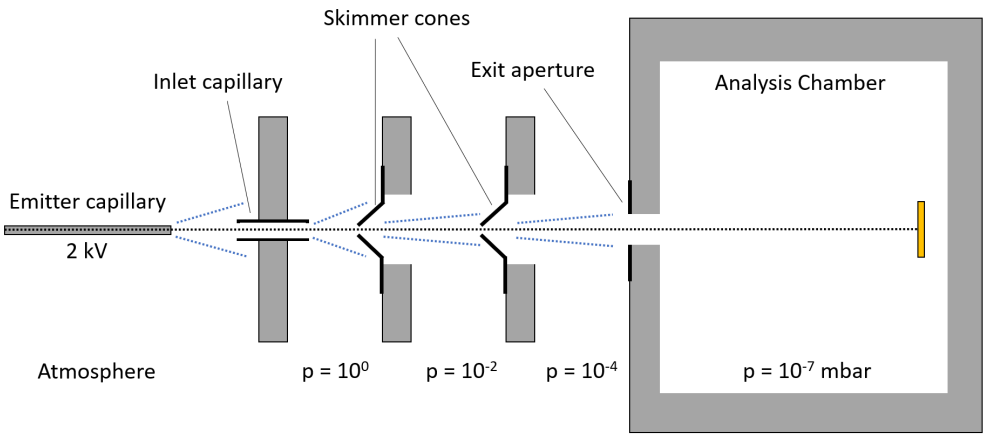

Figure 6.1: UHV-4 system from Molecularspray Ltd. for electrospray deposition. The diagram is adapted from [200].

ularspray Ltd. consists of a liquid feedthrough from a glass syringe and an electrical connection allowing the required high voltage to be applied to the suspension. The ionised suspension then passes through a stainless-steel 250 μm inlet capillary into a differential pumping scheme made up of 3 increasingly pumped chambers. Skimmer cones with aperture diameters of 0.4 and 0.6 mm force the ion beam along the plane of the sample while the ethanol is evaporated from the nanoparticles. The beam enters the analysis chamber through a 1 mm exit aperture such that the TiO_2 nanoparticles are deposited onto the gold surface at a pressure of 1×10^{-7} mbar. The liquid flow was controlled using a basic syringe pump (NE-300 from World Precision Instruments) and the high voltage using an iseg EHQ-104M. The position of the emitter feedthrough was controlled using a five axis manipulator (Thor Labs) and laser-aligned such that it was typically on axis to the inlet a few millimetres away. Typically a flow rate of $\sim$0.3 mL hour^{-1} and a voltage of $\sim$2 kV was used with a maximum current on the sample of 150 pA and that on the skimmer cones of 450 pA. The nanoparticles were deposited for a total of 3 hours. The suspension was regularly sonicated throughout the process to ensure an even distribution of particles. XPS, NEXAFS and RPES measurements were recorded, then again after the

sample had been sputtered at 1kV for 1 hour, and again after annealing to 460 ^{o}C in 1×10^{-6} mbar of oxygen for 1 hour. A density of states plot was again produced from the NEXAFS and the valence band XPS for the pristine nanoparticles only.

6.3 Results

6.3.1 Clean TiO_2 Crystal

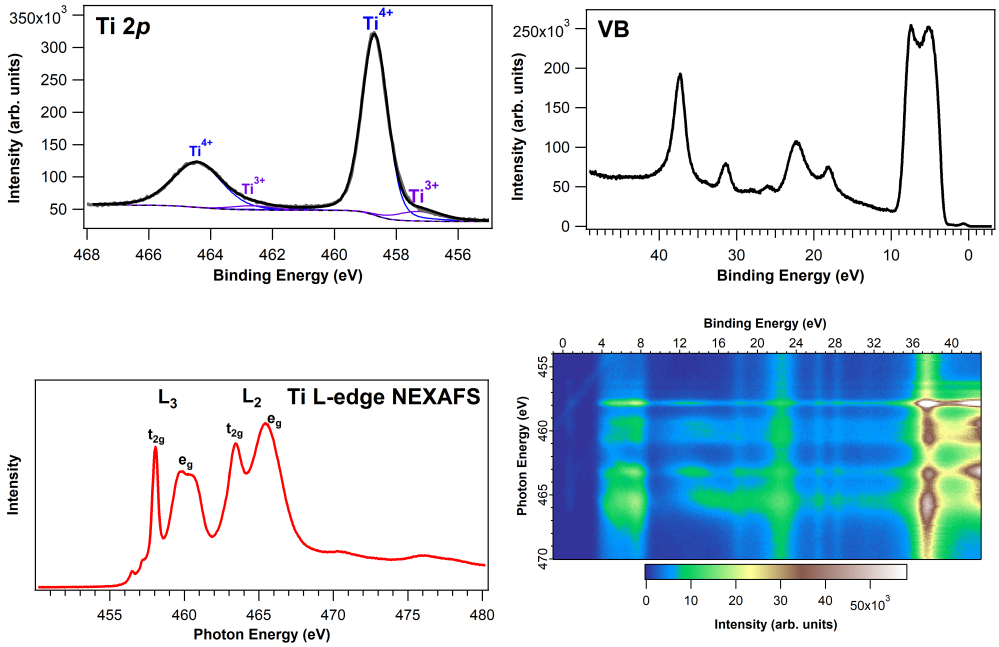

Figure 6.2: Core-level XPS spectra of the Ti 2p and valence band (VB) regions measured using photon energies of 650 and 110 eV respectively for the clean rutile Ti(110) single crystal. The intensity is given in arbitrary units. Peaks have been fitted and the oxidation states labelled where appropriate. The Ti L-edge NEXAFS is also shown, with the main peaks labelled, alongside the Ti RPES map of photon energy versus binding energy.

Surface measurements were performed on the clean rutile TiO_2 (110) single crystal to serve as a reference for comparison to those of the nanoparticles later deposited on gold. Figure 6.2 shows the XPS over both the Ti 2p and valence band binding energy regions, as well as the Ti L-edge NEXAFS and

2D Ti RPES map. It is noted that, for all spectra measured for this sample, the energy axes are calibrated to the Ti^{4+} peak of the Ti $2p$ XPS spectra lying at 458.7 eV in agreement with the literature [148]. The Gaussian-Lorentzian ratio of the peak shapes for all fitting was fixed for features arising from the same core-level, with the widths allowed to vary within realistic constraints. For all samples in this study, the Ti $2p$ XPS has been fitted after a combination of linear and Shirley background subtraction. In this case, the XPS shows that the vast majority of Ti in the crystal surface appears to be in the fully oxidised Ti^{4+} state. This is suggested by the Ti $2p_{3/2}$ peak at a binding energy of 458.7 eV, with its spin-orbit doublet Ti $2p_{1/2}$ at 464.4 eV. Despite several rounds of annealing in oxygen, there still appear to be small contributions from Ti^{3+} defects; the Ti $2p_{3/2}$ and $2p_{1/2}$ component peaks are at 457.3 and 462.6 eV respectively. The Ti L-edge NEXAFS was measured over a photon energy range of 450–480 eV, such that all peaks present correspond to excitations of the Ti $2p$ states into the empty Ti $3d$ states following X-ray absorption. The NEXAFS thus probes the unoccupied states of the sample, while XPS probes the occupied states. The two main peak groups arise from the spin-orbit splitting of the Ti $2p$ core level into the $2p_{1/2}$ (L_2-edge) and $2p_{3/2}$ (L_3-edge) levels. These levels are then further split into two sub-levels denoted by t_{2g} and e_g as per the different possible symmetries. The presence of the small peaks below the L_3-edge is related to particle-hole Coulomb coupling, which enables an otherwise spin-forbidden transition [201, 202]. The two large peaks at 7.4 and 5.3 eV on the valence band XPS are related to the O $2p$ derived states and are referred to as bonding and non-bonding orbitals respectively [203, 204]. The peak at 5.3 eV also represents the HOMO of the TiO_2 valence band, while that at 7.4 eV is labelled as the HOMO-1. Peaks at 22.3 and 37.3 eV likely represent the direct photoemission of electrons from O $2s$ and Ti $3p$ orbitals respectively, while that at 0.8 eV

arises as a result of the interstitial Ti^{3+} defect state in agreement with the literature [203, 204]. This is reinforced by the defect peak seen in the Ti 2p XPS region and can also be seen as a vertical band of enhanced intensity on the Ti RPES map, at the same binding energy of 0.8 eV. Horizontal bands of enhanced intensity seen on the RPES are associated with decay from the LUMO states of the TiO_2 conduction band. The largest of those lies at around 458 eV, representing the LUMO resonance, and has further intensity enhancements where it crosses with vertical bands at fixed binding energies associated with the HOMO and HOMO-1 at 5.3 and 7.4 eV respectively. These features provide evidence of participator decay involving the photoelectron from the excited LUMO state decaying to these occupied molecular orbitals within the timescale of the core-hole lifetime [161]. The enhanced intensities are observed here because the final state after the decay is identical to direct photoemission of the HOMO state involved. Similarly, further horizontal bands at photon energies of 459.8, 460.5, 463.4 and 465.4 eV represent the probability of decay from the LUMO+1, LUMO+2, LUMO+3 and LUMO+4 respectively, and more evidence of participator decay from these orbitals appears in the form of enhanced intensities where the HOMO bands meet them. The large vertical bands at around 23 and 37 eV are associated with direct photoemission from the O 2s and Ti 3p orbitals, as also seen on the valence band spectrum.

6.3.2 TiO_2 nanoparticles drop cast on Au(111)

XPS spectra for the Ti 2p and Au 4f regions after the ethanol suspension of TiO_2 nanoparticles was drop cast onto the gold surface are shown in Figure 6.3. The peaks seen in the Ti 2p XPS confirm the presence of TiO_2 after the deposition. As with the clean crystal, the peak fitting results suggest

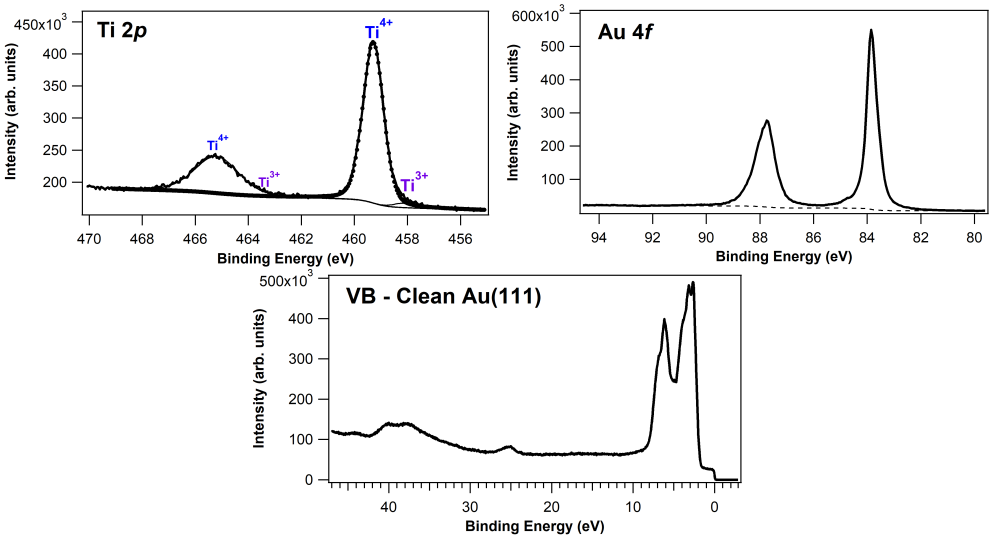

Figure 6.3: Ti $2p$ and Au $4f$ XPS for TiO_2 nanoparticles drop cast onto a gold crystal, measured using a photon energy of 650 eV. Peaks have been fitted for the Ti $2p$ region and the oxidation states labelled where appropriate. The valence band XPS of the clean Au(111) crystal is also shown; it was measured with a photon energy of 110 eV.

that the titanium is mostly fully oxidised, with a very small contribution from Ti^{3+} defects. Energies of all spectra for nanoparticles deposited onto gold were calibrated to the Fermi edge (0 eV) of gold on the valence band XPS. The position of the fitted Ti^{4+} peak for the $2p_{3/2}$ component, at 459.3 eV, lies at a slightly higher binding energy than expected. A suggestion of the reason for this is that the TiO_2 is in nanoparticle form; positive shifts of core levels in nanoparticles on a substrate compared to the bulk crystal of the same compound can be caused by both initial and final state effects [205, 206]. Initial state effects include those induced by nanoparticle-support interactions, and final state effects include an increase in positive charging after photoemission, where there is insufficient conduction from the substrate to replace the negative charge [206]. These can therefore be further investigated with the RPES measurements. The Au $4f$ spectrum, although not fitted, can be seen to suggest that the metallic Au is only present in one state in the sample. There are small shoulders seen on the higher binding energy side of each peak, but the positions and intensities

do not suggest anything physical, their presence may be due to experimental artefacts. After a Shirley background subtraction, the area under the data, along with the relevant ionisation cross-section [139, 140], was used to enable the quantification of relative amounts of TiO_2 and Au, when compared to those of the Ti $2p$ region. The ratio of Ti:Au was calculated as 1.6:1. It is therefore reasonable to suggest that a thin multilayer of TiO_2 nanoparticles had been successfully deposited onto the Au surface, although this could be investigated further with the use of Atomic Force Microscopy (AFM).

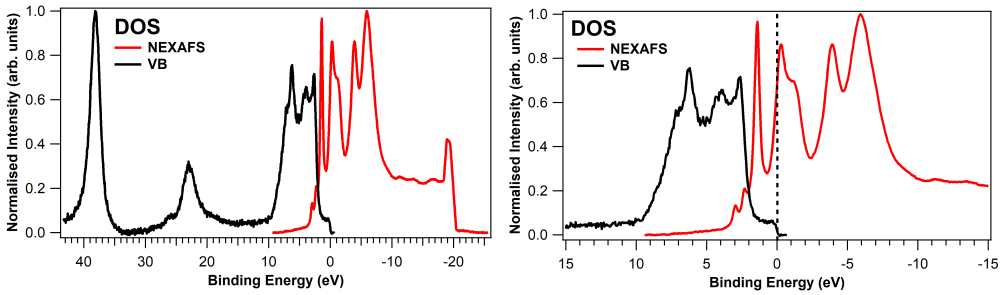

Figure 6.4: Density of States plot (left) for TiO_2 nanoparticles drop cast onto a gold crystal. The same plot is shown over a narrower binding energy range (right) for a clearer view around the Fermi edge. Ti L-edge NEXAFS were subtracted by the binding energy of the the Ti $2p_{3/2}$ peak in the XPS, and intensities normalised, such that it could be placed on the same binding energy scale as the valence band (VB) XPS, which was measured using a photon energy of 650 eV. The Fermi edge of the gold substrate (0 eV) has been marked with a dashed vertical line.

The density of states plot shown in Figure 6.4 was made by placing the valence band spectrum (occupied orbitals) and the NEXAFS (unoccupied orbitals) onto the same binding energy scale. This was done with the NEXAFS by subtracting from it the binding energy of the Ti $2p_{3/2}$ peak in the XPS and normalising the intensities of both spectra. By comparison with the valence band spectra of the clean TiO_2 and Au crystals (Figures 6.2 and 6.3 respectively), that of the multilayer shows features which represent contributions from both the TiO_2 nanoparticles and the underlying Au substrate, with four peaks close to the Fermi edge (0 eV) at around

2.6, 3.9, 6.2 and 7.3 eV binding energy. The position of the large peak in the NEXAFS, corresponding to the LUMO of the TiO_2 conduction band, is at 1.4 eV binding energy. This is therefore below the Fermi edge of the Au crystal substrate. This is unexpected, since, for a metal and semiconductor in intimate contact, a Schottky barrier is expected to form such that the Fermi level of the Au should lie within the band gap of the TiO_2. Nevertheless, the position of the LUMO in this case implies the possibility of charge transfer from the Au surface into the conduction band of the TiO_2 nanoparticles [159, 161]. However, due to the multilayer of TiO_2, the excited electron probed by RPES cannot transfer between the uncoupled nanoparticles and the Au surface, or to neighbouring nanoparticles (due to the excitonic effect of the core hole [161]). This does however mean that the participator intensities associated with the multilayer can later be used as a benchmark for the maximum intensities expected with no charge transfer, and so may help to determine whether charge transfer has taken place between a monolayer and a surface through what is known as the core-hole clock analysis [161, 197, 198]. This is performed later on in this study.

The Ti RPES map is shown in Figure 6.5, along with integrated vertical profiles over binding energy ranges of interest. The region over 0-2 eV binding energy covers the position of the 'defect peak' seen previously to account for Ti^{3+} states. As with the clean TiO_2 crystal, enhanced intensities are seen over both the L_2 and L_3 edges in this region of the RPES map. Although this peak is not seen in the valence band spectrum (Figure 6.3) in this case, its presence in the RPES agrees with that in the fitting of the Ti 2*p* XPS. There appears to be no resonant enhancement at the crossings of the LUMOs with the two vertical bands at binding energies of around 2.5 and 4.0 eV, implying no participator decay involving emis-

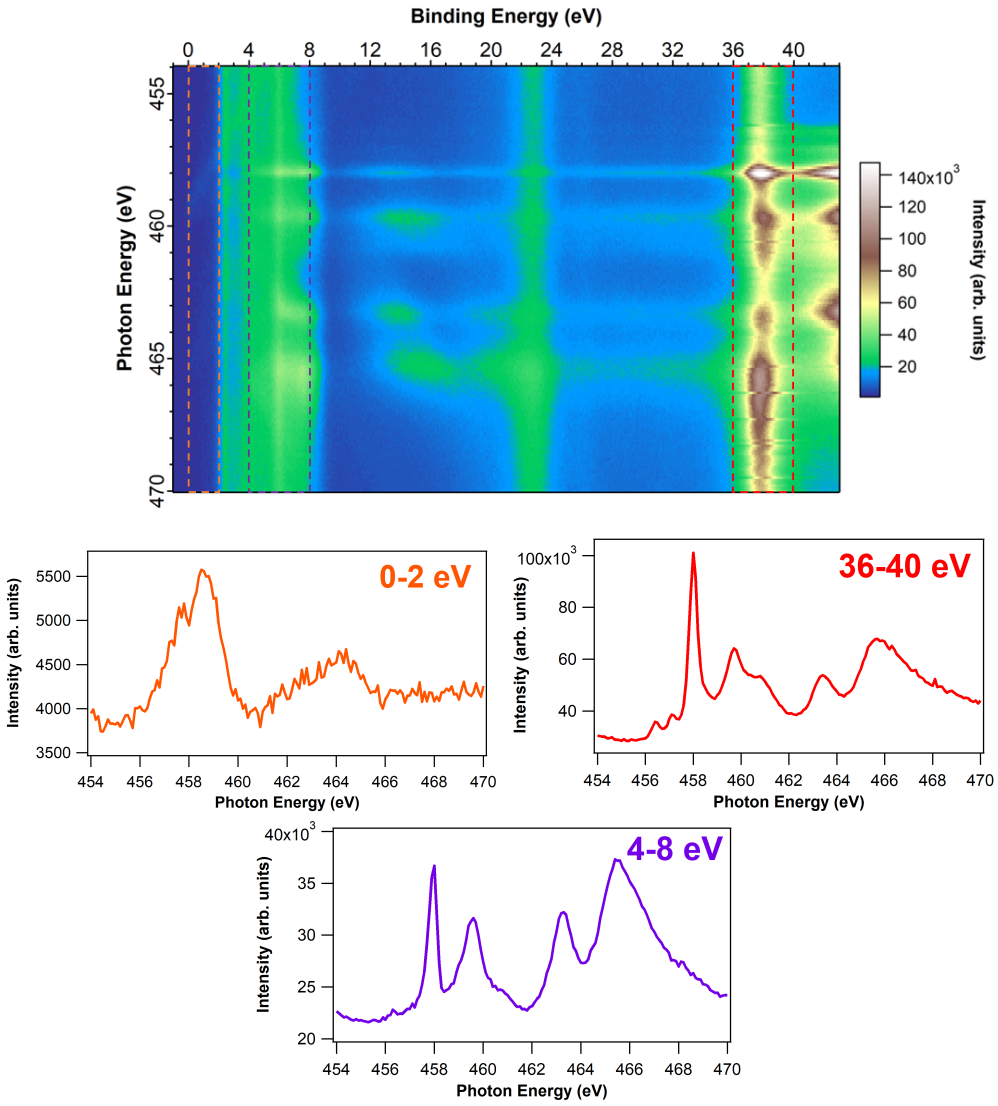

Figure 6.5: Ti RPES map (top) and integrated line profiles of the 'defect peak' (middle left), the top of the valence band (bottom) and the NEXAFS region (middle right) for TiO_2 nanoparticles drop cast on the Au crystal.

sion from these orbitals. The lowest binding energy participator features are instead seen along the bands at binding energies of around 6.1 and 7.6 eV. It is proposed that these bands therefore represent the energies of the HOMO and HOMO-1 of the TiO_2, while those with no participator enhancement are features of the gold substrate. The line profile over the 4-8 eV binding energy range covers the top of the valence band and includes this crossing of the HOMO and HOMO-1 with the LUMOs. Once again participator decay can be inferred from these enhanced intensities. When

compared to those of the NEXAFS, the peak intensities in this region may help to provide evidence of charge transfer, as part of the core-hole clock analysis [161, 196]. Finally, the 36-40 eV binding energy profile represents the Auger-yield NEXAFS.

6.3.3 TiO_2 nanoparticles after electrospray deposition on Au(111) on mica

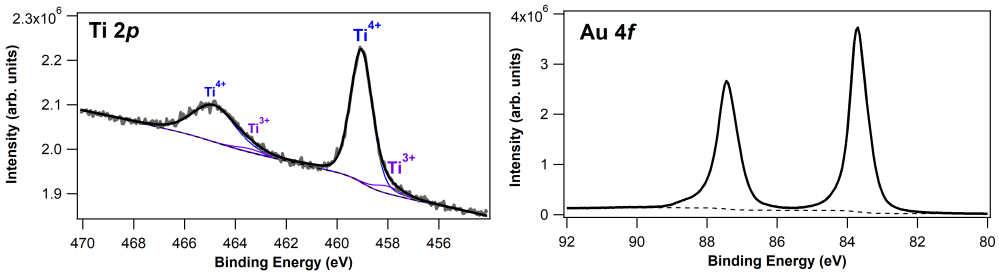

Figure 6.6: Ti $2p$ and Au $4f$ XPS for TiO_2 nanoparticles after electrospray deposition onto a gold crystal on mica, measured using a photon energy of 650 eV. Peaks have been fitted for the Ti $2p$ region and the oxidation states labelled where appropriate.

XPS spectra for the Ti $2p$ and Au $4f$ regions after the ethanol suspension of TiO_2 nanoparticles was electrosprayed onto the surface of the gold on mica sample are shown in Figure 6.6. The Ti $2p$ spectrum suggests that the TiO_2 particles deposited are again mainly in the fully oxidised state, with a very small amount in the reduced Ti^{3+} state. The binding energy position of the Ti^{4+} peak for the $p_{3/2}$ component, at 459.0 eV, again lies slightly higher than might be expected when compared to literature values [148], but 0.3 eV lower than the drop cast sample. It is suggested again that this shift is attributed to the nanoparticle form of the TiO_2. The Au $4f$ spectrum shows only one state, corresponding to metallic Au present in the sample surface, and a Shirley background subtraction again allowed the total intensity to be used for a quantifiable comparison of the amounts of TiO_2 and Au seen. After calculation, the ratio for Ti:Au was found to be

0.26:1. This suggests strongly that less than a monolayer of nanoparticles have been deposited onto the metal surface.

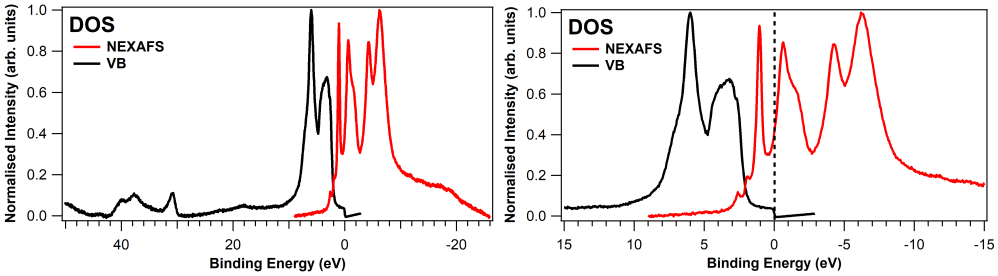

Figure 6.7: Density of States plot (left) for TiO_2 nanoparticles deposited by electrospray onto a gold crystal on mica. The same plot is shown over a narrower binding energy range (right) for a clearer view around the Fermi edge. Ti L-edge NEXAFS were subtracted by the binding energy of the the Ti $2p_{3/2}$ peak in the XPS, and intensities normalised, such that it could be placed on the same binding energy scale as the valence band (VB) XPS, which was measured using a photon energy of 650 eV. The Fermi edge of the gold substrate (0 eV) has been marked with a dashed vertical line.

A density of states plot (Figure 6.7) for the electrosprayed sample was made by placing the valence band XPS and Ti L-edge NEXAFS onto the same binding energy scale. The sharp peak of high intensity at 1.1 eV binding energy represents the LUMO of the nanoparticles and is 0.3 eV lower than that for the drop cast sample. This is consistent with the 0.3 eV shift in the Ti^{4+} peak in the XPS. Its position well below the Fermi edge also again suggests the possibility of charge transfer from the Au surface to this orbital. In this case, since the nanoparticles form less than a monolayer on the surface, charge transfer should be possible where it was not for the multilayer. On the valence band spectrum, it appears that there are again four peaks in the region close to the Fermi edge at similar binding energy values to those for the drop cast sample, although the two lower binding energy peaks are difficult to differentiate. This is likely because it is predominantly Au being probed, since the nanoparticles here form what is assumed to be less than a monolayer, so the valence band spectrum is dominated by that of the Au.

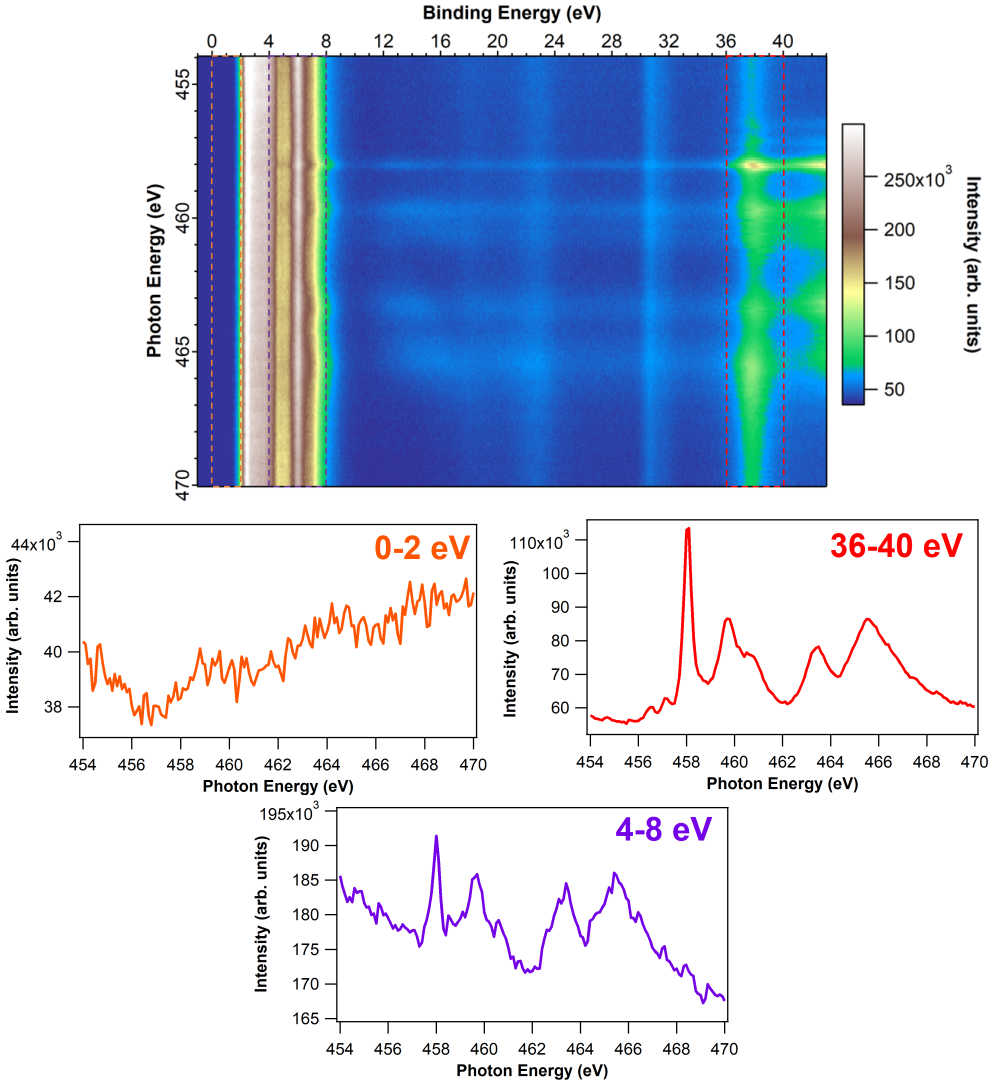

Figure 6.8: Ti RPES map (top) and integrated line profiles of the 'defect peak' (middle left), the top of the valence band (bottom) and the NEXAFS region (middle right) for TiO_2 nanoparticles after electrospray deposition on Au on mica.

The particularly high intensity of the valence band region when compared to the higher binding energy regions of the RPES map in Figure 6.8 makes it difficult to see participator features, but, as with the multilayer, they can be seen to be present on the integrated vertical profile over the 4-8 eV binding energy region shown in the bottom plot of the Figure, where peaks appear at the photon energies of the LUMOs. This is again attributed to resonant enhancement of the photoemission of the HOMO and HOMO-1 after participator decay involving electrons excited into the LUMOs within

the timescale of the core-hole lifetime. The profile over the 'defect peak' region (0-2 eV) again shows two small peaks, suggesting the presence of Ti^{3+} states, but in smaller amounts than seen for the other samples. The NEXAFS region (36-40 eV) is very similar to that of the drop cast nanoparticles.

Since the density of states plot implies that charge transfer from the Au surface into the LUMO of the TiO_2 is energetically possible, the RPES map may provide evidence if this has occurred. An electron transferred from the metal into the LUMO of the TiO_2 would be available to participate in core-hole decay; as explained in Section 2.3 earlier in the thesis, this can either be by "super-spectator" decay or "super-Auger" decay depending on whether the originally excited electron is localised on the timescale of the core-hole lifetime or not respectively. These processes would both appear on the RPES map as constant kinetic energy (diagonal) bands tracking back to the participator resonant enhancements in the HOMOs. This has been seen very clearly after charge transfer from a silver surface into the LUMO of an adsorbed monolayer of C_{60} molecules [161], but is not seen on the RPES map in Figure 6.8. We can therefore say that there is no evidence of charge transfer from the Au surface into the TiO_2 nanoparticles on the timescale of the core-hole lifetime in this case.

6.3.4 TiO_2 nanoparticles drop cast on Au(111): Sputtered

In an attempt to reduce the size of the TiO_2 nanoparticles, the Au crystal with nanoparticles deposited by drop casting were sputtered with Ar^+ ions. From the Ti 2*p* XPS (Figure 6.9), it appears that the sputtering made the nanoparticles far more defective, with a spin-orbit pair of peaks at binding

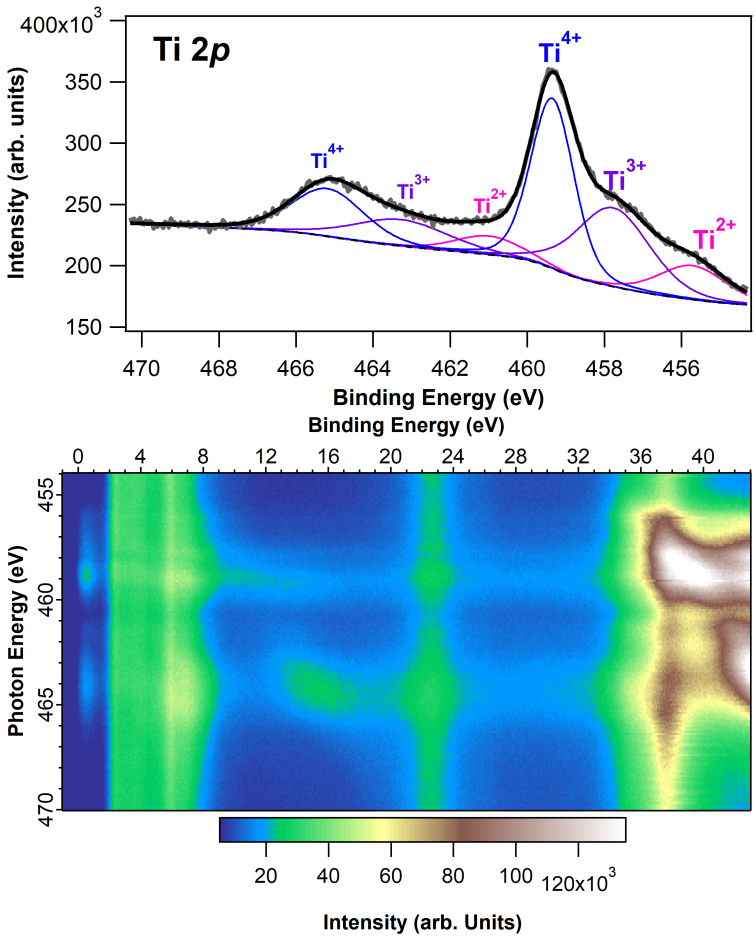

Figure 6.9: Ti 2*p* XPS and Ti RPES map for TiO_2 nanoparticles drop cast onto a gold crystal and sputtered with Ar^+ ions. The XPS was measured using a photon energy of 650 eV and peaks have been fitted with the oxidation states labelled.

energies of 455.4 and 460.7 eV suggesting a significant contribution from Ti^{2+}, while those at 457.4 and 462.9 eV suggest the same for Ti^{3+}. The disorder and mixing of resonant features in the Ti RPES map reinforce this suggestion, and there are large enhancements of intensity at around 0.8 eV binding energy, which represent the 'defect peak' as previously seen.

6.3.5 TiO_2 nanoparticles drop cast on Au(111): Sputtered and Annealed

After annealing the sample in oxygen up to a maximum temperature of 360 ^{o}C, XPS of the Ti 2p region shown in Figure 6.10 suggests that the majority of defects were healed by the process; the spectrum is very similar to that of the drop cast nanoparticles before sputtering (Figure 6.3).

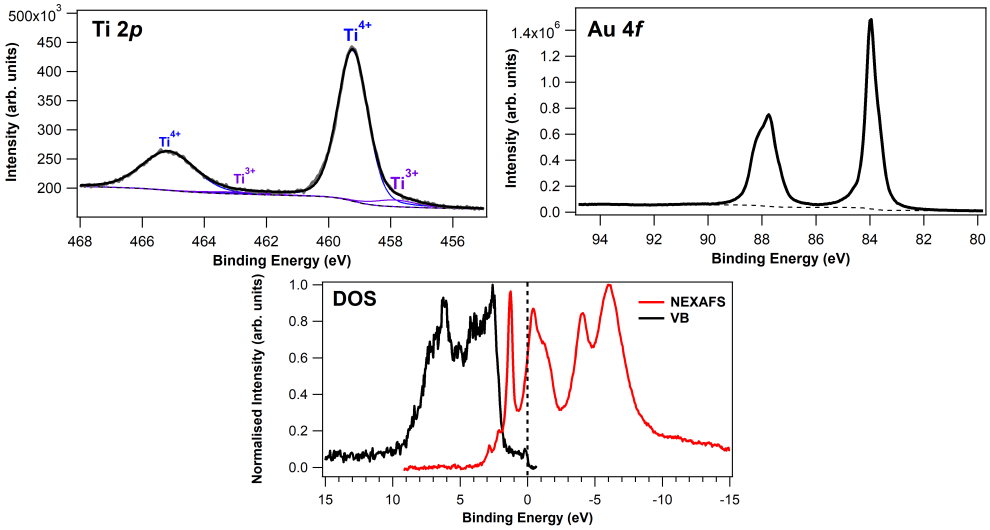

Figure 6.10: Ti 2p and Au 4f XPS for TiO_2 nanoparticles drop cast onto a gold crystal, sputtered, and then annealed. Spectra were measured using a photon energy of 650 eV. Peaks have been fitted for the Ti 2p region and the oxidation states labelled. The Density of States plot is also shown; Ti L-edge NEXAFS were subtracted by the binding energy of the the Ti $2p_{3/2}$ peak in the XPS, and intensities normalised, such that it could be placed on the same binding energy scale as the valence band (VB) XPS, which was measured using a photon energy of 650 eV. The Fermi edge of the gold substrate (0 eV) has been marked with a dashed vertical line.

The Au 4f spectrum again shows shoulders at the higher binding energy sides of the main peaks, and are again thought to be unphysical. The relative intensities of the Ti 2p and Au 4f regions, along with the relevant ionisation cross-sections, were again used to calculate a ratio of Ti:Au for the treated sample. A ratio of 0.64:1 shows a significant decrease from that of the pristine sample. Since the Ti was made far more defective after sputtering, it may be suggested that the sputtering has successfully made

the nanoparticles smaller, although the decreased ratio being caused by the complete removal of nanoparticles cannot be ruled out without further analysis with techniques such as TEM and AFM.

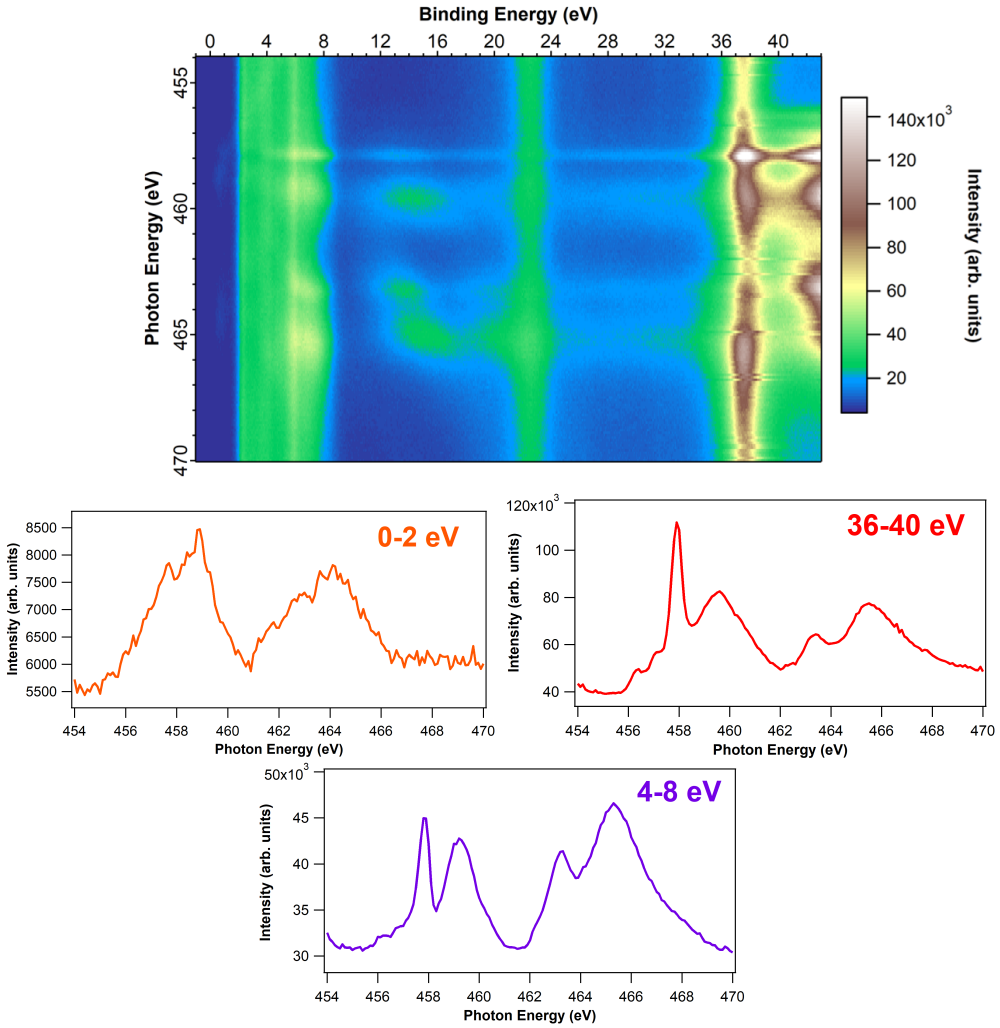

Figure 6.11: Ti RPES map (top) and integrated line profiles of the 'defect peak' (middle left), the top of the valence band (bottom) and the NEXAFS region (middle right) for TiO_2 nanoparticles drop cast on Au after Ar^+ ion sputtering and subsequent annealing in oxygen.

Despite the LUMO of the TiO_2 again lying below the Fermi edge of the Au (Figure 6.10), it is not possible to observe any charge transfer involving the multilayer of nanoparticles. It is for this reason that no constant kinetic energy bands of resonance are seen tracking to the participator features on the Ti RPES map in Figure 6.11. The map itself is very similar to that of the 'pristine' drop cast sample before it was sputtered and annealed. Again,

defect peaks in the 0-2 eV binding energy region are seen, and resonant enhancements at LUMO crossings of the vertical HOMO and HOMO-1 bands at around 6 and 7 eV suggest that excited electrons localised in the LUMO on the timescale of the core-hole lifetime are able to participate in the core-hole decay.

6.3.6 TiO_2 nanoparticles after electrospray deposition on Au(111) on mica: Sputtered

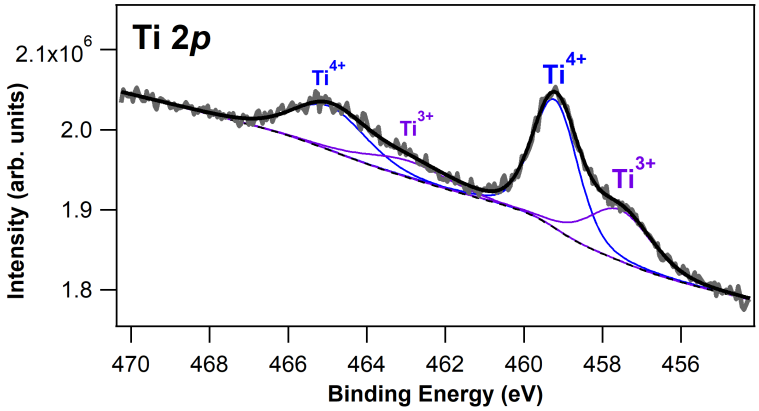

Figure 6.12: Ti 2*p* XPS for TiO_2 nanoparticles after electrospray deposition onto a gold surface and sputtered with Ar^+ ions. The XPS was measured using a photon energy of 650 eV and peaks have been fitted with the oxidation states labelled.

After the nanoparticles deposited onto the Au(111) on mica sample by electrospray were sputtered with Ar^+ ions, the Ti 2*p* XPS suggests more defects have been introduced, but this time without contribution from the Ti^{2+} state, as was seen after the drop cast sample was sputtered. Instead, the data are fitted with a large contribution from the spin-orbit doublet of Ti^{3+} at binding energies of 457.0 and 462.4 eV and again that of Ti^{4+} at 459.3 and 465.2 eV.

6.3.7 TiO_2 nanoparticles after electrospray deposition on Au(111) on mica: Sputtered and Annealed

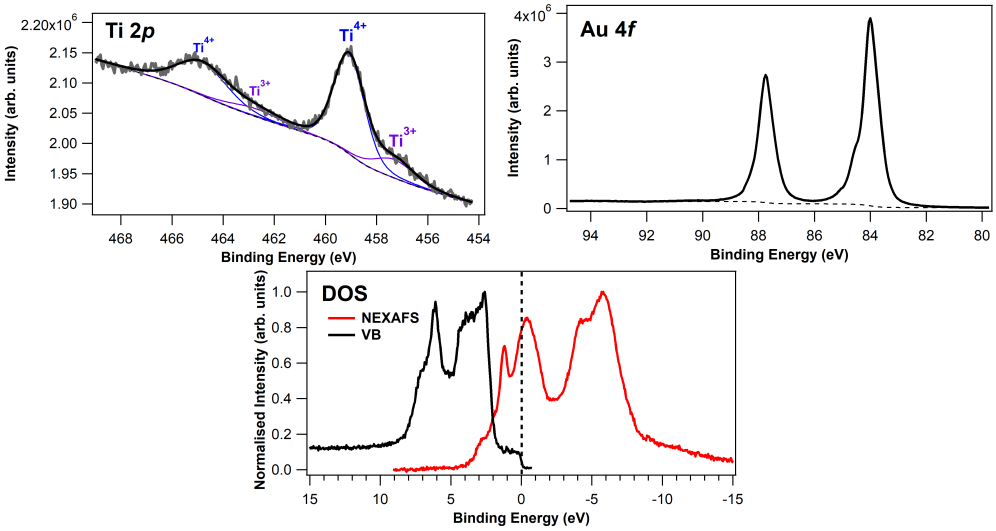

Figure 6.13: Ti $2p$ and Au $4f$ XPS for TiO_2 nanoparticles after electrospray deposition onto a gold surface, sputtered, and then annealed. Spectra were measured using a photon energy of 650 eV. Peaks have been fitted for the Ti $2p$ region and the oxidation states labelled. The Density of States plot is also shown; Ti L-edge NEXAFS were subtracted by the binding energy of the the Ti $2p_{3/2}$ peak in the XPS, and intensities normalised, such that it could be placed on the same binding energy scale as the valence band (VB) XPS, which was measured using a photon energy of 650 eV. The Fermi edge of the gold substrate (0 eV) has been marked with a dashed vertical line.

The Ti $2p$ XPS shown in Figure 6.13 suggests that annealing the electrosprayed nanoparticles to 460 ^{o}C in oxygen has somewhat healed the defects formed during Ar^+ ion sputtering. However, there is still a fairly significant contribution to the fit from peaks attributed to the Ti^{3+} state at binding energies of 457.3 and 462.7 eV. As with the previous samples, the Au $4f$ spectrum again shows shoulders on the main peaks, the reason for the presence of which remains unclear. The ratio of Ti:Au for this sample was calculated to be 0.22:1, again decreased from that of the sample before it was sputtered.

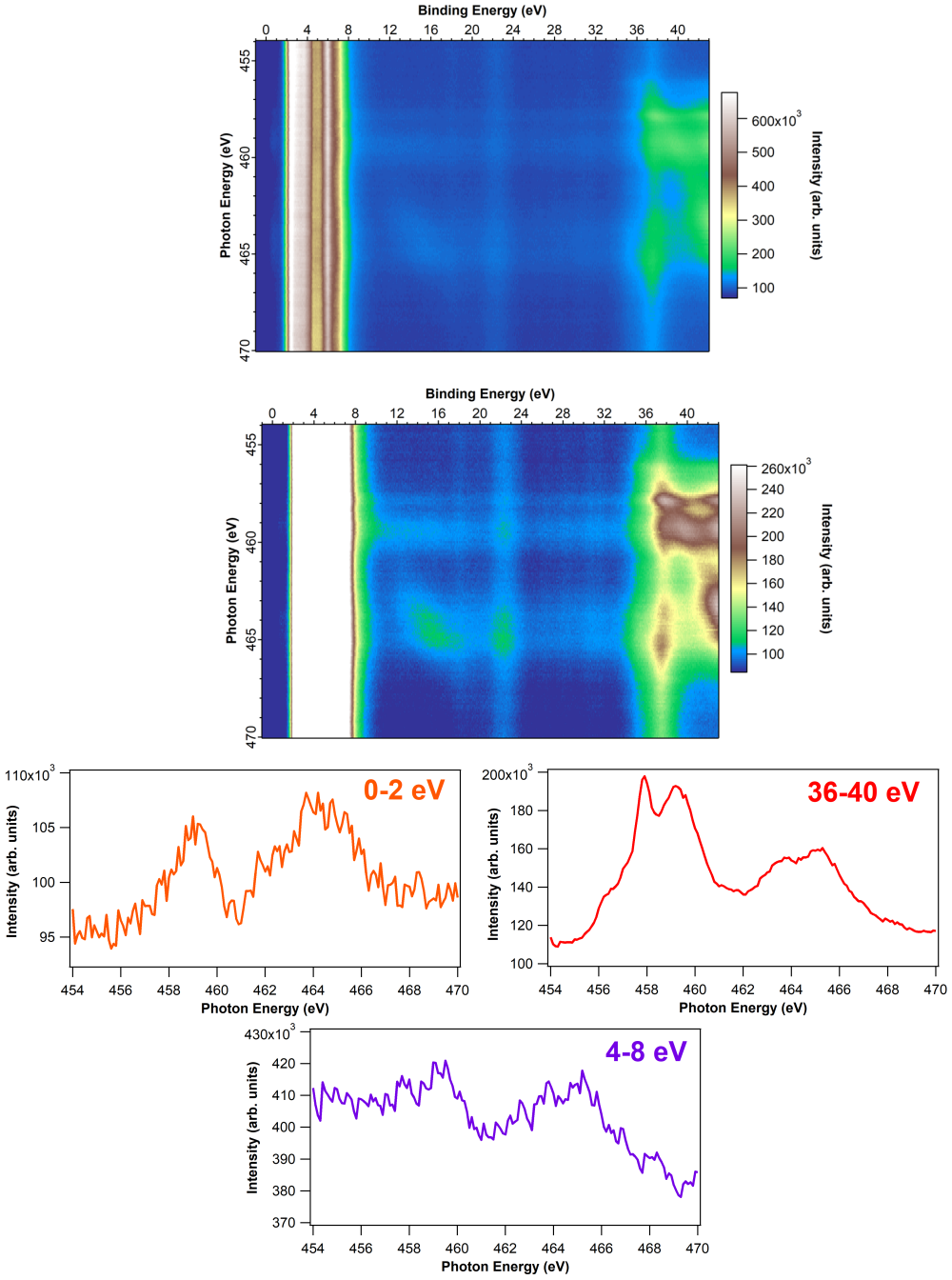

Figure 6.14: Two Ti RPES maps (top) are shown representing the same data but with different colour scales to allow features at all binding energies to be seen more easily. Integrated line profiles of the 'defect peak' (middle left), the top of the valence band (bottom) and the NEXAFS region (middle right) for TiO_2 nanoparticles after electrospray deposition on Au on mica after Ar^+ ion sputtering and subsequent annealing in oxygen are also shown.

Once again, from the density of states plot (Figure 6.13), it can be seen that the LUMO of the TiO_2 nanoparticles lies below the Fermi edge of the Au, suggesting the potential for charge transfer from the metal surface into

the nanoparticles. However, from the Ti RPES maps shown in Figure 6.14, there is again no evidence of this transfer in the form of constant kinetic energy bands of intensity tracking to the participator resonant enhancements. The two maps shown in Figure 6.14 represent the same data, but with different colour scales to allow features at all binding energies to be seen clearly. As with each of the Ti RPES seen in this study, there are peaks present in the 0-2 eV binding energy line profile which suggest defect states of Ti^{3+} present in the nanoparticles, in agreement with the Ti 2*p* XPS. Due to high intensity bands in the lower binding energy region of the map, it is difficult to see enhancements that may represent features of participator decay. The integrated line profile over the top of the valence band between 4-8 eV binding energy, also covering the energy of the HOMO and HOMO-1 bands, does however show peaks present at photon energies corresponding to the LUMOs. These peaks are less defined than those of the pristine sample of electrosprayed nanoparticles seen in Figure 6.8. The same can be said for the peaks in the NEXAFS region (36-40 eV binding energy). A potential explanation for this is that the spectra are showing a combination of the Ti^{4+} and Ti^{3+} states present, due to the larger contribution of defective Ti seen in the XPS. For this sample, the signal to noise ratio is also lower than any of the previously seen line profiles of the RPES; this is to be expected, since this is the smallest amount of TiO_2 probed in the study, but this also makes it more difficult to define the individual peaks at the photon energies corresponding to the LUMOs.

6.3.8 Charge transfer from the TiO_2 nanoparticles to the Au surface

No charge transfer has been seen from the Au surface to the LUMO of the TiO_2 on the timescale of the core-hole lifetime for any of the samples in this study. However, to see if it has occurred in the opposite direction, from the nanoparticles to the Au, a core-hole clock type analysis must be performed. This method makes use of the fact that the NEXAFS will represent the full intensity of the unoccupied levels, while the RPES of the HOMO from which the electron is excited may show reduced intensity as a result of charge transfer competing with the participator decay. This is only the case if the charge transfer can occur on the timescale of the core-hole lifetime. For the multilayer sample, where the nanoparticles were drop cast onto the Au surface, no charge transfer is possible in either direction. The participator intensities should therefore be maximised for this sample, such that any depletion in that of the monolayer of electrosprayed nanoparticles in comparison suggests that charge transfer has been observed. The line profiles integrated over the 4-8 eV binding energy region of the RPES maps, representing the participator enhancements for the drop cast and electrosprayed samples, are shown in Figure 6.15, along with the associated NEXAFS after background removal for both. In each case, the two plots are also normalised to the peak at the photon energy representing the LUMO (around 458 eV). Since the LUMO lies below the Fermi edge of the Au for each sample, charge transfer from the LUMO into the Au surface is forbidden, therefore by normalising the intensities at this photon energy, changes in the intensity of the participator features due to charge transfer out of the LUMO+1, LUMO+2, LUMO+3 and LUMO+4 states can be probed [196].

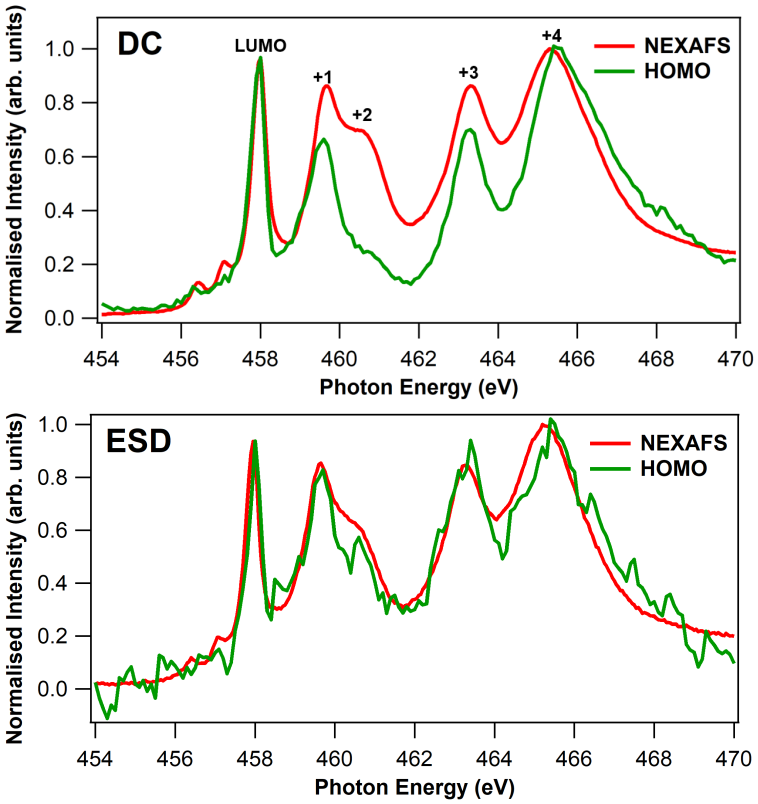

Figure 6.15: Line profiles integrated over the 4-8 eV binding energy region of the RPES maps (HOMO) plotted with NEXAFS for both the multilayer of drop cast (DC) nanoparticles and monolayer of electrosprayed (ESD) nanoparticles. The sets of data are normalised to the intensity of the LUMO peak at around 458 eV.

It can be seen clearly from Figure 6.15 that the participator intensity for the HOMO plot of the electrosprayed (ESD) monolayer sample is not depleted at photon energies corresponding to any of the LUMOs other than potentially the LUMO+4. In fact, unexpectedly, the HOMO plots of the drop cast (DC) sample are at lower intensities relative to the the NEXAFS for each of the other orbitals. The calculations of the intensity ratios for the monolayer $I^{mono}_{HOMO}/I^{mono}_{NEXAFS}$ and multilayer $I^{multi}_{HOMO}/I^{multi}_{NEXAFS}$ of nanoparticles were therefore only performed for the LUMO+4 orbital. By curve fitting in each case, areas underneath the peaks were found. The ratio for the electrosprayed monolayer was found to be $I^{mono}_{HOMO}/I^{mono}_{NEXAFS} = 0.98$, while that for the drop cast multilayer $I^{multi}_{HOMO}/I^{multi}_{NEXAFS} = 0.99$. The fact that the monolayer term is lower would indicate that charge transfer had

occurred from the LUMO+4 of the TiO_2 nanoparticles to the unoccupied states of the Au surface, but the difference in the ratios is far lower than the total error associated with the acquisition of the data and the calculation itself. It therefore cannot be said with any certainty that charge transfer has occurred on the timescale of the core-hole lifetime.

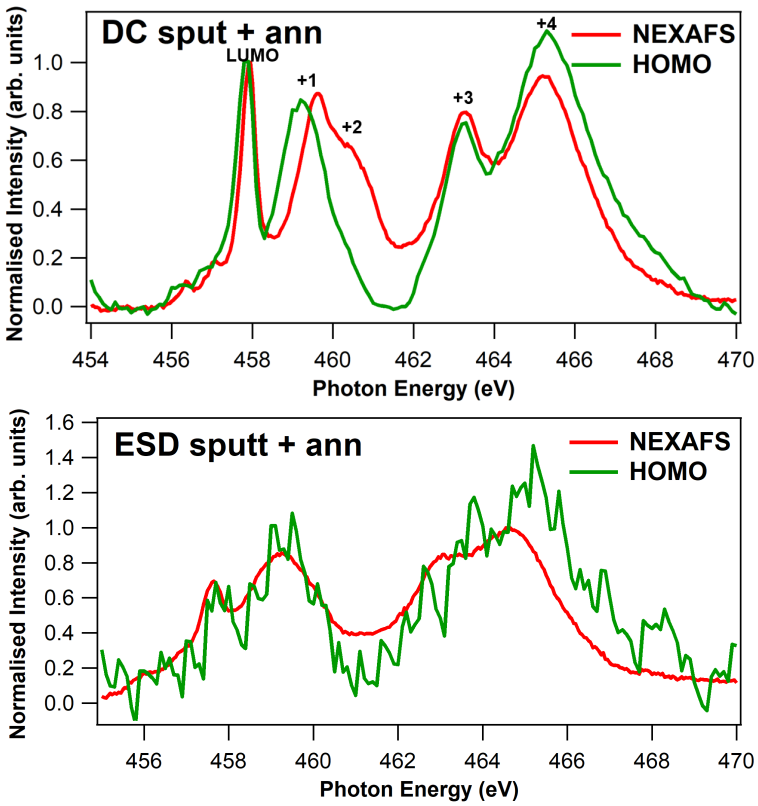

Figure 6.16: Line profiles integrated over the 4-8 eV binding energy region of the RPES maps (HOMO) plotted with NEXAFS for both the multilayer of drop cast (DC) nanoparticles and monolayer of electrosprayed (ESD) nanoparticles after sputtering and annealing. The sets of data are normalised to the intensity of the LUMO peak at around 458 eV.

The process was repeated for the sputtered and annealed samples, with the plots shown in Figure 6.16. However, the calculations of the intensity ratios were not possible, as the error in the normalisation to the LUMO peak, in combination with that of the peak fitting alone is too large for an accurate comparison. It is therefore again not possible to see evidence of charge transfer.

6.4 Discussion

Two methods were used for the deposition of TiO_2 nanoparticles onto a gold surface. Results suggest that the only significant difference between the two methods was the amount of nanoparticles deposited; drop casting resulted in a greater coverage of the metal surface than electrospray deposition. This seemed to be the maximum amount achievable with electrospray, as further rounds of deposition failed to increase the coverage. A benefit of the electrospray deposition in the setup described in this study is that it takes place with the sample under UHV conditions. This will allow levels of impurities to be minimised when compared to drop casting, which took place in the open atmosphere [207]. It was suggested that a thin multilayer coverage may have been achieved with drop casting, but this would have to be confirmed with further analysis. In fact, the depleted intensities of the HOMO plot when compared to the NEXAFS for the drop cast sample (Figure 6.15) would suggest that a multilayer was not achieved, since otherwise no depletion would be expected.

Despite the density of states plots suggesting the possibility of charge transfer from the Au surface into the LUMO of the TiO_2 nanoparticles for all samples, there was no evidence of this seen in any of the RPES maps. It could perhaps be expected that no charge transfer would occur in this direction due to the formation of a Schottky barrier between the semiconductor and the metal. While the electrons in the TiO_2 have energy provided by the incident X-rays to allow them to overcome this barrier in the forwards direction, the barrier acts to hinder the movement of non-excited electrons in the reverse direction. This is a property of the TiO_2/Au combination which is exploited to decrease recombination of electron-hole pairs, and thus increase efficiency, in solar cells [109, 128, 192]. To achieve transfer in

the reverse direction, a defect and strain-free gold nanoparticle-TiO_2 interface has been favoured [120], such that localized surface plasmon resonance (LSPR) bands, occurring when the frequency of photons matches the natural frequency of the surface free electrons [121], excite energetically 'hot' electrons which are then able to overcome the Schottky barrier. However, if a Schottky barrier had formed in this study, the Fermi level of Au would be expected to lie at a lower energy than the LUMO of TiO_2 in the band gap of the semiconductor. The fact that it instead lay above the LUMO suggests that a Schottky barrier did not form, which may be due to a lack of intimate contact between the relatively large nanoparticles and the metal substrate.

Evidence of participator decay from the LUMOs was seen in features of the measured Ti RPES maps for each of the TiO_2 on Au samples. However, the core-hole clock type analyses performed in each case could not provide direct evidence of charge transfer from the TiO_2 nanoparticles into the Au surface on the timescale of the core-hole lifetime. Although the signal to noise ratio for the sputtered and annealed samples made the calculation impossible, it was able to be performed for the pristine samples. The difference in the ratios of the participator to the NEXAFS intensities for the drop cast multilayer and electrosprayed monolayer of nanoparticles was far too small relative to the error associated with their calculation to suggest definitive evidence of charge transfer. The cause again may be that the physical system of TiO_2 on Au explored in this study did not provide a sufficiently intimate contact between the metal and the semiconductor to allow charge transfer across the interface [208].

Decreasing XPS ratios of relative intensities of Ti:Au after sputtering and annealing may suggest that the nanoparticles were made smaller by the treatments, but could also be due to some nanoparticles being removed

completely. To directly measure the size of the nanoparticles, a microscopy technique such as transmission electron microscopy (TEM) or scanning electron microscopy (SEM) could be used. If this method of sputtering the previously deposited TiO_2 nanoparticles was successful in decreasing their diameters, it is possible that they could be made small enough to act as quantum dots (QDs). QDs are nanoscale semiconductor crystals which contain just a hundred to a thousand atoms [209]. As the size becomes comparable to that of the de Broglie wavelength of the charge carriers, the charge carriers themselves become confined within three dimensions, such that a series of discrete electronic states are the result [192]. A key feature of QDs is that the band gap of the semiconductor becomes dependant on the size of the nanoparticle: it increases as the particle size decreases and the electronic states become more discrete [210]. This presents the idea that the band gap is now a tuneable property, such that the wavelength of light absorbed and emitted may be selected. Quantum confinement in TiO_2 can therefore enable increased efficiency in solar cells since the tuneable band gap can allow the absorption of light across a broader spectrum, including at wavelengths that traditional solar cells might miss [209].

6.5 Conclusions

Titanium dioxide nanoparticles were deposited onto a gold surface and the interactions between the two materials were investigated with X-ray based analytical techniques. The aim of the study was to provide information that may help with the development of technology for TiO_2 photocatalysed cells for hydrogen production through solar water splitting. Drop casting may have resulted in the deposition of a multilayer of nanoparticles, to and from which charge transfer does not occur, but this must be confirmed with

AFM. Evidence of participator decay was observed with RPES, attributed to resonant enhancement of the photoemission of the HOMO and HOMO-1 after participator decay involving electrons excited into the LUMOs within the multilayer. Less than a monolayer of surface coverage was achieved via electrospray deposition of the nanoparticle suspension, and although evidence of participator decay was again observed, no direct evidence of charge transfer was measured either from the metal surface to the nanoparticles, or in the reverse direction. It was proposed that a lack of intimate contact between the nanoparticles and the metal substrate meant that a Schottky barrier was not formed at the metal/semiconductor interface, while also restricting charge transfer in the direction of TiO_2 to Au. For use in solar cells for efficient water splitting, charge transfer between the the semiconductor photocatalyst and metal cocatalyst is essential, so the derived system of nanoparticles on a crystal substrate in this study would likely be a poor choice for solar cell construction. Results of XPS measurements may suggest that Ar^+ ion sputtering and annealing in oxygen resulted in decreased size of the deposited nanoparticles, opening up the possibility of using this method to introduce quantum confinement effects into the semiconductor for improvements of solar cell efficiency. Future studies may look to confirm particle size changes with electron microscopy techniques.

Chapter 7

Conclusions and Future Work

This thesis aims to investigate materials for potential applications in hydrogen production and storage technologies, using X-ray based analytical techniques including X-ray photoelectron spectroscopy (XPS), near-edge X-ray absorption fine structure (NEXAFS) spectroscopy and resonant photoemission spectroscopy (RPES).

Chapter 3 describes a device designed for further improvement of these UHV-based analytical techniques for their use in investigating the reactions of materials at elevated pressures, such as those associated with solid-state hydrogen storage. The device acts to provide a method for rapid transfer of a flat sample from reaction to analysis conditions, such that the measured results could more accurately represent the actual behaviour of the sample under those reaction conditions. Additionally, the sample is not exposed to other unwanted elements such as air during the transfer, something that would again affect results. The device employs a simple mechanism which enables transfer from a reaction chamber, with a gas pressure of up to 4.5 bar, to an analysis chamber through a differential pumping scheme, down a pressure gradient of 11 orders of magnitude. Taking just 5 minutes, and

requiring no evacuation of the reaction chamber, the time for the transfer is comparable to similar systems in the literature, while also allowing for easy transfer in the opposite direction. The pressures in the analysis chamber were not as low as is ideally used for XPS analysis ($\leq 10^{-9}$ mbar), but this could potentially be achieved in the future by introducing another differentially pumped stage to the system.

Chapter 4 served as a 'proof of concept' for the device designed in the previous chapter. A titanium dioxide crystal was sputtered with argon ions in the analysis chamber to create a defective surface, before it was transferred to the reaction chamber for prolonged air exposure. Rapid transfer back into position for XPS analysis enabled the observation that most of the defective titanium sites had been fully oxidised, successfully proving the capabilities of the device. For a completely defect-free structure, annealing of the crystal is required, a capability currently lacking on the transfer system. The installation of a radiative heating device mounted in the reaction chamber could enable this for future studies. Achieving higher pressures of gas in the reaction chamber is also a possibility, but would require changes to some parts. However, the system was designed to be compatible for reactions involving hydrogen, such that investigations of reactions of solid-state storage materials could be an obvious next step.

The effects of exposure to hydrogen at 1 bar were investigated in Chapter 5 for the high entropy alloy $(Ti_{0.65}Zr_{0.35})_{1.05}MnCr_{0.8}Fe_{0.2}$, a material with promising properties for storage applications. The first hydrogenation, or activation, of the alloy is a process which depends heavily on surface interactions. It is for this reason that XPS and NEXAFS could be used effectively to investigate changes in the surface composition and oxidation states of the constituent metals after a variety of activation-like treatments. Element-specific surface segregation led to large changes in the surface composition

after each treatment, with manganese playing a significant role after heating in hydrogen; it appeared to sacrificially oxidise on the surface, such that oxides of chromium and iron could be reduced to metallic states and left available as sites for hydrogen dissociation. Further enhancement in the effects of hydrogenation seen after a second cycle suggest that investigations of behaviour after increasing numbers of cycles could help to explain the strong cycling stability of the alloy seen through measurements of storage capacities elsewhere. The study in this chapter provided a 'snapshot' of the alloy surface before and after exposure to activation-like conditions, it is therefore suggested that future studies may look at more incremental variations in temperature and pressure, in efforts to determine the mechanism of the process.

Finally, the interaction of titanium dioxide (TiO_2) and gold was investigated in Chapter 6 with the aim of developing a further understanding of the interactions between the two materials for potential applications in devices for solar water splitting. In nanoparticle form, the TiO_2 was deposited onto the gold surface via drop casting and via electrospray deposition, with a larger coverage achieved with the drop casting method. XPS, NEXAFS and RPES were used to probe the charge transfer dynamics between the two materials, but found no evidence of charge transfer in either direction. XPS results may suggest that argon ion sputtering of the deposited nanoparticles was successful in reducing their size, providing a potentially unexplored method of introducing quantum confinement effects into the semiconductor, but more analysis is required to confirm the particle sizes. Future studies may look to investigate this further, since quantum confinement effects may be used to increase efficiencies for solar water splitting through improved charge separation and selective absorption of different wavelengths of radiation.

Overall, this thesis has demonstrated the effective application of surface-sensitive techniques for the analysis of materials with potential for use in hydrogen storage and production technologies, and as such highlighted the importance of understanding surface interactions when considering complete systems.

References

[1]D. M. Mattox, *Handbook of Physical Vapor Deposition (PVD) Processing*, Second Edition (William Andrew, Oxford, UK, 2010).

[2]D. E. Starr, Z. Liu, M. Hävecker, A. Knop-Gerickec, and H. Bluhm, "Investigation of solid/vapor interfaces using ambient pressure X-ray photoelectron spectroscopy", Chemical Society Reviews **42**, 5833–5857 (2013).

[3]ThermoFisher, *XPS Simplified: What is X-ray photoelectron spectroscopy (XPS)?*, `https://xpssimplified.com/whatisxps.php`, (accessed: 18.05.2020).

[4]A. Polini and F. Yang, "Nanofiber composites for biomedical applications", in (Woodhead Publishing, 2017) Chap. 5.

[5]M. P. Seah and W. A. Dench, "Quantitative Electron Spectroscopy of Surfaces: A standard data base for electron inelastic mean free paths in solids", Surface and Interface Analysis **1**, 2–11 (1979).

[6]H. Konno, "Materials science and engineering of carbon", in (Butterworth-Heinemann, 2016) Chap. 8, pp. 153–171.

[7]J. Maibach, C. Xu, S. K. Eriksson, J. Åhlund, T. Gustafsson, H. Siegbahn, H. Rensmo, K. Edström, and M. Hahlin, "A high pressure X-ray photoelectron spectroscopy experimental method for characterization of

solid-liquid interfaces demonstrated with a Li-ion battery system", Review of Scientific Instruments **86**, 044101-1–044101-8 (2015).

[8]D. W. Goodman, "Catalysis: from single crystals to the 'real world'", Surface Science **299**, 837–848 (1994).

[9]H. Siegbahn and K. Siegbahn, "ESCA applied to liquids", Journal of Electron Spectroscopy and Related Phenomena **2**, 319–325 (1973).

[10]H. J. Ruppender, M. Grunze, C. W. Kong, and M. Wilmers, "In situ X-ray Photoelectron Spectroscopy of Surfaces at Pressures up to 1 mbar", Surface and Interface Analysis **15**, 245–253 (1990).

[11]J. Pantförder, S. Pöllmann, J. F. Zhu, D. Borgmann, R. Denecke, and H. P. Steinrück, "New setup for in situ X-ray photoelectron spectroscopy from ultrahigh vacuum to 1 mbar", Review of Scientific Instruments **76**, 014102-1–014102-9 (2005).

[12]H. Siegbahn, "Electron spectroscopy for chemical analysis of liquids and solutions", Journal of Physical Chemistry **89**, 897–909 (1985).

[13]R. W. Joyner, M. W. Roberts, and K. Yates, "A "high-pressure" electron spectrometer for surface studies", Surface Science **87**, 501–509 (1979).

[14]Z. Novotny, D. Aegerter, N. Comini, B. Tobler, L. Artiglia, U. Maier, T. Moehl, E. Fabbri, T. Huthwelker, T. J. Schmidt, M. Ammann, J. A. van Bokhoven, J. Raabe, and J. Osterwalder, "Probing the solid–liquid interface with tender X-rays: A new ambient-pressure X-ray photoelectron spectroscopy endstation at the Swiss Light Source", Review of Scientific Instruments **91**, 023103-1–023103-10 (2020).

[15]S. Kaya, H. Ogasawara, L.-Å. Näslund, J.-O. Forsell, H. S. Casalongue, D. J. Miller, and A. Nilsson, "Ambient-pressure photoelectron spectroscopy for heterogeneous catalysis and electrochemistry", Catalysis Today **205**, 101–105 (2013).

[16]D. F. Ogletree, G. L. Hendrik Bluhm, and C. S. Fadley, "A differentially pumped electrostatic lens system for photoemission studies in the millibar range", Review of Scientific Instruments **73**, 3872–3877 (2002).

[17]D. W. Blakely, E. I. Kozak, B. A. Sexton, and G. A. Somorjai, "New instrumentation and techniques to monitor chemical surface reactions on single crystals over a wide pressure range (10^{-8}–10^{5} Torr) in the same apparatus", Journal of Vacuum Science and Technology **13**, 1091–1096 (1976).

[18]A. Z. Moshfegh and A. Ignatiev, "Combined high-pressure photocatalytic reactor–UHV system and sample transfer device", Review of Scientific Instruments **59**, 2202–2205 (1988).

[19]A. Ludviksson, J. Yoshihara, and C. T. Campbell, "A high pressure cell and transfer rod for ultrahigh vacuum chambers", Review of Scientific Instruments **66**, 4370–4374 (1995).

[20]Y. Wang, R. McAllister, R. G. Herman, G. W. Simmons, and K. Klier, "Design and construction of a simple UHV-compatible high-pressure reaction cell", Review of Scientific Instruments **63**, 5767–5770 (1992).

[21]D. R. Kahn, E.E.Petersen, and G. A. Somorjai, "The hydrogenolysis of cyclopropane on a platinum stepped single crystal at atmospheric pressure", Journal of Catalysis **34**, 294–306 (1974).

[22]*U.S. Department of Energy and U.S. DRIVE Partnership, Targets for onboard hydrogen storage systems for light-duty vehicles*, `https://www.energy.gov/eere/fuelcells/doe-technical-targets-onboard-hydrogen-storage-light-duty-vehicles`, (accessed: 07.07.2023).

[23]P. H. F. Reijnen, U. van Slooten, A. P. de Jongh, J. H. M. Kuijper, and A. W. Kleyn, "A system for high pressure preparation and UHV char-

acterization of surface reactions", Measurement Science and Technology **1**, 1244–1246 (1990).

[24]C. Kuhrs, M. Swoboda, and W. Weiss, "Single crystal flow reactor for studying reactivities on metal oxide model catalysts at atmospheric pressure to bridge the pressure gap to the adsorption properties determined under UHV conditions", Topics in Catalysis **15**, 13–18 (2001).

[25]E. Laegsgaard, L. Österlund, P. Thostrup, P. B. Rasmussen, I. Stensgaard, and F. Besenbacher, "A high-pressure scanning tunneling microscope", Review of Scientific Instruments **72**, 3537–3542 (2001).

[26]Y. Du, L. Li, X. Wang, and H. Qiu, "A newly designed infrared reflection absorption spectroscopy system for in situ characterization from ultrahigh vacuum to ambient pressure", Applied Spectroscopy **72**, 122–128 (2018).

[27]H. D. Polaschegg, A. Jungel, and E. Schirk, "A high pressure preparation lock for surface analysis", Surface and Interface Analysis **1**, 100–103 (1979).

[28]A. E. Nelson and K. H. Schulz, "High pressure reaction cell and transfer mechanism for ultrahigh vacuum spectroscopic chambers", Review of Scientific Instruments **71**, 2471–2475 (2000).

[29]D. W. Goodman, R. D. Kelley, T. E. Madey, and J. T. Y. Jr., "Kinetics of the hydrogenation of CO over a single crystal nickel catalyst", Journal of Catalysis **63**, 226–234 (1980).

[30]S. H. Oh, G. B. Fisher, J. E. Carpenter, and D. W. Goodman, "Comparative kinetic studies of CO-O_2 and CO-NO reactions over single crystal and supported rhodium catalysts", Journal of Catalysis **100**, 360–376 (1986).

[31]H. P. Bonzel and H. J. Krebs, "Enhanced rate of carbon deposition during fischer-tropsch synthesis on K promoted Fe", Surface Science **109**, L527–L531 (1981).

[32]H. P. Bonzel and H. J. Krebs, "Surface science approach to heterogeneous catalysis: CO hydrogenation on transition metals", Surface Science **117**, 639–658 (1982).

[33]H. D. Polaschegg, *Vacuum analysis and sample transfer system - with analyser lying between reaction vessel and transfer drive, US Patent: 3746217*, (Dec. 15, 1977) `https://worldwide.espacenet.com/patent/search/family/005979600/publication/DE2624697A1?q=leybold-heraeus%20sample%20transfer`.

[34]L. W. Hobbs, "Preparation of thin films of moisture-sensitive crystals for transmission electron microscopy", Journal of Physics E: Scientific Instruments **3**, 85–88 (1970).

[35]C. Solliard and M. Rappaz, "Air-lock system for the transfer of reactive samples to the Philips EM 300S electron microscope", Review of Scientific Instruments **49**, 101–103 (1978).

[36]R. M. Gaume and L.-M. Joubert, "Airtight container for the transfer of atmosphere-sensitive materials into vacuum-operated characterization instruments", Review of Scientific Instruments **82**, 123705-1–4 (2011).

[37]M. Balat, "Potential importance of hydrogen as a future solution to environmental and transportation problems", International Journal of Hydrogen Energy **33**, 4013–4029 (2008).

[38]P. Millet, "Hydrogen storage in hydride-forming materials", in *Advances in Hydrogen Production, Storage and Distribution*, edited by A. Basile and A. Iulianelli (Woodhead Publishing, 2014) Chap. 14, pp. 368–409.

[39]N. Rusman and M. Dahari, "A review on the current progress of metal hydrides material for solid-state hydrogen storage applications", International Journal of Hydrogen Energy **41**, 12108–12126 (2016).

[40]M. Veenstra, J. Purewal, C. Xu, J. Yang, R. Blaser, A. Sudik, D. Siegel, Y. Ming, D. Liu, H. Chi, M. Gaab, L. Arnold, and U. Muller, "Technical Report: Ford/BASF/UM Activities in Support of the Hydrogen Storage Engineering Center of Excellence", U.S. Department of Energy Office of Scientific and Technical Information, 1–131 (2015).

[41]D. Chandra, "Intermetallics for hydrogen storage", in *Solid-state hydrogen storage*, edited by G. S. Walker (Woodhead Publishing Ltd, Cambridge, UK, 2008) Chap. 12, pp. 315–356.

[42]M. Dornheim, "Thermodynamics of Metal Hydrides: Tailoring Reaction Enthalpies of Hydrogen Storage Materials", in *Thermodynamics - Interaction Studies - Solids, Liquids and Gases*, edited by J. C. M. Piraján (InTechOpen, 2011) Chap. 33.

[43]S. W. Lambert, D. Chandra, W. N. Cathey, F. E. Lynch, and R. C. Bowman Jr., "Investigation of hydriding properties of $LaNi_{4.8}Sn_{0.2}$, $LaNi_{4.27}Sn_{0.24}$ and $La_{0.9}Gd_{0.1}Ni_5$ after thermal cycling and aging", Journal of Alloys and Compounds **187**, 113–135 (1992).

[44]J.-C. Crivello, B. Dam, R. V. Denys, M. Dornheim, D. M. Grant, J. Huot, T. R. Jensen, P. de Jongh, M. Latroche, C. Milanese, D. Milčius, G. S. Walker, C. J. Webb, C. Zlotea, and V. A. Yartys, "Review of magnesium hydride-based materials: development and optimisation", Applied Physics A **122**, 1–20 (2016).

[45]M. Paskevicius, D. A. Sheppard, and C. E. Buckley, "Thermodynamic Changes in Mechanochemically Synthesized Magnesium Hydride Nanoparticles", Journal of the American Chemical Society **132**, 5077–5083 (2010).

[46]W. P. Kalisvaart, C. T. Harrower, J. Haagsma, B. Zahiri, E. J. Luber, C. Ophus, E. Poirier, H. Fritzsche, and D. Mitlin, "Hydrogen storage in binary and ternary Mg-based alloys: A comprehensive experimental study", International Journal of Hydrogen Energy **35**, 2091–2103 (2010).

[47]W. Grochala and P. P. Edwards, "Thermal Decomposition of the Non-Interstitial Hydrides for the Storage and Production of Hydrogen", Chemical Reviews **104**, 1283–1316 (2004).

[48]S. Srinivasan, D. Escobar, Y. Goswami, and E. Stefanakos, "Effects of catalysts doping on the thermal decomposition behavior of $Zn(BH_4)_2$", International Journal of Hydrogen Energy **33**, 2268–2272 (2008).

[49]M. B. Ley, L. H. Jepsen, Y.-S. Lee, Y. W. Cho, J. M. B. von Colbe, M. Dornheim, M. Rokni, J. O. Jensen, M. Sloth, Y. Filinchuk, J. E. Jørgensen, F. Besenbacher, and T. R. Jensen, "Complex hydrides for hydrogen storage – new perspectives", Materials Today **17**, 122–128 (2014).

[50]Z. G. Huang, Z. P. Guo, A. Calka, D. Wexler, C. Lukey, and H. K. Liu, "Effects of iron oxide (Fe_2O_3, Fe_3O_4) on hydrogen storage properties of Mg-based composites", Journal of Alloys and Compounds **422**, 299–304 (2006).

[51]N. C. Smythe and J. C. Gordon, "Ammonia Borane as a Hydrogen Carrier: Dehydrogenation and Regeneration", European Journal of Inorganic Chemistry **2010**, 499–656 (2010).

[52]H. T. Hwang, A. Al-Kukhun, and A. Varma, "Hydrogen for Vehicle Applications from Hydrothermolysis of Ammonia Borane: Hydrogen Yield, Thermal Characteristics, and Ammonia Formation", Industrial & Engineering Chemistry Research **49**, 10994–11000 (2010).

[53]Q.-L. Zhu and Q. Xu, "Liquid organic and inorganic chemical hydrides for high-capacity hydrogen storage", Energy & Environmental Science **8**, 478–512 (2015).

[54]G. G. Libowitz, H. F. Hayes, and T. R. G. G. Jr, "The system zirconium-nickel and hydrogen", Journal of Physical Chemistry **62**, 76–79 (1958).

[55]A. Mohammadi, Y. Ikeda, P. Edalati, M. Mito, B. Grabowski, H.-W. Li, and K. Edalati, "High-entropy hydrides for fast and reversible hydrogen storage at room temperature: Binding-energy engineering via first-principles calculations and experiments", Acta Materialia **236**, 118117-1–14 (2022).

[56]H. Yu, X. Yang, X. Jiang, Y. Wu, S. Chen, W. Lin, Y. Wu, L. Xie, X. Li, and J. Zheng, "$LaNi_{5.5}$ particles for reversible hydrogen storage in N-ethylcarbazole", Nano Energy **80**, 105476 (2021).

[57]J. O. Abe, A. Popoola, E. Ajenifuja, and O. Popoola, "Hydrogen energy, economy and storage: Review and recommendation", International Journal of Hydrogen Energy **44**, 15072–15086 (2019).

[58]B. S. Murty, J. W. Yeh, and S. Ranganathan, "Intermetallics, Interstitial Compounds and Metallic Glasses in High-Entropy Alloys", in *High-Entropy Alloys* (Butterworth-Heinemann, London, UK, 2014) Chap. 7, pp. 119–131.

[59]K.-H. Young, S. Chang, and X. Lin, "C14 Laves Phase Metal Hydride Alloys for Ni/MH Batteries Applications", Batteries **3**, 1–33 (2017).

[60]J. Liu, L. Sun, J. Yang, D. Guo, D. Chen, L. Yang, and P. Xiao, "Ti–Mn hydrogen storage alloys: from properties to applications", RSC Advances **12**, 35744–35755 (2022).

[61]B.-H. Liu, D.-M. Kim, K.-Y. Lee, and J.-Y. Lee, "Hydrogen storage properties of $TiMn_2$-based alloys", Journal of Alloys and Compounds **240**, 214–218 (1996).

[62]G. Principi, F. Agresti, A. Maddalena, and S. L. Russo, "The problem of solid state hydrogen storage", Energy **34**, 2087–2091 (2009).

[63]G. Sandrock and P. D. Goodell, "Surface poisoning of $LaNi_5$, FeTi and (Fe,Mn)Ti by O_2, Co and H_2O", Journal of the Less Common Metals **73**, 161–168 (1980).

[64]K. B. Park, J. O. Fadonougbo, C.-S. Park, J.-H. Lee, T.-W. Na, H.-S. Kang, W.-S. Ko, and H.-K. Park, "Effect of Fe substitution on first hydrogenation kinetics of TiFe-based hydrogen storage alloys after air exposure", International Journal of Hydrogen Energy **46**, 30780–30789 (2021).

[65]P. Modi and K.-F. Aguey-Zinsou, "Titanium-iron-manganese ($TiFe_{0.85}Mn_{0.15}$) alloy for hydrogen storage: Reactivation upon oxidation", International Journal of Hydrogen Energy **44**, 16757–16764 (2019).

[66]M. Bououdina, D. Fruchart, S. Jacquet, L. Pontonnier, and J. L. Soubeyroux, "Effect of nickel alloying by using ball milling on the hydrogen absorption properties of TiFe", International Journal of Hydrogen Energy **24**, 885–890 (1999).

[67]M. Abe and T. Kuji, "Hydrogen absorption of TiFe alloy synthesized by ball milling and post-annealing", Journal of Alloys and Compounds **446-447**, 200–203 (2007).

[68]S.-M. Lee and T.-P. Perng, "Effect of the second phase on the initiation of hydrogenation of $TiFe_{1-x}M_x$ (M = Cr,Mn) alloys", International Journal of Hydrogen Energy **19**, 259–263 (1994).

[69]T. H. Jang, J. I. Han, and J.-Y. Lee, "Effect of substitution of titanium by zirconium in TiFe on hydrogenation properties", Journal of the Less Common Metals **119**, 237–246 (1986).

[70]S. Lanyin, L. Fangjie, and B. Deyou, "An advanced TiFe series hydrogen storage material with high hydrogen capacity and easily activated properties", International Journal of Hydrogen Energy **15**, 259–262 (1990).

[71]A. Guéguen and M. Latroche, "Influence of the addition of vanadium on the hydrogenation properties of the compounds $TiFe_{0.9}V_x$ and $TiFe_{0.8}Mn_{0.1}V_x$ (x = 0, 0.05 and 0.1)", Journal of Alloys and Compounds **509**, 5562–5566 (2011).

[72]P. Jain, C. Gosselin, and J. Huot, "Effect of Zr, Ni and Zr_7Ni_{10} alloy on hydrogen storage characteristics of TiFe alloy", International Journal of Hydrogen Energy **40**, 16921–16927 (2015).

[73]J.-W. Yeh, S.-K. Chen, S.-J. Lin, J.-Y. Gan, T.-S. Chin, T.-T. Shun, C.-H. Tsau, and S.-Y. Chang, "Nanostructured High-Entropy Alloys with Multiple Principal Elements: Novel Alloy Design Concepts and Outcomes", Advanced Engineering Materials **6**, 273–349 (2004).

[74]M. M. Nygård, G. Ek, D. Karlsson, M. H. Sørby, M. Sahlberg, and B. C. Hauback, "Counting electrons - A new approach to tailor the hydrogen sorption properties of high-entropy alloys", Acta Materialia **175**, 121–129 (2019).

[75]S. Akrami, P. Edalati, M. Fuji, and K. Edalati, "High-entropy ceramics: Review of principles, production and applications", Materials Science and Engineering: R: Reports **146**, 100644-1–64 (2021).

[76]X. Xin, R. Johansson, M. Wolff, and B. Hjörvarsson, "Hydrogen in vanadium: Site occupancy and isotope effects", Physical Review B **93**, 134107-1–5 (2016).

[77]M. Sahlberg, D. Karlsson, C. Zlotea, and U. Jansson, "Superior hydrogen storage in high entropy alloys", Scientific Reports **6**, 36770-1–6 (2016).

[78]N. K. Katiyar, K. Biswas, J.-W. Yeh, S. Sharma, and C. S. Tiwary, "A perspective on the catalysis using the high entropy alloys", Nano Energy **88**, 106261-1–9 (2021).

[79]F. Marques, M. Balcerzak, F. Winkelmann, G. Zepon, and M. Felderhoff, "Review and outlook on high-entropy alloys for hydrogen storage", Energy & Environmental Science **14**, 5191–5227 (2021).

[80]P. Edalati, R. Floriano, A. Mohammadi, Y. Li, G. Zepon, H.-W. Li, and K. Edalati, "Reversible room temperature hydrogen storage in high-entropy alloy TiZrCrMnFeNi", Scripta Materialia **178**, 387–390 (2020).

[81]K. Balasubramanian, S. V. Khare, and D. Gall, "Valence electron concentration as an indicator for mechanical properties in rocksalt structure nitrides, carbides and carbonitrides", Acta Materialia **152**, 175–185 (2018).

[82]D. B. Miracle and O. N. Senkov, "A critical review of high entropy alloys and related concepts", Acta Materialia **122**, 448–511 (2017).

[83]P. E. de Jongh, "Keeping out the oxygen", Nature Materials **10**, 265–266 (2011).

[84]S. Sleiman and J. Huot, "Effect of particle size, pressure and temperature on the activation process of hydrogen absorption in TiVZrHfNb high entropy alloy", Journal of Alloys and Compounds **861**, 158615-1–9 (2021).

[85]K. B. Park, T.-W. Na, Y. D. Kim, J.-Y. Park, J.-W. Kang, H.-S. Kang, K. Park, and H.-K. Park, "Characterization of microstructure and surface oxide of $Ti_{1.2}Fe$ hydrogen storage alloy", International Journal of Hydrogen Energy **46**, 13082–13087 (2021).

[86]D. M. Dreistadt, T.-T. Le, G. Capurso, J. M. B. von Colbe, A. Santhosh, C. Pistidda, N. Scharnagl, H. Ovri, C. Milanese, P. Jerabek, T. Klassen, and J. Jepsen, "An effective activation method for industrially produced TiFeMn powder for hydrogen storage", Journal of Alloys and Compounds **919**, 165847-1–14 (2022).

[87]X. Yu, Z. Wu, T. Huang, J. Cheng, B. Xia, and N. Xu, "Effect of surface oxide layer on activation performance of hydrogen storage alloy $TiMn_{1.25}Cr_{0.25}$", International Journal of Hydrogen Energy **29**, 81–86 (2004).

[88]H. Uchida, "Surface processes of H_2 on rare earth based hydrogen storage alloys with various surface modifications", International Journal of Hydrogen Energy **24**, 861–869 (1999).

[89]W. E. Wallace, R. F. Karlicek, and H. Imamura, "Mechanism of hydrogen absorption by lanthanum-nickel ($LaNi_5$)", Journal of Physical Chemistry **83**, 1708–1712 (1979).

[90]H. Pan, Y. Zhu, M. Gao, Y. Liu, R. Li, Y. Lei, and Q. Wang, "A study on the cycling stability of the Ti–V-based hydrogen storage electrode alloys", Journal of Alloys and Compounds **364**, 271–279 (2004).

[91]P. Lv and J. Huot, "Hydrogen storage properties of $Ti_{0.95}FeZr_{0.05}$, $TiFe_{0.95}Zr_{0.05}$ and $TiFeZr_{0.05}$ alloys", International Journal of Hydrogen Energy **41**, 22128–22133 (2016).

[92]Y. Shenzhong, Y. Rong, H. Tiesheng, Z. Shilong, and C. Bingzhao, "A study of the activation of FeTi and $Fe_{0.9}$ $TiMn_{0.1}$", International Journal of Hydrogen Energy **13**, 433–437 (1988).

[93]K. Edalati, J. Matsuda, H. Iwaoka, S. Toh, E. Akiba, and Z. Horita, "High-pressure torsion of TiFe intermetallics for activation of hydrogen

storage at room temperature with heterogeneous nanostructure", International Journal of Hydrogen Energy **38**, 4622–4627 (2013).

[94]K. Edalati, J. Matsuda, A. Yanagida, E. Akiba, and Z. Horita, "Activation of TiFe for hydrogen storage by plastic deformation using groove rolling and high-pressure torsion: Similarities and differences", International Journal of Hydrogen Energy **39**, 15589–15594 (2014).

[95]L. E. R. Vega, D. R. Leiva, R. M. L. Neto, W. B. Silva, R. A. Silva, T. T. Ishikawa, C. S. Kiminami, and W. J. Botta, "Mechanical activation of TiFe for hydrogen storage by cold rolling under inert atmosphere", International Journal of Hydrogen Energy **43**, 2913–2918 (2018).

[96]F. Guo, K. Namba, H. Miyaoka, A. Jain, and T. Ichikawa, "Hydrogen storage behavior of TiFe alloy activated by different methods", Materials Letters: X **9**, 100061-1–5 (2021).

[97]J. Balasubramanian, J. Lemere, S. S. Khan, and N. R. Agarwal, "Plasmonic nanosensors and their spectroscopic applications—current trends and future perspectives", in *Molecular and Laser Spectroscopy, Advances and Applications*, edited by V. P. Gupta (Elsevier, 2022) Chap. 10, pp. 337–372.

[98]P. Lv, M. N. Guzik, S. Sartori, and J. Huot, "Effect of ball milling and cryomilling on the microstructure and first hydrogenation properties of TiFe+4wt.% Zr alloy", Journal of Materials Research and Technology **8**, 1828–1834 (2019).

[99]H. Emami, K. Edalati, J. Matsuda, E. Akiba, and Z. Horita, "Hydrogen storage performance of TiFe after processing by ball milling", Acta Materialia **88**, 190–195 (2015).

[100]C.-H. Chiang, Z.-H. Chin, and T.-P. Perng, "Hydrogenation of TiFe by high-energy ball milling", Journal of Alloys and Compounds **307**, 259–265 (2000).

[101]C. Zhang, Y. Wu, L. You, X. Cao, Z. Lu, and X. Song, "Investigation on the activation mechanism of hydrogen absorption in TiZrNbTa high entropy alloy", Journal of Alloys and Compounds **781**, 613–620 (2019).

[102]*International Renewable Energy Agency - energy Transition: Hydrogen*, https://www.irena.org/Energy-Transition/Technology/Hydrogen#:~:text=As%20at%20the%20end%20of,around%204%25%20comes%20from%20electrolysis, (accessed: 2.10.2023).

[103]*International Energy Agency - energy System: Hydrogen*, https://www.iea.org/energy-system/low-emission-fuels/hydrogen, (accessed: 2.10.2023).

[104]*International Energy Agency - energy System: Electrolysers*, https://www.iea.org/energy-system/low-emission-fuels/electrolysers, (accessed: 2.10.2023).

[105]J. Nowotny, C. C. Sorrell, L. R. Sheppard, and T. Bak, "Solar-hydrogen: Environmentally safe fuel for the future", International Journal of Hydrogen Energy **30**, 521–544 (2005).

[106]T. H. Syed and W. Wei, "Technoeconomic Analysis of Dye Sensitized Solar Cells (DSSCs) with WS2/Carbon Composite as Counter Electrode Material", Inorganics **10**, 1–12 (2022).

[107]A. Fujishima and K. Honda, "Electrochemical Photolysis of Water at a Semiconductor Electrode", Nature **238**, 37–38 (1972).

[108]J. Nowotny, T. Bak, M. K. Nowotny, and L. R. Sheppard, "Titanium dioxide for solar-hydrogen I. Functional properties", International Journal of Hydrogen Energy **32**, 2609–2629 (2007).

[109]X. Chen, S. Shen, L. Guo, and S. S. Mao, "Semiconductor-based Photocatalytic Hydrogen Generation", Chemical Reviews **110**, 6503–6570 (2010).

[110]B. Gupta, A. A. Melvin, T. Matthews, S. Dash, and A. K. Tyagi, "TiO_2 modification by gold (Au) for photocatalytic hydrogen (H_2) production", Renewable and Sustainable Energy Reviews **58**, 1366–1375 (2016).

[111]D. M. Antonelli and J. Y. Ying, "Synthesis of Hexagonally Packed Mesoporous TiO_2 by a Modified Sol–Gel Method", Angewandte Chemie International Edition **34**, 1913–2061 (1995).

[112]Z. Chen, P. Li, R. Anderson, X. Wang, X. Zhang, L. Robison, L. R. Redfern, S. Moribe, T. Islamoglu, D. A. Gómez-Gualdrón, T. Yildirim, J. F. Stoddart, and O. K. Farha, "Balancing volumetric and gravimetric uptake in highly porous materials for clean energy", Science **368**, 297–303 (2020).

[113]M. Grätzel, "Perspectives for dye-sensitized nanocrystalline solar cells", Progress in Photovoltaics: Research and Applications **8**, 171–185 (2000).

[114]M. Grätzel, "Dye-sensitized solar cells", Journal of Photochemistry and Photobiology C: Photochemistry Reviews Volume 4, Issue 2, 31 October 2003, Pages 145-153 **4**, 145–154 (2003).

[115]M. K. Nazeeruddin, A. Kay, I. Rodicio, R. Humphry-Baker, E. Mueller, P. Liska, N. Vlachopoulos, and M. Grätzel, "Conversion of light to electricity by cis-X2bis(2,2'-bipyridyl-4,4'-dicarboxylate)ruthenium(II) charge-transfer sensitizers (X = Cl^-, Br^-, I^-, CN^-, and SCN^-) on nanocrystalline titanium dioxide electrodes", Journal of the American Chemical Society **115**, 6382–6390 (1993).

[116]B. O'Regan and M. Grätzel, "A low-cost, high-efficiency solar cell based on dye-sensitized colloidal TiO_2 films", Nature **353**, 737–740 (1991).

[117]J. Huang, W. Guo, Y. Hu, and W. D. Wei, "Plasmonic metal-semiconductor heterostructures for hot-electron-driven photochemistry", MRS Bulletin **45**, 37–42 (2020).

[118]G. Liu, K. Du, J. Xu, G. Chen, M. Gu, C. Yang, K. Wang, and H. Jakobsen, "Plasmon-dominated photoelectrodes for solar water splitting", Journal of Materials Chemistry A **5**, 4233–4253 (2017).

[119]R. T. Tung, "The physics and chemistry of the Schottky barrier height", Applied Physics Reviews **1**, 01134-1–54 (2014).

[120]S. Atta, A. M. Penningtona, and F. E. C. anf Laura Fabris, "TiO_2 on Gold Nanostars Enhances Photocatalytic Water Reduction in the Near-Infrared Regime", Chem **4**, 2140–2153 (2018).

[121]A. Wang, S. Wu, J. Dong, R. Wang, J. Wang, J. Zhang, S. Zhong, and S. Bai, "Interfacial facet engineering on the Schottky barrier between plasmonic Au and TiO_2 in boosting the photocatalytic CO_2 reduction under ultraviolet and visible light irradiation", Chemical Engineering Journal **404**, 127145-1–9 (2021).

[122]J. S. DuChene, B. C. Sweeny, A. C. Johnston-Peck, D. Su, E. A. Stach, and W. D. Wei, "Prolonged Hot Electron Dynamics in Plasmonic-Metal/Semiconductor Heterostructures with Implications for Solar Photocatalysis", Angewandte Chemie International Edition **53**, 7887–7891 (2014).

[123]J. L. Storck, M. Dotter, S. Adabra, M. Surjawidjaja, B. Brockhagen, and T. Grothe, "Long-Term Stability Improvement of Non-Toxic Dye-Sensitized Solar Cells via Poly(ethylene oxide) Gel Electrolytes for Future Textile-Based Solar Cells", Polymerss **12**, 1–15 (2020).

[124]M. V. Dozzi, L. Prati, P. Cantonc, and E. Selli, "Effects of gold nanoparticles deposition on the photocatalytic activity of titanium dioxide un-

der visible light", Physicsal Chemistry Chemical Physics **11**, 7171–7180 (2009).

[125]G. L. Chiarello, E. Selli, and L. Forni, "Photocatalytic hydrogen production over flame spray pyrolysis-synthesised TiO_2 and Au/TiO_2", Applied Catalysis B: Environmental **84**, 332–339 (2008).

[126]G. R. Bamwenda, S. Tsubota, T. Nakamura, and M. Haruta, "Photoassisted hydrogen production from a water-ethanol solution: a comparison of activities of Au-TiO_2 and Pt-TiO_2", Journal of Photochemistry and Photobiology A: Chemistry **89**, 177–189 (1995).

[127]T. Sreethawonga and S. Yoshikawa, "Comparative investigation on photocatalytic hydrogen evolution over Cu-, Pd-, and Au-loaded mesoporous TiO_2 photocatalysts", Catalysis Communications **6**, 661–668 (2005).

[128]A. Naldoni, M. Altomare, G. Zoppellaro, N. Liu, Š. Kment, R. Zbořil, and P. Schmuki, "Photocatalysis with Reduced TiO_2: From Black TiO_2 to Cocatalyst-Free Hydrogen Production", ACS Catalysis **9**, 345–364 (2019).

[129]Y. Ikuma and H. Bessho, "Effect of Pt concentration on the production of hydrogen by a TiO_2 photocatalyst", International Journal of Hydrogen Energy **32**, 2689–2692 (2007).

[130]D. Jing, Y. Zhang, and L. Guo, "Study on the synthesis of Ni doped mesoporous TiO_2 and its photocatalytic activity for hydrogen evolution in aqueous methanol solution", Chemical Physics Letters **415**, 74–78 (2005).

[131]M. Haruta, "Size- and support-dependency in the catalysis of gold", Catalysis Today **36**, 153–166 (1997).

[132]K. Siegbahn, C. Nordling, and A. Fahlman, *ESCA : atomic, molecular and solid state structure studied by means of electron spectroscopy*, Presented to the Royal Society of Sciences of Uppsala, Dec. 3rd, 1965. (Uppsala : Almqvist and Wiksell, 1967).

[133]G. Greczynski and L. Hultman, "X-ray photoelectron spectroscopy: Towards reliable binding energy referencing", Progress in Materials Science **107**, 100591 (2020).

[134]M. P. Seah, "Simple universal curve for the energy-dependent electron attenuation length for all materials", Surface and Interface Analysis **44**, 1353–1359 (2012).

[135]ISO 18115-1, Surface Chemical Analysis—Vocabulary, Part 1—General Terms and Terms Used in Spectroscopy, International Organization for Standardization, Geneva (2013).

[136]G. Greczynski and L. Hultman, "A step-by-step guide to perform x-ray photoelectron spectroscopy", Journal of Applied Physics **132**, 1–53 (2022).

[137]M. J. Chester and T. Jach, "Grazing-incidence x-ray photoelectron spectroscopy from multilayer media: Oxidized GaAs(100) as a case study", Physical Review B **48**, 17262–17270 (1993).

[138]W. G. Richards, "The use of Koopmans' Theorem in the interpretation of photoelectron spectra", International Journal of Mass Spectrometry and Ion Physics **2**, 419–424 (1969).

[139]J. J. Yeh, *Atomic Calculation of Photoionization Cross-Section and Asymmetry Parameters* (Gordon and Breach Science Publishers, Langhorne, PE (USA), 1993).

[140]J. J. Yeh and I. Lindau, "Atomic subshell photoionization cross sections and asymmetry parameters", Atomic Data and Nuclear Data Tables **32**, 1–155 (1985).

[141]J. P. Lowe, *Quantum chemistry*, Student Edition (Academic Press, Inc., New York, NY (USA), 1978).

[142]C. Nicolas and C. Miron, "Lifetime broadening of core-excited and -ionized states", Journal of Electron Spectroscopy and Related Phenomena **185**, 267–272 (2012).

[143]G. H. Major, N. Fairley, P. M. A. Sherwood, M. R. Linford, J. Terry, V. Fernandez, and K. Artyushkova, "Practical guide for curve fitting in x-ray photoelectron spectroscopy", Journal of Vacuum Science & Technology A **38**, 061203-1–061203-22 (2020).

[144]S. Doniach and M. Sunjic, "Many-electron singularity in X-ray photoemission and X-ray line spectra from metals", Journal of Physics C: Solid State Physics **3**, 285–291 (1970).

[145]A. J. Maxwell, P. A. Brühwiler, A. Nilsson, N. Mårtensson, and P. Rudolf, "Photoemission, autoionization, and x-ray-absorption spectroscopy of ultrathin-film C_{60} on Au(110)", Physical Review B **49**, 10 717–10 725 (1994).

[146]D. Coster and R. D. L. Kronig, "New type of auger effect and its influence on the x-ray spectrum", Physica **2**, 13–24 (1935).

[147]P. S. Bagus, C. J. Nelin, C. R. Brundle, and S. A. Chambers, "A New Mechanism For XPS Line Broadening: The 2p-XPS of Ti(IV)", The Journal of Physical Chemistry C **123**, 7705–7716 (2019).

[148]National Institute of Standards and Technology, "NIST X-ray Photoelectron Spectroscopy Database", NIST Standard Reference Database Number 20, `10.18434/T4T88K` (2012).

[149]D. A. Shirley, "High-Resolution X-Ray Photoemission Spectrum of the Valence Bands of Gold", Physical Review B **5**, 4709–4714 (1972).

[150]M. Repoux, "Comparison of Background Removal Methods for XPS", Surface and Interface Analysis **18**, 567–570 (1992).

[151]S. Tougaard, W. Braun, E. Holub-Krappe, and H. Saalfeld, "Test of algorithm for background correction in XPS under variation of XPS peak energy", Surface and Interface Analysis **13**, 225–227 (1988).

[152]B. Rupp, *Biomolecular Crystallography: Principles, Practice, and Application to Structural Biology*, 1st (Garland Science, New York, 2009) Chap. 8: Instrumentation and data collection.

[153]K. Wille, "Synchrotron radiation sources", Reports on Progress in Physics **54**, 1005–1068 (1991).

[154]S. Zhu, M. Scardamaglia, J. Kundsen, R. Sankari, H. Tarawneh, R. Temperton, L. Pickworth, F. Cavalca, C. Wang, H. Tissot, J. Weissenrieder, B. Hagman, J. Gustafson, S. Kaya, F. Lindgren, I. Källquist, J. Maibach, M. Hahlin, V. Boix, T. Gallo, F. Rehman, G. D'Acunto, J. Schnadt, and A. Shavorskiya, "HIPPIE: a new platform for ambient-pressure X-ray photoelectron spectroscopy at the MAX IV Laboratory", Journal of Synchrotron Radiation **28**, 624–636 (2021).

[155]A. Preobrajenski, A. Generalov, G. Öhrwall, M. Tchaplyguine, H. Tarawneh, S. Appelfeller, E. Frampton, and N. Walsh, "FlexPES: a versatile soft X-ray beamline at MAX IV Laboratory", Journal of Synchrotron Radiation **30**, 831–840 (2023).

[156]I. Asconea and R. Strange, "Biological X-ray absorption spectroscopy and metalloproteomics", Journal of Synchrotron Radiation **16**, 413–421 (2009).

[157]P. M. V. Raja and A. R. Barron, "A Practical Introduction to X-ray Absorption Spectroscopy", in *Physical Methods in Chemistry and Nano Science* (LibreTexts, Online at: https://chem.libretexts.org) Chap. 1.8, pp. 49–57.

[158]W. R. Flavell, "Surface Structure Determination by Interference Techniques", in *Surface Analysis - The Principal Techniques*, edited by J. C. Vickerman (John Wiley and Sons Ltd, Manchester, UK, 1997) Chap. 8, pp. 369–371.

[159]R. H. Temperton, "Complex molecules on surfaces: In-situ electrospray deposition and photoelectron spectroscopy", PhD Thesis, University of Nottingham (2017).

[160]J. B. Taylor, L. C. Mayor, J. C. Swarbrick, J. N. O'Shea, and J. Schnadt, "Charge-Transfer Dynamics at Model Metal-Organic Solar Cell Surfaces", The Journal of Physical Chemistry C **111**, 16071–16700 (2007).

[161]A. J. Gibson, R. H. Temperton, K. Handrup, and J. N. O'Shea, "Resonant core spectroscopies of the charge transfer interactions between C60 and the surfaces of Au(111), Ag(111), Cu(111) and Pt(111)", Surface Science **657**, 69–78 (2017).

[162]F. W. Sears and G. L. Salinger, *Thermodynamics, kinetic theory, and statistical thermodynamics*, Third Edition (Addison-Wesley, Reading, MA (USA), 1975).

[163]GNB Corporation, *Why Build A Stainless Steel Vacuum Chamber?*, https://www.vacuumchamber.com/blog/why-build-a-stainless-steel-vacuum-chamber/#:~:text=Low%20Outgassing%20Rates&text=Stainless%20steel%20does%20not%20hold,excellent%20material%20for%20vacuum%20chambers., (accessed: 06.11.2023).

[164]Northern Engineering Sheffield, *What is Viton? A Guide To Viton O Rings*, https://www.nes-ips.com/what-is-viton/, (accessed: 04.09.2023).

[165]A. Keçebaş and M. Kayfeci, "Hydrogen properties", in *Solar Hydrogen Production: Processes, Systems and Technologies*, edited by F. Calise, M. D. d'Accadia, M. G. L. Santarelli, A. Lanzini, and D. Ferrero (Academic Press, 2019) Chap. 1, pp. 3–29.

[166]Mitsubishi Gas Chemical, *AGELESS EYE™, Oxygen Indicator*, https://www.mgc.co.jp/eng/products/sc/ageless-eye.html, (accessed: 06.05.2021).

[167]K. Parvathi and M. T. Ramesan, "Effect of titanium dioxide on the structural, thermal, and electrical properties of chlorinated natural rubber/poly (indole) blend nanocomposites for flexible nanoelectronic devices", Journal of Applied Polymer Science **140**, 1–14 (2023).

[168]A. Fujishima, T. N. Rao, and D. A. Tryk, "Titanium dioxide photocatalysis", Journal of Photochemistry and Photobiology C: Photochemistry Reviews **1**, 1–21 (2000).

[169]A. Fujishima, X. Zhang, and D. A. Tryk, "TiO_2 photocatalysis and related surface phenomena", Surface Science Reports **63**, 515–582 (2008).

[170]S. Ge, D. Sang, L. Zou, Y. Yao, C. Zhou, H. Fu, H. Xi, J. Fan, L. Meng, and C. Wang, "A review on the Progress of Optoelectronic Devices Based on TiO_2 Thin Films and Nanomaterials", Nanomaterials **13**, 1141-1–22 (2023).

[171]M. A. Henderson, "A surface perspective on self-diffusion in rutile TiO_2", Surface Science **419**, 174–187 (1999).

[172]M. H. M. Ahmed, R. H. Temperton, and J. N. O'Shea, "An in situ exploration of subsurface defect migration to a liquid water-exposed rutile TiO_2(110) surface by XPS", Surface and Interface Analysis **53**, 997–1079 (2021).

[173]S. A. Chambers, M. H. Engelhard, L. Wang, T. C. Droubay, M. E. Bowden, M. J. Wahila, N. F. Quackenbush, L. F. J. Piper, T.-L. Lee, C. J. Nelin, and P. S. Bagus, "X-ray photoelectron spectra for single-crystal Ti_2O_3: Experiment and theory", Physical Review B **96**, 205143-1–11 (2017).

[174]X. Wang, R. Chen, C. Chen, and Q. Wang, "Hydrogen storage properties of Ti_xFe + y wt.% La and its use in metal hydride hydrogen compressor", Journal of Alloys and Compounds **425**, 291–295 (2006).

[175]M. Williams, M. V. Lototsky, M. W. Davids, V. Linkov, V. A. Yartys, and J. K. Solberg, "Chemical surface modification for the improvement of the hydrogenation kinetics and poisoning resistance of TiFe", Journal of Alloys and Compounds **509S**, S770–S774 (2011).

[176]C. Wan, X. Ju, Y. Qi, C. Fan, S. Wang, X. Liu, and L. Jiang, "A study on crystal structure and chemical state of TiCrVMn hydrogen storage alloys during hydrogen absorption-desorption cycling", International Journal of Hydrogen Energy **34**, 8911–8950 (2009).

[177]A. Ferrari and F. Körmann, "Surface segregation in Cr-Mn-Fe-Co-Ni high entropy alloys", Applied Surface Science **533**, 10.1016/j.apsusc.2020.147471 (2020).

[178]K. Manickam, D. M. Grant, and G. S. Walker, "Optimization of AB2 type alloy composition with superior hydrogen storage properties for stationary applications", International Journal of Hydrogen Energy **40**, 16288–16296 (2015).

[179]B. Gilbert, B. H. Frazer, A. Belz, P. G. Conrad, K. H. Nealson, D. Haskel, J. C. Lang, G. Srajer, and G. D. Stasio, "Multiple Scattering Calculations of Bonding and X-ray Absorption Spectroscopy of Manganese Oxides", The Journal of Physical Chemistry A **107**, 2839–2847 (2003).

[180]L. Xi, C. Schwanke, J. Xiao, F. F. Abdi, I. Zaharieva, and K. M. Lange, "In Situ L-Edge XAS Study of a Manganese Oxide Water Oxidation Catalyst", The Journal of Physical Chemistry **121**, 11977–12504 (2017).

[181]M. C. Biesinger, B. P. Payne, A. P. Grosvenor, L. W. M. Lau, A. R. Gerson, and R. S. C. Smart, "Resolving surface chemical states in XPS analysis of first row transition metals, oxides and hydroxides: Cr, Mn, Fe, Co and Ni", Applied Surface Science **257**, 2717–2730 (2011).

[182]M. Giménez-Marqués, E. Bellido, T. Berthelot, T. Simón-Yarza, T. Hidalgo, R. Simón-Vázquez, Á. González-Fernández, J. Avila, M. C. Asensio, R. Gref, P. Couvreur, C. Serre, and P. Horcajada, "GraftFast Surface Engineering to Improve MOF Nanoparticles Furtiveness", Small **14**, 1801900-1–1801900-11 (2018).

[183]S. Seong, E. Lee, H. W. Kim, B. I. Min, S. Lee, J. Dho, Y. Kim, J.-Y. Kim, and J.-S. Kang, "Experimental evidence for mixed-valent Cr ions in half-metallic CrO_2: Temperature-dependent XMCD study", Journal of Magnetism and Magnetic Materials **452**, 447–450 (2018).

[184]Z. Wang, L. Alrehaily, J. Joseph, J. C. Wren, J. Wang, and T.-K. Sham, "Scanning transmission X-ray microscopy studies of chromiumhydroxide hollow spheres and nanoparticles formed by gamma radiation", Canadian Journal of Chemistry **95**, 447–450 (2017).

[185]L. Farsi and N. A. Deskins, "First principles analysis of surface dependent segregation in bimetallic alloys", Physical Chemistry Chemical Physics **21**, 23626–23637 (2019).

[186]G. Laplanche, U. F. Volkert, G. Eggeler, and E. P. George, "Oxidation Behavior of the CrMnFeCoNi High-Entropy Alloy", Oxidation of Metals **85**, 629–645 (2016).

[187]Y. J. Li, A. Savan, A. Kostka, H. S. Stein, and A. Ludwig, "Accelerated atomic-scale exploration of phase evolution in compositionally complex materials", Materials Horizons **5**, 86–92 (2018).

[188]L. Schlapbach, A. Seiler, and F. Stucki, "Surface segregation in FeTi and its catalytic effect on the hydrogenation II: AES and XPS studies", Materials Research Bulletin **13**, 1031–1037 (1978).

[189]M. Faisal, J.-Y. Suh, and Y.-S. Lee, "Understanding first cycle hydrogenation properties of TiFeZr ternary alloys", International Journal of Hydrogen Energy **46**, 4241–4251 (2021).

[190]H. Züchner and G. Kirch, "Auger electron spectroscopy investigation of the activation of TiFe for hydrogen uptake", Journal of the Less Common Metals **99**, 143–150 (1984).

[191]G. Sandrock, "A panoramic overview of hydrogen storage alloys from a gas reaction point of view", Journal of Alloys and Compounds **293-295**, 877–888 (1999).

[192]X. Chen and S. S. Mao, "Titanium Dioxide Nanomaterials: Synthesis, Properties, Modifications, and Applications", Chemical Reviews **107**, 2891–2959 (2007).

[193]B. Wu, D. Liu, S. Mubeen, T. T. Chuong, M. Moskovits, and G. D. Stucky, "Anisotropic Growth of TiO_2 onto Gold Nanorods for Plasmon-Enhanced Hydrogen Production from Water Reduction", Journal of the American Chemical Society **138**, 1114–1117 (2016).

[194]M. Murdoch, G. I. N. Waterhouse, M. A. Nadeem, J. B. Metson, M. A. Keane, R. F. Howe, J. Llorca, and H. Idriss, "The effect of gold loading and particle size on photocatalytic hydrogen production from ethanol over Au/TiO_2 nanoparticles", Nature Chemistry **3**, 489–492 (2011).

[195]P. A. Brühwiler, O. Karis, and N. Mårtensson, "Charge-transfer dynamics studied using resonant core spectroscopies", Reviews of Modern Physics **74**, 703–740 (2002).

[196]A. J. Gibson, R. H. Temperton, K. Handrup, M. Weston, L. C. Mayor, and J. N. O'Shea, "Charge transfer from an adsorbed ruthenium-based photosensitizer through an ultra-thin aluminium oxide layer and into a metallic substrate", The Journal of Chemical Physics **140**, 234708-1–7 (2014).

[197]A. J. Britton, A. Rienzo, J. N. O'Shea, and K. Schulte, "Charge transfer between the Au(111) surface and adsorbed C_{60}: resonant photoemission and new core-hole decay channels", The Journal of Chemical Physics **133**, 094705-1–7 (2010).

[198]J. Schnadt, P. A. Brühwiler, L. Patthey, J. N. O'Shea, S. Södergren, M. Odelius, R. Ahuja, O. Karis, M. Bässler, P. Persson, H. Siegbahn, S. Lunell, and N. Mårtensson, "Experimental evidence for sub-3-fs charge transfer from an aromatic adsorbate to a semiconductor", Nature **418**, 620–623 (2002).

[199]H. Holland-Moritz, S. Scheeler, C. Stanglmair, C. Pacholski, and C. Ronning, "Enhanced sputter yields of ion irradiated Au nano particles: energy and size dependence", Nanotechnology **26**, 325301-1–7 (2015).

[200]R. H. Temperton, J. N. O'Shea, and D. J. Scurr, "On the suitability of high vacuum electrospray deposition for the fabrication of molecular electronic devices", Chemical Physics Letters **682**, 15–19 (2017).

[201]C. Bittencourt, P. Krüger, M. J. Lagos, X. Ke, G. V. Tendeloo, C. Ewels, P. Umek, and P. Guttmann, "Towards atomic resolution in sodium titanate nanotubes using near-edge X-ray-absorption fine-structure spectromicroscopy combined with multichannel multiple-scattering calculations", Beilstein Journal of Nanotechnology **3**, 789–797 (2012).

[202]P. Krüger, "Multichannel multiple scattering calculation of $L_{2,3}$-edge spectra of TiO_2 and $SrTiO_3$: Importance of multiplet coupling and band structure", Physical Review B **81**, 125121-1–6 (2010).

[203]K. Bapna, D. M. Phase, and R. J. Choudhary, "Study of valence band structure of Fe doped anatase TiO_2 thin films", Journal of Applied Physics **110**, 043910-1–6 (2011).

[204]A. Vázquez-López, D. Maestre, R. Martínez-Casado, J. Ramírez-Castellanos, I. Píš, S. Nappini, and A. Cremades, "Unravelling the role of lithium and nickel doping on the defect structure and phase transition of anatase TiO_2 nanoparticles", Journal of Materials Science **57**, 7191–7207 (2022).

[205]K. Luo, T. P. S. Clair, X. Lai, and D. W. Goodman, "Silver Growth on TiO_2(110) (1×1) and (1×2)", Journal of Physical Chemistry B **104**, 3050–3057 (2000).

[206]K. Luo, D. Y. Kim, and D. W. Goodman, "The nucleation and growth of gold on silica", Journal of Molecular Catalysis A: Chemical **167**, 191–198 (2001).

[207]C. J. Satterley, L. M. A. Perdigão, A. Saywell, G. Magnano, A. Rienzo, L. C. Mayor, V. R. Dhanak, P. H. Beton, and J. N. O'Shea, "Electrospray deposition of fullerenes in ultra-high vacuum: in situ scanning tunneling microscopy and photoemission spectroscopy", Nanotechnology **18**, 455304-1–5 (2007).

[208]L. Liu, S. Ouyang, and J. Ye, "Gold-Nanorod-Photosensitized Titanium Dioxide with Wide-Range Visible-Light Harvesting Based on Localized Surface Plasmon Resonance", Angewandte Chemie International Edition **52**, 6689–6693 (2013).

[209]D. S. Kumar, B. J. Kumar, and H. M. Mahesh, "Quantum Nanostructures (QDs): An Overview", in *Synthesis of Inorganic Nanomaterials*, edited by S. M. Bhagyaraj, O. S. Oluwafemi, N. Kalarikkal, and S. Thomas (Woodhead Publishing Ltd, Cambridge, UK, 2018) Chap. 3, pp. 59–88.

[210]C. Kormann, D. W. Bahnemann, and M. R. Hoffmann, "Preparation and characterization of quantum-size titanium dioxide", The Journal of Physical Chemistry **92**, 5196–5201 (1988).

Appendices

Appendix A

Supplementary Information

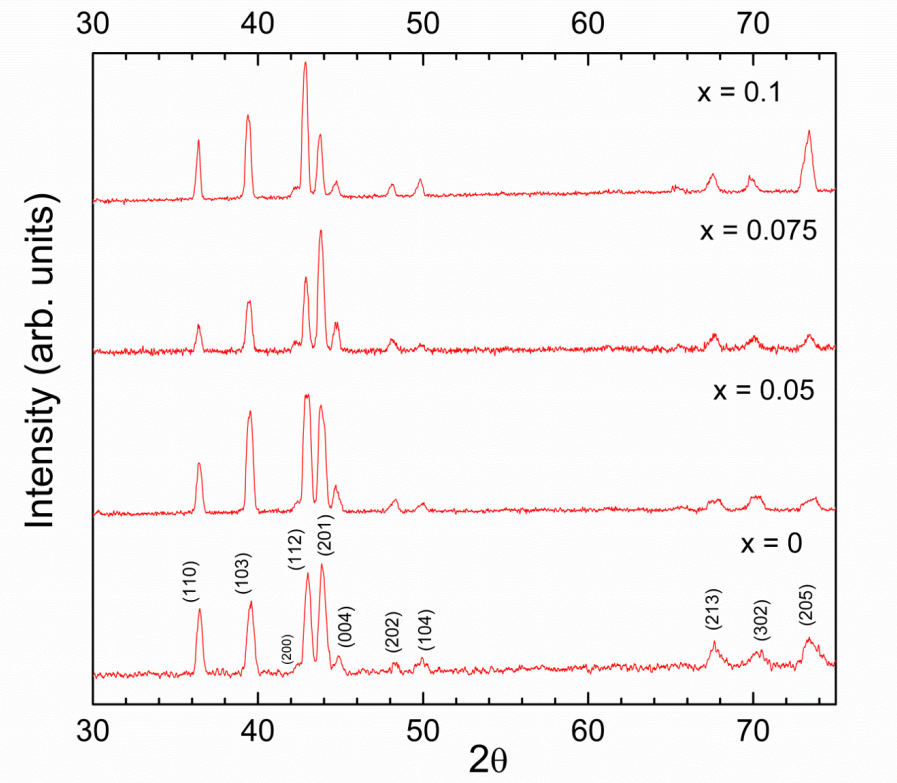

Figure A.1: Powder X-ray diffraction patterns $(Ti_{0.65}Zr_{0.35})_{1+x}MnCr_{0.8}Fe_{0.2}$ (x = 0, 0.05, 0.075 and 0.1) alloys using Cu Kα radiation (λ = 1.54056 Å). Performed by the authors of [178].

Table A.1: Relative amounts of each element in the alloy as-received and after each treatment, calculated from the areas of the peaks in the XPS spectra of the appropriate binding energy regions. Error ranges were calculated from the maximum and minimum area values which could be determined from differing background subtractions.

Treatment	**Relative amount of element and error range**				
	Ti	Zr	Mn	Cr	Fe
As-received (Surface)	0.73 ± 0.04	0.14 ± 0.005	1 ± 0.09	0.61 ± 0.02	0.18 ± 0.05
In Vacuum	0.63 ± 0.06	0.19 ± 0.006	1 ± 0.07	0.58 ± 0.02	0.09 ± 0.003
In Hydrogen	0.19 ± 0.03	0.03 ± 0.002	1 ± 0.04	0.49 ± 0.03	0.04 ± 0.02
In Hydrogen Twice	0.21 ± 0.07	0.004 ± 0.004	1 ± 0.09	0.10 ± 0.01	0.02 ± 0.01